

Unterschrift des Betreuers



TECHNISCHE
UNIVERSITÄT
WIEN

Vienna University of Technology

DIPLOMARBEIT

Head scatter modeling of the ImagingRing™ System

Ausgeführt am Atominstitut der Technischen Universität Wien

**unter der Anleitung von Univ.-Prof. Dr. DI Dietmar Georg
und Ko-Betreuung von DI Hermann Fuchs, PhD
und Mag. Peter Kuess, PhD**

durch

Niklas Reisz, Bsc

Mühlbergstraße 28/6

A-1140 Wien

24. Februar 2018

Unterschrift (Student)

Contents

List of Figures	IV
List of Tables	VIII
Abstract	XI
Zusammenfassung	XIII
1 Introduction	1
1.1 Motivation and objectives	1
1.2 Interactions between photons and matter	1
1.2.1 Rayleigh scattering	2
1.2.2 Compton scattering	2
1.2.3 Photoelectric effect	3
1.2.4 Pair production	4
1.2.5 Photonuclear reaction	6
1.2.6 Photon beam attenuation	6
1.3 X-rays	7
1.3.1 X-ray production	7
1.3.2 X-ray spectrum	8
1.3.3 Filtration and HVL	10
1.3.4 Angular distribution of X-rays and Heel effect	11
1.4 Monte Carlo method	12
1.5 Computed Tomography	13
1.6 Image guided radiotherapy	14
2 Materials	17
2.1 ImagingRing™ System	17
2.2 Geant4	18
2.3 Gate	20
2.3.1 Tuning of GATE parameters	21
2.4 SpekCalc	23
2.5 R	24
2.6 NOMEX	24
2.7 Lynx	25

3	X-ray head	27
3.1	Precalculated spectrum approach	27
3.2	Electron beam approach	28
3.3	Spectrum	29
3.4	X-ray tube geometry	30
3.5	X-ray head geometry	30
	3.5.1 STL import	31
	3.5.2 Pimary aperture and flattening filter	32
	3.5.3 Collimator jaws and exit window	32
3.6	Efficiency	33
4	Half value layer	37
4.1	Experiments	37
4.2	Results of experiments	39
4.3	Simulations	42
	4.3.1 Monoenergetic approach	42
	4.3.2 Energy weighting approach	43
4.4	Results of simulations and discussion	46
	4.4.1 Results of the monoenergetic approach	46
	4.4.2 Results of energy weighting approach	46
	4.4.3 Discussion	47
5	Focal spot	49
5.1	Experiments	49
5.2	Results of experiments	51
5.3	Simulations	56
5.4	Results of simulations and discussion	58
6	Heel effect	63
6.1	Experiments	63
6.2	Results of experiments	64
6.3	Simulations	65
6.4	Results of simulations and discussion	66
7	Summary	71
8	Conclusion and outlook	75
	Bibliography	77
A	Appendix	83
B	Code Listing	85

Acknowledgements

A very special gratitude goes out to my thesis advisors Hermann Fuchs and Peter Kuess for their excellent support and advice and for countless hours of productive discussions as well as to Professor Dietmar Georg who made this thesis possible. Working with them was a fantastic and highly informative experience.

I am also very grateful to Phil Steininger and Ivan Michael Messner from medPhoton whose scientific work laid the foundation for my thesis. Without their continued support and deep insight, the ImagingRing™ System could not have been modeled successfully.

In addition I would like to express my gratitude to the team at the Medical University of Vienna with a special mention to Andreas Resch for his support on handling the computer cluster and for the insight he provided on my simulations.

And finally, last but by no means least, I would like to thank Simon Rit from the Creatis Medical Imaging Research Center whose expert advice allowed me to overcome critical obstacles I have been facing through my research.

List of Figures

Fig. 1.1	Rayleigh scattering of a photon on a shell electron (from [35] p.194)	2
Fig. 1.2	Compton scattering of a photon on a weakly bound shell electron (from [35] p.174)	3
Fig. 1.3	Photoelectric effect: Left: Ionization of an inner shell electron. Right: An outer shell electron fills the vacancy and a photon is emitted. (from [35] p.169)	4
Fig. 1.4	Pair production: a photon is absorbed in the Coulomb field of the nucleus and a pair of electron and positron is created (from [35] p.191)	5
Fig. 1.5	Triplet production: a photon is absorbed in the coulomb field of an electron, ionizing the electron while creating a pair of electron and positron. (from [35] p.191)	5
Fig. 1.6	Photonuclear reaction: a photon is absorbed by the nucleus which enters an excited state. Subsequently the nucleus returns to its ground state and a nuclear particle is emitted (from [35] p.195)	6
Fig. 1.7	X-ray tube: K: cathode, A: anode (from [36] p.89)	7
Fig. 1.8	Modern rotating anode X-ray tube (from [36] p.129). Center-left: cathode, Center-right: rotating Anode. The tube is encased in glass.	8
Fig. 1.9	Process of generating characteristic X-rays: (a): Ionization of a K-shell electron through collision. (b): Electrons from outer shells fill the vacancy. The energies emitted are called K-series. (c): A vacancy in the L-shell is filled, the emitted energy is called L-series. (from [36] p.102)	9
Fig. 1.10	Production of bremsstrahlung from a scattered electron (from [36] p.92)	9
Fig. 1.11	X-ray spectrum: superposition of continuous spectrum (orange triangle) and discrete spectrum (blue lines) (from [36] p.90)	10
Fig. 1.12	100 keV Tungsten anode spectrum: from top to bottom: no filter, 0.5 / 1.0 / 1.5 / 2 / 3 / 4 / 6 / 8 / 10 mm Al (modified from [36] p.110)	11

Fig. 1.13 Heel effect: left: direction dependent attenuation of a photon beam by difference in length s travelled within the anode A. right: energy flux density dependent on the direction of emission. The values are relative to the energy flux density of the central beam.(from [36] p.124)	12
Fig. 1.14 time to solution: Monte Carlo vs analytical method (from [4] p.8)	13
Fig. 1.15 Rotating source and detector of a modern CT (from [44] p.32)	14
Fig. 2.1 ImagingRing™ System at MedAustron (from [43]) The ring surrounds the patient couch. Both are mounted on a robotic arm. X-ray head and detector are positioned underneath the patient couch. . . .	19
Fig. 2.2 sketch of the layered architecture of GATE (from [17]) p.4546 .	20
Fig. 2.3 Results of different parameter settings in GATE. All HVL_{A1} are relative to a reference value at a step and cut size of 0.005 mm. The x axis is logarithmic. The dashed black line shows the influence of the step size at a fixed cut size of 0.005 mm. The dotted blue line shows the influence of the cut size at a fixed step size of 0.005 mm. The solid red line shows the effect of simultaneously changing step and cut size to the same value.	23
Fig. 2.4 The NOMEX Multimeter (PTW, Freiburg, Germany) (from [50])	25
Fig. 2.5 The Lynx PT (IBA Dosimetry, Bartlett, USA) (from [15]) . . .	26
Fig. 3.1 Electron beam approach: a cathode "K" (orange) emits electrons (red) which impact on the anode "A" (blue) resulting in X-ray photons (green). The electron beam is perpendicular to the anode surface.	28
Fig. 3.2 Example spectrum of a 120 keV tungsten anode registered by an energy spectrum actor. The literature values for the energy and relative intensity of the K-lines are: $K_{\alpha 1} : E = 57.98keV, I = 0.576$, $K_{\alpha 2} : E = 59.32keV, I = 1$, $K_{\beta 1} : E = 67.2keV, I = 0.338$, $K_{\beta 2} : E = 69.1keV, I = 0.086$ [18]	29
Fig. 3.3 Geometry of the X-ray tube modeled in GATE: blue, center: anode, green: glass casing, red: oil (coolant), yellow: lead cylinder, blue: polycarbonate exit-cone	30
Fig. 3.4 Primary aperture (blue) and flattening filter (green) in GATE. .	32
Fig. 3.5 Collimator jaws in GATE.	33
Fig. 3.6 Evaluation of the efficiency of the simulated anode. The electron beam (red) hits the anode (blue). Many electrons are deflected but are eliminated before they leave the sphere. The photons (green) exit the sphere and contribute to the particle count.	34
Fig. 3.7 Efficiency of the anode for different energies as simulated in GATE.	35
Fig. 3.8 Efficiency of different splitting factors in GATE. Both axes are logarithmic.	36

Fig. 4.1	Experimental setup of HVL_{Al} measurements. The NOMEX Multimeter was placed on the patient couch, in the central beam of the X-ray source.	38
Fig. 4.2	X-ray image of the NOMEX multimeter. The red dot marks the central beam.	39
Fig. 4.3	HVL_{Al} without flattening filter and primary collimator for different filtration and tube currents	40
Fig. 4.4	HVL_{Al} with flattening filter and primary collimator for different filtration and tube currents	41
Fig. 4.5	Simulation of HVL_{Al} measurements. From left to right: cuboid block of aluminum (green), copper filter (white square), polycarbonate exit window (white circle), collimator jaws (blue), primary collimator (green), flattening filter (blue), exit cone (blue), lead cylinder (yellow), oil (red), glass (green).	43
Fig. 4.6	Left: a monoenergetic energy spectrum with $\omega(80keV) = 1$, Right: linear combination of three energies with $\omega(60keV) = 0.2$, $\omega(80keV) = 0.6$ and $\omega(90keV) = 0.2$	44
Fig. 4.7	Deposited energy in aluminum. Left: monoenergetic electron beam of $E_1 = 120keV$ and $\omega_1 = 1$, Right: monoenergetic electron beam of $E_2 = 100keV$ and $\omega_2 = 1$, Bottom: Example of a linear combination of electron energies. $E_1 = 120keV$, $\omega_1 = 0.6$ and $E_2 = 100keV$, $\omega_2 = 0.4$	45
Fig. 4.8	Weighting factors of an optimized electron energy spectrum for a tube voltage of 120kV.	48
Fig. 5.1	Experimental setup of the focal spot measurements: the X-ray head on the left side was placed in a horizontal position, with the slit camera directly next to the exit window. The detector was positioned parallel.	50
Fig. 5.2	Profile of the small focal spot. Left: in horizontal direction. Right: in vertical direction.	52
Fig. 5.3	Profile of the large focal spot. Left: in horizontal direction. Right: in vertical direction.	52
Fig. 5.4	Vertical (blue line) and horizontal (red line) length in [mm] of the large focal spot (FS) for varying tube voltages.	53
Fig. 5.5	Vertical (blue line) and horizontal (red line) length in [mm] of the large focal spot (FS) for varying tube currents.	53
Fig. 5.6	Vertical (blue line) and horizontal (red line) length in [mm] of the large focal spot (FS) for varying irradiation times.	54
Fig. 5.7	Vertical (blue line) and horizontal (red line) length in [mm] of the small focal spot (FS) for varying tube voltages.	54
Fig. 5.8	Vertical (blue line) and horizontal (red line) length in [mm] of the small focal spot (FS) for varying tube currents.	55

Fig. 5.9	Vertical (blue line) and horizontal (red line) length in [mm] of the small focal spot (FS) for varying irradiation times.	55
Fig. 5.10	Approximation of the experimentally measured profile of the small focal spot (black, solid line) by four normal distributions (red, blue, green and yellow dashed or dotted lines).	56
Fig. 5.11	Sketch of an elliptical focal spot. Left: anode as seen from the side, FSh is the horizontal size of the focal spot, PD is the penetration depth of the electrons, alpha is the anode angle. Right: anode as seen from front for negligible penetration depths, FSv is the vertical size of the focal spot.	58
Fig. 5.12	Comparison of the experimental data of the focal spot profile in horizontal direction and the superposition of normal distributions in R. Left: small focal spot, Right: large focal spot. This approximation served as a basis for the model of the focal spot in GATE.	59
Fig. 5.13	Comparison of the profile of the small focal spot in horizontal direction for simulation and experiment.	60
Fig. 5.14	Comparison of the profile of the large focal spot in horizontal direction for simulation and experiment.	61
Fig. 6.1	Experimental setup of heel measurements. Left: the X-ray head of the ImagingRing™ System, Right: The Lynx camera. The detector (not in the picture) of the ImagingRing™ System was moved to the top in order to protect the electronics from unfiltered radiation. . . .	64
Fig. 6.2	Intensity profile of the X-ray source of the ImagingRing™ System without primary collimator, flattening filter and collimator jaws as detected by the Lynx camera. Left: absolute intensity, right: intensity relative to maximum	65
Fig. 6.3	Simulation of Heel measurements. Left: The detection plane of the Lynx camera (blue), Right: the X-ray head of the ImagingRing™ System.	66
Fig. 6.4	Greyscale plot of the 2D intensity distribution of the X-ray source of the ImagingRing™ System without primary collimator, flattening filter and collimator jaws. Left: 2D intensity measured with Lynx. The image is cut off due to the limited size of the Lynx scan field. Right: simulated 2D intensity	67
Fig. 6.5	Comparison of the heel effect in vertical direction for simulation and experiment for a monochromatic electron beam of 120 keV. Due to the limited size of the Lynx scan field, the experimental data is cut off to the right.	68
Fig. 6.6	Comparison of the heel effect in vertical direction for simulation and experiment for an electron energy spectrum that resulted from the optimization in chapter 4.3.2. Due to the limited size of the Lynx scan field, the experimental data is cut off to the right.	69

List of Tables

1.1	Example discrete X-ray energies for a tungsten anode	9
2.1	Simulation parameters for the detector used in HVL_{AI} evaluations. From [51]	21
4.1	HVL_{AI} values measured on the ImagingRing™ System without primary collimator, flattening filter and collimator jaws for a tube current of 20 mA (small focal spot). All empirical standard deviations were below 0.1 mm	39
4.2	HVL_{AI} values measured on the ImagingRing™ System without primary collimator, flattening filter and collimator jaws for a tube current of 40 mA (large focal spot). All empirical standard deviations were below 0.1 mm	39
4.3	HVL_{AI} values measured on the ImagingRing™ System with primary collimator, flattening filter and collimator jaws for a tube current of 20 mA (small focal spot). All empirical standard deviations were below 0.1 mm	41
4.4	HVL_{AI} values measured on the ImagingRing™ System with primary collimator, flattening filter and collimator jaws for a tube current of 40 mA (large focal spot). All empirical standard deviations were below 0.1 mm	41
4.5	Simulated HVL_{AI} values without primary collimator and flattening filter and mean relative deviation between simulation and experiment. All empirical standard deviations were below 0.1 mm	46
4.6	Simulated HVL_{AI} values with primary collimator and flattening filter and mean relative deviation between simulation and experiment. All empirical standard deviations were below 0.1 mm	46
4.7	Simulated HVL_{AI} values without primary collimator and flattening filter and mean relative deviation between simulation and experiment. All empirical standard deviations were below 0.1mm	47
4.8	Simulated HVL_{AI} values with primary collimator and flattening filter and mean relative deviation between simulation and experiment. All empirical standard deviations were below 0.1 mm	47

5.1	Focal spot size of the small and large focal spot measured with a slit camera and the detector of the ImagingRing™ System. All empirical standard deviations were below 0.1 mm.	51
5.2	Fit parameters for the simulation of the small focal spot in GATE. Each normal distribution is implemented in GATE as a separate electron beam. Each electron source in GATE, called "Beam i" corresponds to a two dimensional normal distribution of mean value μ_i , standard deviations $\sigma_{ver,i}$ and $\sigma_{hor,i}$ and intensity a_i	58
5.3	Fit parameters for the simulation of the large focal spot in GATE. Each normal distribution is implemented in GATE as a separate electron beam. Each electron source in GATE, called "Beam i" corresponds to a two dimensional normal distribution of mean value μ_i , standard deviations $\sigma_{ver,i}$ and $\sigma_{hor,i}$ and intensity a_i	59
A.1	HVL _{A1} and computing time for varying step sizes inside the anode volume. All HVL _{A1} and computing times are relative to a reference value at a step size of 0.005 mm.	83
A.2	HVL _{A1} and computing time for varying cut sizes inside the anode volume. All HVL _{A1} and computing times are relative to a reference value at a cut size of 0.005 mm.	83
A.3	HVL _{A1} and computing time for varying cut sizes inside the anode volume. All HVL _{A1} and computing times are relative to a reference value at a cut size of 0.005 mm.	83
A.4	Efficiency of different splitting factors	84

Abstract

The ImagingRing™ System (medPhoton, Salzburg, Austria) is a novel X-ray planar and cone beam computed tomography system for in room imaging in particle therapy. The aim of this study was to establish a Monte Carlo model of the ImagingRing™ System for future research on scatter effects.

The X-ray head was modeled using the Monte Carlo toolkit GATE (v8.0, GEANT4 Application for Tomographic Emission) and GEANT4 (GEometry ANd Tracking v.10.3).

In a first step, the tungsten anode and the electron beam emerging from the cathode were modeled using GATE. Its surrounding glass and oil, as well as the polycarbonate exit cone were modeled directly while the primary collimator, collimator jaws and flattening filter were imported from vendor supplied CAD-files.

Next, experimental characterization was performed. Half-Value-Layers (HVL) in aluminum were determined with a selection of filtration levels and types using a NOMEX multimeter (PTW, Freiburg, Germany). In the simulated model, the energy spectrum was tuned by approximating the energy of the electron beam by a linear combination of discrete energies. The resulting MC based HVLs in aluminum were compared to experimental data. The best approximation for the energy spectrum was determined by minimizing a cost function.

The physical dimensions of the electron focal spot on the anode were measured using a dedicated slit camera (PTW, Freiburg, Germany). The slit camera restricted the beam to a narrow slit. The projection of this slit was then registered by the detector of the ImagingRing™ System. Subsequently, findings on position and shape of the electron focal spot were implemented in the simulation.

In addition, two-dimensional dose distributions in absence of a flattening filter were first measured, using the scintillation based Lynx detector (IBA, Schwarzenbruck, Germany), and then simulated.

The average deviation between measured and simulated HVL_{Al} was within 3% for the whole clinical energy range between 80 keV to 120 keV. This agreement was

within measurement uncertainty. The size and shape of the simulated electron focal spot agreed closely with the experimentally measured data. The heel effect stemming from the anode was clearly visible in both the experimental data and the MC simulation and the intensity profiles matched.

In conclusion, a GATE based X-ray head model was established, that accurately resembles experimental measurements. The presented method was shown to provide a realistic X-ray distribution, enabling the estimation of imaging doses when implementing new clinical protocols or predict the impact of technical changes of the X-ray source. The developed method can be transferred to model other commercial X-ray units. The established model also allows detailed MC based investigations of the head scatter to improve imaging quality.

Zusammenfassung

Das ImagingRing™ System (medPhoton, Salzburg, Österreich) ist ein neuartiger Röntgen-Kegelstrahl Computertomograph zur Bildgebung in der Strahlentherapie.

Das Ziel dieser Arbeit war es, ein Monte Carlo Computermodell des ImagingRing™ Systems zu erstellen, welches zur späteren Untersuchung von Streueffekten dient.

Der Strahlkopf wurde mit Hilfe des Monte Carlo Toolkits GATE (v8.0, GEANT4 Application for Tomographic Emission) und des Simulationscodes GEANT4 (Geometry ANd Tracking v.10.3) modelliert.

Im ersten Schritt wurde die Anode und der Elektronenstrahl, welcher auf der Wolfram-Kathode auftrifft in GATE modelliert. Diese Elemente wurden von einer Glas- und einer Ölschicht umgeben. Die gesamte Röhre wurde dann von einem Bleizylinder eingeschlossen, welchen der Röntgenstrahl durch ein Polycarbonat-Austrittsfenster verlässt. Während diese Elemente direkt in GATE modelliert wurden, wurden der Ausgleichsfilter, der Primärkollimator und die Kollimatorblätter mit Hilfe von durch den Hersteller bereitgestellten CAD-Dateien importiert.

Im nächsten Schritt wurde das Modell anhand von experimentellen Daten evaluiert. Halbwertsschichtdicken in Aluminium bei unterschiedlicher Filterung wurden mit dem NOMEX Multimeter (PTW, Freiburg, Deutschland) gemessen. In der Simulation wurde das Energiespektrum des Röntgenstrahls angepasst, indem die Energie des Elektronenstrahls durch eine Linearkombination diskreter Energien angenähert wurde. Die resultierenden Halbwertsschichtdicken in Aluminium wurden mit den experimentellen Messwerten verglichen. Die beste Näherung des Energiespektrums wurde durch eine Minimierung einer Kostenfunktion gefunden.

Die Größe und Form des Elektronen Fokuspunktes auf der Anode wurden mit einer Schlitzkamera (PTW, Freiburg, Deutschland) gemessen. Diese Kamera schränkte den Röntgenstrahl auf einen schmalen Schlitz ein. In Folge wurde seine Projektion auf die Detektorebene des ImagingRing™ Systems detektiert. Die Resultate dieser Messungen wurden anschließend im Computermodell integriert.

Abschließend wurde die zweidimensionale Intensitätsverteilung ohne Ausgleichsfilter

mit der Lynx Kamera (IBA, Schwarzenbruck, Deutschland) gemessen und in GATE simuliert.

Die durchschnittliche Abweichung zwischen gemessenen und simulierten Halbwertsschichtdicken in Aluminium betrug unter 3% in dem gesamten klinisch relevanten Energiebereich zwischen 80 keV und 120 keV. Die Übereinstimmung zwischen Experiment und Simulation war damit innerhalb der Messgenauigkeit. Größe und Form des Fokuspunktes stimmten weitgehend mit den experimentellen Daten überein. Der Heel-Effekt der Anode war sowohl im Experiment als auch in der Simulation deutlich sichtbar und die Intensitätsprofile stimmen überein.

Zusammenfassend wurde ein auf GATE basierendes Modell des Röntgenkopfes erstellt, welches die reellen Gegebenheiten in hohem Detailgrad wiedergibt. Die beschriebene Vorgehensweise lieferte eine realistische Röntgenstrahlverteilung, welche zur Abschätzung von Strahlungsdosen in Folge der Implementierung neuer klinischer Routinen oder zur Vorhersage der Wirkung von technischen Änderungen an der Röntgenquelle verwendet werden kann. Die dabei entwickelte Methode kann auch auf die Modellierung anderer kommerzieller Röntgengeräte angewandt werden. Außerdem erlaubt das entwickelte Modell eine detaillierte Monte Carlo basierte Untersuchung der Streustrahlung zur Verbesserung der Bildqualität.

1. Introduction

1.1 Motivation and objectives

Proton- and ion beam therapy is an innovative and precise treatment modality for tumor patients. Compared to conventional radiation therapy with photons the dose to adjacent healthy tissue can be greatly decreased. In December 2016, the first Austrian facility for particle-beam therapy MedAustron became operational. The high precision of this therapy results in considerable demands with respect to patient positioning, and patient image quality of image guided radiotherapy approaches.

At MedAustron, in-room imaging is performed with the ImagingRing™ System. It is a novel X-ray cone beam computed tomography system, designed to allow an independent movement of X-ray head and detector as well as longitudinal movement along the patient couch. This enables a large field of view and the possibility for imaging during irradiation.

The image quality can be negatively influenced by possible imaging radiation scatter. To account for such scatter, Monte Carlo (MC) simulations of the imaging device can provide valuable information. Therefore, the aim of this thesis was to model and validate the design of the ImagingRing™ Systems X-ray head in the Monte Carlo toolkit GATE. The modelling included the X-ray tube and internal components such as the primary collimator, collimator jaws and flattening filter. Furthermore, the model was validated by measurements performed on the ImagingRing™ System at MedAustron.

1.2 Interactions between photons and matter

The following chapter is based on the books by Hanno Krieger [35–37]

1.2.1 Rayleigh scattering

Rayleigh scattering describes the elastic scattering of a photon by the electron shell of an atom. In this process the photon gets absorbed by the electron and induces oscillation. This oscillation causes the electron to emit a photon of the same wavelength. The energy of the primary photon $E_{\gamma 0}$ is conserved, the direction however is changed by an angle φ . A sketch of the process can be seen in figure 1.1.

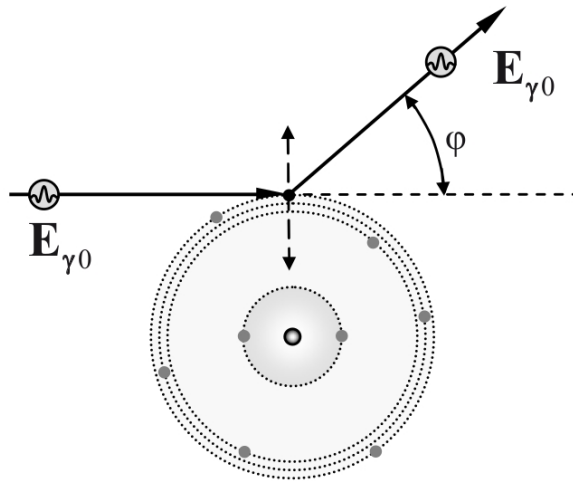


Figure 1.1: Rayleigh scattering of a photon on a shell electron (from [35] p.194)

Therefore, Rayleigh scattering widens a photon beam, resulting in attenuation. The cross section σ_R of the process can be calculated from equation 1.1.

$$\sigma_R = \rho * \frac{Z^{1.5}}{E_{\gamma 0}^2} \quad (1.1)$$

$E_{\gamma 0}$ is the photon energy, ρ is the density of the absorber and Z is the atomic number. The effect is most important for low energies and absorbers of high atomic number.

1.2.2 Compton scattering

Compton scattering describes the inelastic scattering of a photon with energy $E_{\gamma 0}$ on an outer shell electron. Part of its momentum and energy is transferred to the recoiling electron, which causes a shift in the wavelength and direction of the photon and the ionisation of the electron. A sketch of the process can be seen in figure 1.2. The kinetic energy of the recoiling electron is equal to the energy difference of the

photon before and after the event, minus the binding energy of the electron as can be seen in equation 1.2.

$$E_{kin} = E_{\gamma} - E_{\gamma'} - E_{bind} \quad (1.2)$$

where E_{kin} is the kinetic energy of the recoiling electron, E_{γ} the energy of the photon before the event, $E_{\gamma'}$ its energy after the event and E_{bind} the binding energy of the electron.

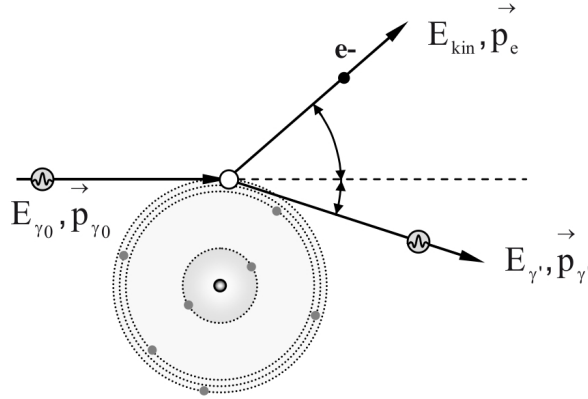


Figure 1.2: Compton scattering of a photon on a weakly bound shell electron (from [35] p.174)

The Compton interaction-coefficient σ_c describes the probability of this process and can be approximated by equation 1.3 for energies between 0.2 and 10 MeV.

$$\sigma_c = \rho * \frac{Z}{A} * \frac{1}{E_{\gamma}^n} \quad (n = 0.5 \text{ to } 1) \quad (1.3)$$

ρ is the density of the absorber, Z the atomic number, A the mass number and E_{γ} the photon energy. The ratio of atomic number and mass number $\frac{Z}{A}$ it is almost independent from the atomic number, especially for low Z elements.

1.2.3 Photoelectric effect

The photoelectric effect describes the ionization of an inner shell electron by a photon of energy E_{γ} . The photon is absorbed in the process and its energy is transferred to the electron. The kinetic energy of the emitted electron equals the difference between photon energy and binding energy. Therefore the photoelectric effect requires photons of energies higher or at least equal to the binding energy of the electron.

Below this threshold no ionization is possible. This process is illustrated in figure 1.3.

Conservation of momentum also demands that a fraction of the energy is transferred to the nucleus. However, due to the much larger mass of the nucleus, this fraction is not significant.

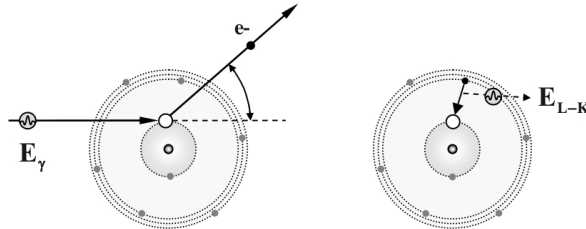


Figure 1.3: Photoelectric effect: Left: Ionization of an inner shell electron. Right: An outer shell electron fills the vacancy and a photon is emitted. (from [35] p.169)

The photo-absorption coefficient τ describes the probability of the process. It can be approximated by relation 1.4

$$\tau \propto \rho * \frac{Z^n}{A} \quad (n = 4 - 4.5) \quad (1.4)$$

where ρ is the density of the absorber, Z is its atomic number and A is its mass number.

The energy dependence below 511 keV is approximately proportional to $\frac{1}{E^3}$. As the probability for absorption is the highest when photon energy and binding energy are exactly the same, absorption edges can be observed.

1.2.4 Pair production

Photons can be absorbed in an electromagnetic field of a nucleus and be converted into a particle and its anti-particle. The photon is absorbed during the process. For this effect to occur, the energy of the photon must at least be equal to the rest mass energy of both particles. In the case of the creation of an electron and a positron this energy threshold is found at 1022 keV. Any energy exceeding the rest mass energy is converted into kinetic energy and split between the two particles.

The probability for the process κ_{pair} can be estimated from equation 1.5

$$\kappa_{pair} \propto Z * \rho * \log(E_{\gamma 0}) \quad (1.5)$$

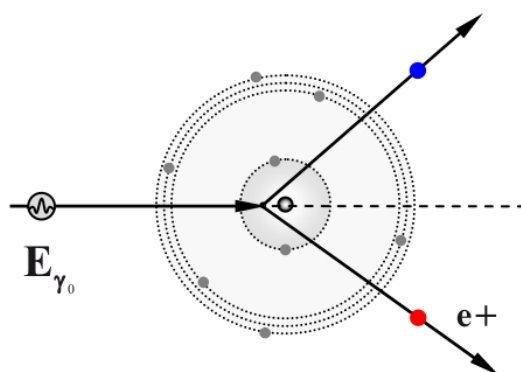


Figure 1.4: Pair production: a photon is absorbed in the Coulomb field of the nucleus and a pair of electron and positron is created (from [35] p.191)

It is proportional to the density ρ and the atomic number Z of the absorber as well as the logarithm of the photon energy E_{γ_0} .

After depositing the kinetic energy in the absorber material through numerous scatter incidents the positron collides with an electron and both particles are annihilated, resulting in an annihilation radiation of two 511 keV photons that are emitted in opposite directions.

The rare event of pair production in the Coulomb field of an electron is called triplet production because of the ionization of the participating electron. The associated attenuation coefficient is denoted κ_{tripl} . A sketch can be seen in figure 1.4 for pair production and 1.5 for triplet production.

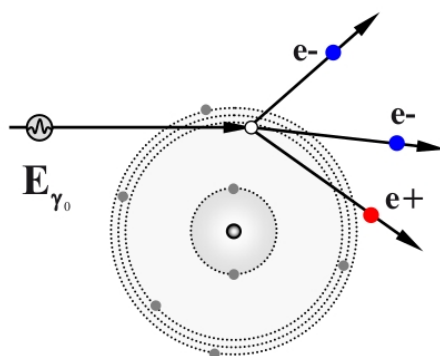


Figure 1.5: Triplet production: a photon is absorbed in the coulomb field of an electron, ionizing the electron while creating a pair of electron and positron. (from [35] p.191)

1.2.5 Photonuclear reaction

Similar to the photoelectric effect, a photon can be absorbed by an atomic nucleus if its energy is higher than the binding energy of one of the nuclear particles. The nucleus then enters an excited state and immediately decays, emitting a nuclear particle. This process is shown in figure 1.6. The photons energy is transferred to the nucleus, causing a photon beam to be attenuated which is expressed by the attenuation coefficient σ_{np} . This effect is mostly relevant for energies between 10 and 20 MeV and is therefore not important in the energy range used for medical imaging.

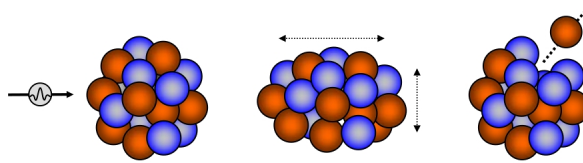


Figure 1.6: Photonuclear reaction: a photon is absorbed by the nucleus which enters an excited state. Subsequently the nucleus returns to its ground state and a nuclear particle is emitted (from [35] p.195)

1.2.6 Photon beam attenuation

All attenuation coefficients for the processes explained above can be summed up to one energy dependent attenuation coefficient μ , which can be calculated from equation 1.6.

$$\mu = \tau + \sigma_c + \sigma_R(+\kappa_{pair})(+\kappa_{tripl})(+\sigma_{nr}). \quad (1.6)$$

where τ is the photo absorption coefficient, σ_c is the compton interaction coefficient, σ_R is the Rayleigh interaction coefficient, κ_{pair} is the pair-production coefficient, κ_{tripl} is the triplet-production coefficient and σ_{nr} is the photonuclear-reaction coefficient. Pair-production, triplet-production and photonuclear reaction are insignificant for the low to mid keV energy range. Thus they were excluded in expression 1.6.

The attenuation of a monoenergetic photon beam, specifically its number of photons N and its intensity I , by an absorber of thickness d and the attenuation coefficient μ is then described by the following well known equations 1.7 and 1.8.

$$N(d) = N_0 \cdot e^{-\mu d} \quad (1.7)$$

$$I(d) = I_0 \cdot e^{-\mu d} \quad (1.8)$$

Therefore, beam attenuation occurs in an exponential fashion depending on the atomic number and the density of the absorbing material.

1.3 X-rays

The following chapter is based on the books by Hanno Krieger [35–37]

X-rays were first discovered in 1895 by W.C. Röntgen and are of great importance in radiology and medical imaging. They are part of the electromagnetic spectrum with wavelengths shorter than visible light.

1.3.1 X-ray production

An X-ray tube consists of a heated cathode, made from heat resistant metal, that emits electrons in vacuum through thermal emission. The electrons then impact on an anode, usually made from tungsten, and their kinetic energy is converted into heat and radiation. Between cathode and anode the electrons are accelerated by an electric field. This setup is shown in figure 1.7.

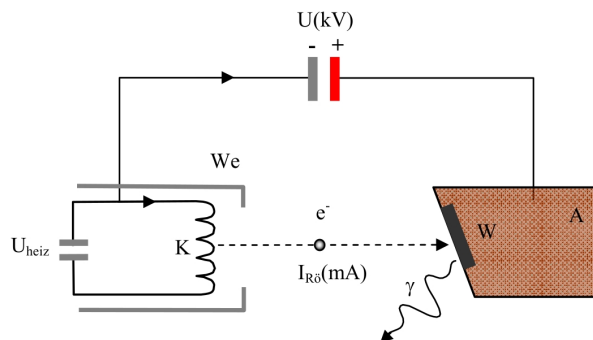


Figure 1.7: X-ray tube: K: cathode, A: anode (from [36] p.89)

The electron focal spot causes high temperatures in the anode, often damaging the anode material. Therefore, heat removal is a crucial part of X-ray tube design. For this reason, modern X-ray tubes often contain a cone segment-shaped rotating anode to distribute the heat over a wider area. Additionally, the tube is externally cooled with water or oil. A sketch of a modern X-ray tube can be found in figure 1.8.

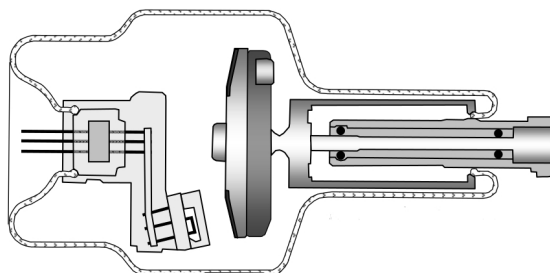


Figure 1.8: Modern rotating anode X-ray tube (from [36] p.129). Center-left: cathode, Center-right: rotating Anode. The tube is encased in glass.

The generated X-rays exit the tube through an exit window, often made from X-ray transparent beryllium or polycarbonate.

1.3.2 X-ray spectrum

When high energy electrons are decelerated in the anode material, X-rays of a particular energy spectrum are emitted. The spectrum results from two different physical processes: ionization and bremsstrahlung.

Characteristic radiation

When an accelerated electron collides with electrons of the anode material, those electrons get ionized if the kinetic energy exceeds the binding energy. The ionized electrons leave the atom and electrons from higher energy levels fill the vacancy. As a result, X-ray photons are emitted. The energy of these photons is equivalent to the difference in energy levels, which is characteristic for the element. Hence the name characteristic radiation. A sketch of this process can be found in figure 1.9.

The characteristic energies are labeled after the shell of the ionized electron. In addition, an index denotes the shell from which the electron filling the vacancy originates from. For example, if an electron from the K-shell gets ionized and an electron from the L-shell fills the vacancy, the resulting X-ray energy is called K_{α} .

For tungsten, the most important energies are listed in 1.1.

However, there is another competing process called Auger emission, where the energy surplus is transferred to an outer shell electron instead of being emitted as a photon. The electron is then ionized and leaves the atom with a kinetic energy that is equal to the difference in energy levels minus the binding energy.

Table 1.1: Example discrete X-ray energies for a tungsten anode

Name	Energy level transition	Energy [keV]	Relative frequency [%]
$K_{\alpha 1}$	$L_{III} - K$	59.318	100
$K_{\alpha 2}$	$L_{II} - K$	57.981	57
$K_{\beta 1}$	$M_{III} - K$	67.245	22
$L_{\alpha 1}$	$M_V - L_{III}$	8.398	100
$L_{\beta 1}$	$M_{IV} - L_{II}$	9.673	52
$L_{\beta 2}$	$N_V - L_{III}$	9.962	22

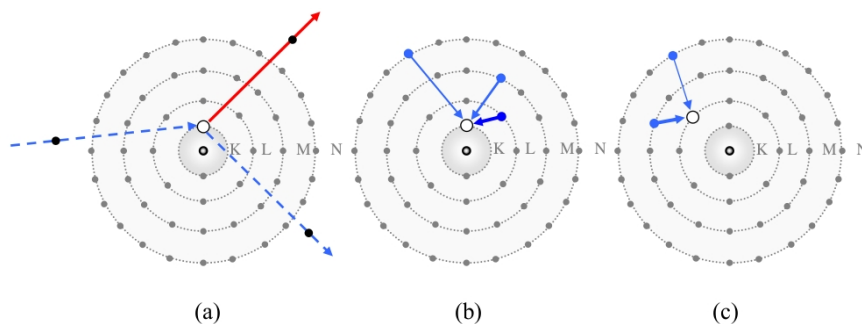


Figure 1.9: Process of generating characteristic X-rays: (a): Ionization of a K-shell electron through collision. (b): Electrons from outer shells fill the vacancy. The energies emitted are called K-series. (c): A vacancy in the L-shell is filled, the emitted energy is called L-series. (from [36] p.102)

Bremsstrahlung

When electrons are scattered and decelerated by the strong Coulomb field of a nucleus they give off continuous X-ray radiation. The energy of the radiation is equal to the difference in kinetic energy before and after the electron was scattered. The intensity of this so called "bremsstrahlung" is proportional to its wavelength. The minimum wavelength is determined by the maximum energy of the electron and thus by the tube voltage. Figure 1.10 shows a sketch of this process.

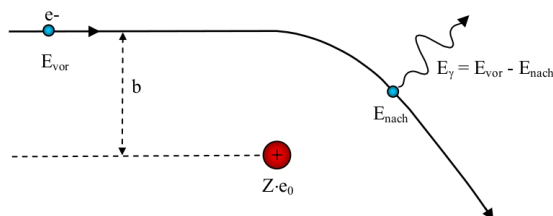


Figure 1.10: Production of bremsstrahlung from a scattered electron (from [36] p.92)

The X-ray spectrum is a superposition of the characteristic spectrum and the continuous spectrum. The maximum energy of this spectrum is the energy of the electron, which is determined by the tube voltage. A sketch of the superposition can be seen in figure 1.11.

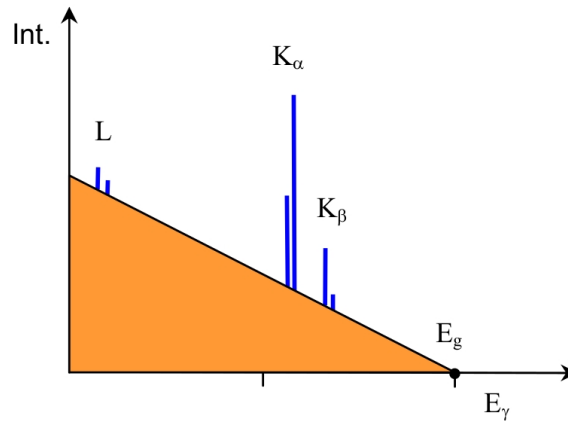


Figure 1.11: X-ray spectrum: superposition of continuous spectrum (orange triangle) and discrete spectrum (blue lines) (from [36] p.90)

Efficiency

The efficiency of the X-ray tube is proportional to the atomic number Z as well as the tube voltage. For this reason a heat resistant material with high atomic number like tungsten ($Z = 74$) is chosen as anode material. Nevertheless, even for tungsten the efficiency factor is less than 1% for energies below 100 keV.

1.3.3 Filtration and HVL

For medical imaging on the human thorax, energies mostly around 120 keV are used. The low energy portion of the spectrum is absorbed entirely. Therefore, it does not contribute to the image and should be eliminated for the purpose of radiation protection. By adding a filter made of aluminium, rhenium, tungsten or other materials of similar properties the low energy portion of the spectrum can be suppressed. Figure 1.12 shows example spectra for different filtrations.

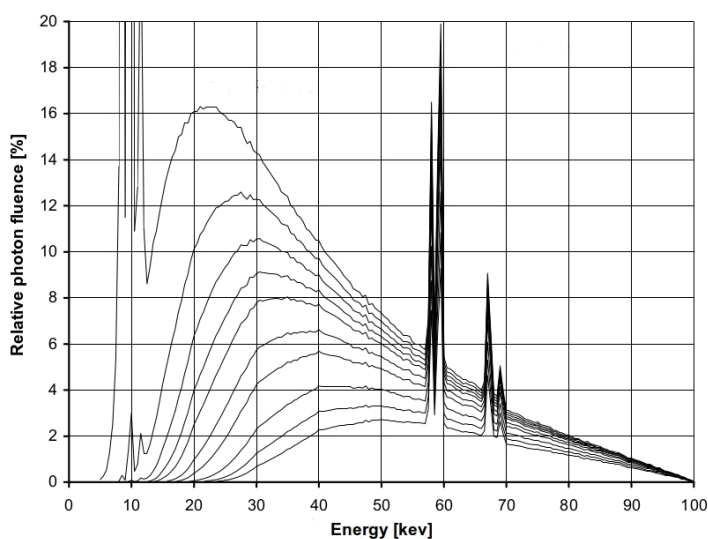


Figure 1.12: 100 keV Tungsten anode spectrum: from top to bottom: no filter, 0.5 / 1.0 / 1.5 / 2 / 3 / 4 / 6 / 8 / 10 mm Al (modified from [36] p.110)

The amount of filtration of a specific material needed to reduce the intensity of a beam to its half is called half value layer (HVL). It can be measured with little effort and is used in medical physics to characterize the energy spectrum of the beam.

1.3.4 Angular distribution of X-rays and Heel effect

Characteristic X-rays are emitted almost homogeneous in all directions. Therefore, their intensity distribution is isotropic. In contrast, bremsstrahlung is emitted mostly perpendicular to the electron beam. However due to multiple scatter events the electrons are deflected soon after entering the anode and the resulting bremsstrahlung is emitted almost homogenous in all directions. As a result, the intensity is distributed in a hemisphere around the anode.

However, due to the anode geometry the distance travelled by a photon within the anode depends on the angle, effectively adding filtration. As a result the intensity of the beam varies depending on the direction of emission. This effect is called heel effect. A sketch can be seen in figure 1.13. Its influence is mostly unwanted in planar imaging and thus has to be compensated by additional filters or through patient positioning [5]. In contrast, other applications like mammography take advantage of the heel effect.

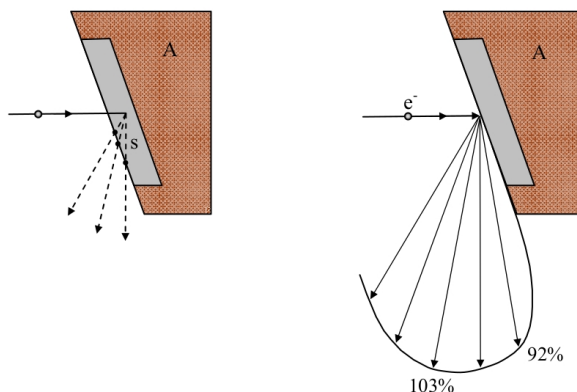


Figure 1.13: Heel effect: left: direction dependent attenuation of a photon beam by difference in length s travelled within the anode A. right: energy flux density dependent on the direction of emission. The values are relative to the energy flux density of the central beam.(from [36] p.124)

1.4 Monte Carlo method

The idea of using a large number of random events to find an approximation to a mathematical problem can be traced back to Georges Louis LeClerc (1707-1788). This French scientist used needle tosses (and even baguettes tossed onto tiles) to estimate the value of π . The method was then refined by John von Neumann and Stanislaw Ulam during the Manhattan Project to simulate the path of neutrons travelling through radiation shielding. It is named after the Monte Carlo casino in Monaco [25].

In order to simulate a system it firstly has to be modelled using a series of probability density functions. Then a large number of outcomes is sampled from these functions through the use of random numbers. The data of interest can then be calculated from the samples [25].

Because of the high complexity of the systems examined and the high number of samples required to acquire the desired accuracy the use of computers is essential. Therefore, the applicability of Monte Carlo simulations is limited by the available computing power, the computer memory and consequently by time [38]. However, computers are getting faster and cheaper at a geometric rate, which is known as Moore's law [4].

Monte Carlo simulations are especially useful for highly complex problems as the amount of work required to find an analytical solution gets out of hand quickly. Figure 1.14 illustrates required time to find a solution for Monte Carlo methods versus analytical methods.

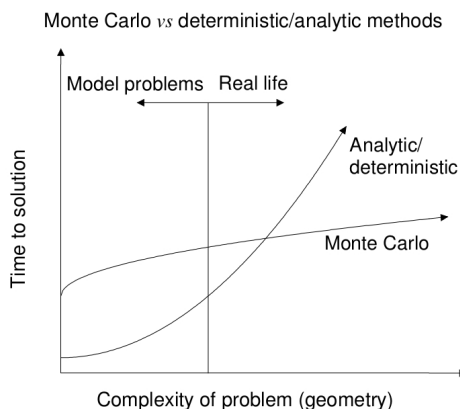


Figure 1.14: time to solution: Monte Carlo vs analytical method (from [4] p.8)

Today's applications of Monte Carlo simulations are numerous and reach from particle physics [19] to finance [30] and biology [38] with no end in sight.

1.5 Computed Tomography

The following section is based on the book by Victor Mikla [44].

Computed Tomography (CT) or CT scan is a combination of computer technology with X-ray imaging, widely used in medical radiology. Through the computer processed combination of X-ray images taken from different angles, a three dimensional image of the patient can be constructed. This allows physicians to look at a patient's body slice by slice and give access to areas that were previously hidden by overlaying tissue.

The CT scanner was first developed in 1972 by British engineer Godfrey Hounsfield and American physicist Allan M. Cormack, who later on shared the nobel prize in medicine for their invention. The mathematical theory needed was developed in 1917 by Johann Radon, who showed mathematical prove that a function could be reconstructed from an infinite set of its projections. This reconstruction was called Radon transformation.

A CT consists of a gantry and a patient couch. The X-ray source is mounted on the gantry and can circle the patient. A detector is either placed opposite of the source or along the entire gantry to detect the image. In image guided radiotherapy, cone shaped X-ray beams combined with collimators and filters such as the device sketched in figure 1.15 are of high importance. For other applications such as diagnostic radiology, modern spiral CT are the standard.

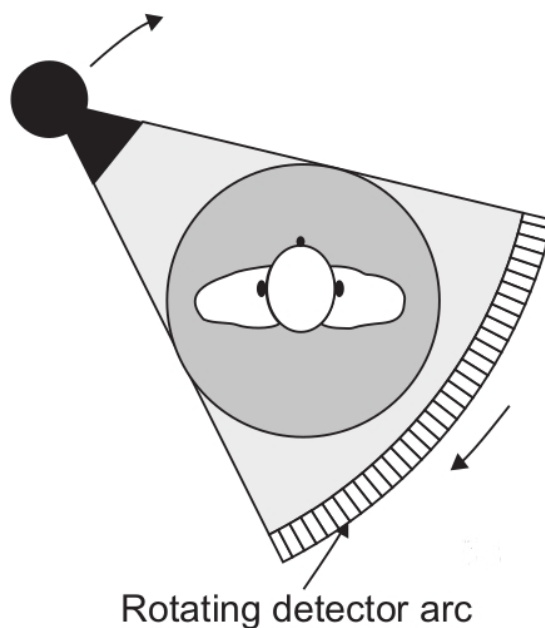


Figure 1.15: Rotating source and detector of a modern CT (from [44] p.32)

In medicine, CT scans can be used to detect tumors, complex bone fractures, haemorrhage or infarction. Before and during radiotherapy, CT scans are used to evaluate size and position of a tumor. In addition to that they are essential for treatment planning as they provide a basis for dose calculations. But the use of CT extends even further as it is used in material sciences and industry, e.g for defect detection.

1.6 Image guided radiotherapy

This section is based on the lecture by Professor Dietmar Georg [23] and the paper published by Stock et al. [60].

Imaging plays an essential role in radiotherapy and is present in every step of the treatment.

Before therapy, a treatment plan has to be established. This plan is based on a CT scan. Radiation oncologists delineate tumor structures as well as organs at risk on these CT scans. Additionally, the type and density of tissue can be concluded. Based on this information, the treatment plan is calculated. It intends to cover the cancerous area while sparing organs at risk. Delineation can be improved by combining CT information with magnetic resonance tomography (MR) images.

Imaging is also used during the course of the treatment to direct the radiation therapy. This process is called image guided radiotherapy. It is a novel field and the first generation of equipment is becoming available.

Before each treatment session, the immobilized patient has to be aligned correctly, to ensure that he or she is positioned as required by the treatment plan. This can be done by the use of a cone beam CT. Positioning is even more important for particle therapy, as particle beams are highly precise and very sensitive to range variations.

During the course of the therapy, the tumors size or position might change, depending on several factors such as organ filling, organ movement, receptiveness to the therapy and weight loss. As a result, the treatment plan might need to be renewed in order to fit to the changed anatomy [26, 55, 64]. Thus an additional CT scan is required at this stage to re-plan the dose distribution for the patient.

Changes in anatomy caused by organ or cavity filling can be monitored through high quality planar X-ray imaging. This partly substitutes weekly control CT scans and thus helps to significantly reduce imaging dose [59]. If needed, the treatment plan can be adapted based on a new planning CT scan.

Involuntary or necessary movement of the patient might also influence the position of the tumor. This is especially true in the case of lung cancer, where the patient's breathing motion heavily alters the targets position. As a solution, advanced techniques such as gating and tracking based on real-time X-ray imaging are deployed as an alternative to extended safety margins or breath hold techniques [21, 56].

Recent research investigates the applicability of MR for treatment planning and in room imaging [24]. MR images have increased soft tissue contrast compared to X-ray images, which is beneficial to the process of tissue characterization. Hybrid MR linear accelerator systems are already available and MR guided proton therapy has become an important research topic [20, 45, 57, 67].

2. Materials

2.1 ImagingRing™ System

The ImagingRing™ System (medPhoton, Salzburg, Austria), shown in figure 2.1, is a cone beam computed tomography device for medical imaging [33, 43, 68]. It is used for patient positioning in radiation therapy. The device consists of a Monobloc (IMD generators, Grassobbio, Italy) X-ray tube contained in the X-ray head on one side and a XRD flat panel detector (PerkinElmer, Waltham, USA) on the other side. Both are mounted and independently movable on a ring around the patient couch. The ring itself allows movement along the patient axis with a longitudinal travel range of up to 125 cm [42]. This way, the whole body can be imaged without re-positioning the patient. Comprehensive image processing and reconstruction software is used for the independently positioned source and detector and to account for gravity induced geometrical changes [2, 53, 62].

X-ray head

The Monobloc is a rotating anode X-ray tube with two different cathodes, depending on the tube current. It allows for currents below 40 mA (one cathode) as well as above 40 mA (both cathodes). This also influences the size of the focal spot, resulting in a larger focal spot for higher currents [41].

The X-ray radiation exits the tube through a layer of glass, followed by oil and a polycarbonate exit window, resulting in an inherent self-filtration equivalent to 1.4 mm of aluminum.

The system operates at photon energies in the range of 40 keV to 120 keV with 80 keV and 120 keV being most relevant for clinical use.

The source emits X-rays in so called pulses. These are constant time intervals of a set length. For each irradiation, the number and length of pulses can be defined.

In contrast to conventional X-ray CT devices, the ImagingRing™ System does not use the product of tube current and time (mAs) for calibration. Instead, it uses the detector entrance dose converted to air KERMA (Kinetic Energy Released per unit MAass). Thereby, eventual nonlinearities of the tube current can be avoided and the settings of different ImagingRing™ Systems can be translated from device to device.

The primary aperture, made from lead, follows directly after the exit window. Additionally, an aluminum flattening filter is mounted on top of the primary aperture to compensate the heel effect. The entire Monobloc is rotated by 3° around the transversal axis to further reduce the influence of the heel effect.

To shape the field of view, four moveable collimator jaws are used. Furthermore, the latest model of the X-ray head includes four different possible filter settings (air, aluminum, copper, combination of copper and silver) [41].

The X-ray head can be rotated freely around the patient. The rotational movement range is 476.21° [42].

Detector

The XRD detector is an amorphous silicon flat panel X-ray detector based on a CsI scintillator. The "XRD 1642 AP" model used for the ImagingRing™ System offers a resolution of 1024×1024 pixels and high framerates of up to 100 fps. It has an active sensor area of $41 \times 41 \text{ cm}^2$ [41]. The detector can be rotated by up to 481.5° around the patient [42].

MedAustron

All physical measurements described in this work were performed at the MedAustron treatment facility, specifically in the research room "IR1". At MedAustron, proton beams are used to treat patients suffering from cancer and carbon ions are planned to be used clinically from early 2019 on [60]. For this purpose, a linear accelerator and a synchrotron ring accelerate particles to up to 80% of the speed of light [40].

The ImagingRing™ System is used at MedAustron for in room imaging.

2.2 Geant4

GEANT4 (GEometry ANd Tracking) is a toolkit for simulating the behaviour of particles as they travel through matter. It was developed at CERN by a collaboration of physicists from around the world. It is capable of simulating particle emission



Figure 2.1: ImagingRing™ System at MedAustron (from [43]) The ring surrounds the patient couch. Both are mounted on a robotic arm. X-ray head and detector are positioned underneath the patient couch.

and tracking the particles along their way through a specified geometry [22]. The source code of the software itself is freely available as a download.

A wide range of physical processes are taken into account by GEANT4, including electromagnetic, hadronic and optical processes as well as most elements and relevant materials. For each process, different models are available. Depending on the energy range and available computing power, suitable models can be chosen flexibly and combined in a so-called physics list. The physics list then defines the set of models used for the computation of all interactions of particles. In contrast to other simulation systems, adding or modifying a model is a well defined process that requires little to no alteration of the source code. Because of this flexibility and the wide range of energies offered (250 eV to several TeV), GEANT4 is used for particle physics, nuclear physics, accelerator design, space engineering and medical physics [16].

In GEANT4, particles are simulated one by one and each particle is tracked along its way. The track consists of discrete steps whose lengths are defined by the so-called step size. After each step all interactions described in the physics list that fit the particle type are evaluated by sampling from the appropriate probability distributions. To limit this tracking process, a parameter called track cut can be specified. If the average length of a particle's path is shorter than the track cut, GEANT4 removes the particle and deposits its energy locally. This can be used to speed up the computing process by eliminating particles that stand no chance of reaching the relevant detection volume. In a similar way, the production cut parameter can be used to remove secondary particles of short residual range [22].

2.3 Gate

GATE, the Geant4 Application for Tomographic Emission is based on the GEANT4 framework and acts as a toolkit for simulating medical applications of radiation physics [17]. While GEANT4 provides the simulation models, GATE offers an easy to use macro mechanism to control intricate geometries. It can be used for the design of new medical devices as well as for the optimization of image acquisition, image reconstruction and random noise reduction.

GATE is written in C++. It uses a layered design. Its core defines the main features. Based on the core is the application layer which is a set of C++ classes. The user layer, however, is built in a user friendly way that does not require any C++ programming skills and allows control through an extended version of the Geant4 scripting language [17]. A sketch of the layered architecture of GATE can be found in figure 2.2.

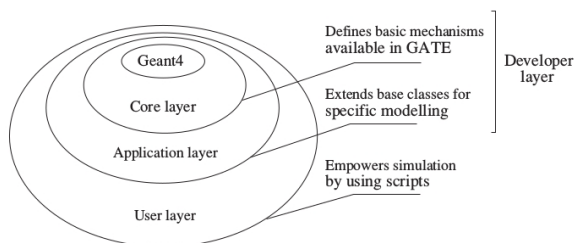


Figure 2.2: sketch of the layered architecture of GATE (from [17]) p.4546

In GATE, the geometry of a device can be modeled step by step by combining basic geometrical objects like boxes, spheres, cylinders and many more. A material can then be defined for each object.

In a similar way, a particle source can be added. The type of the particle as well as the energy distribution and direction can be defined to realistically reflect the real source.

In GATE, information is collected and stored by so-called actors. Actors are attached to volumes. Depending on the actor, data is stored in a user defined voxel matrix or histograms. There are different kinds of actors in GATE. The actors used include dose actors, which store the deposited energy in each voxel, and phase actors, which register particle-type, position, direction and energy of each particle that passes through the actor. Such actors can be used to register dose profiles or an energy spectrum.

2.3.1 Tuning of GATE parameters

GATE allows the user to customize a multitude of GEANT4 parameters in order to fit the desired model.

The GEANT4 physics list is one of the most impactful parameters. Users can choose from different lists, with each list being tailored to certain energy ranges or interactions. Different physics lists may therefore result in different outcomes of the same simulation.

Another important parameter is the maximum step size, which can be limited for each type of particle and for every volume in the simulation. Of particular interest are often the step size inside the detection volume and if present, inside any filter volume. This is due to the low mean free path inside these volumes and the resulting heavy impact on beam attenuation.

Similar to the step size, the cut size can be set in GATE. It heavily influences the production of secondary particles as all processes below the energy corresponding to the cut size do not take place.

Different parameter settings might result in different simulation outcomes. Thus, to establish an accurate X-ray source model, the physics list, the step size and the cut size were investigated.

The physics list as well as the step size and the cut size for photons in matter were tested in a preceding work [51]. The parameter settings found there can be seen in table 2.1. They have been used in this work as well.

As the step- and cut size for electrons in the anode material might influence the production of X-ray photons, it was tested in a series of simulations. Simulations were performed for the lowest energy (60 keV) as well as the highest energy (120 keV). For each simulation, HVL_{A1} values were evaluated and compared to experimental data.

Table 2.1: Simulation parameters for the detector used in HVL_{A1} evaluations. From [51]

Parameter	Setting
Actor	TLE-Dose
Step size (detector)	≤ 0.01 mm
Cut size (detector)	≤ 0.01 mm
Physics list	empenelope

Applying the setting from table 2.1 to the detector volume reduced the variance of the simulation by at least 20% compared to the default parameters at the small cost of a 10% increase in computing time. Results from other works suggest an even

stronger impact [66].

The results for different parameter settings inside the anode volume are visualized in figure 2.3. The results for the HVL_{A1} for a fixed cut size of 0.005 mm inside the anode volume can be found in table A.1. For a fixed step size of 0.005 mm the results can be found in table A.2. For a combination of both, the results are presented in table A.3.

Based on the data, a step and cut size of 0.001 mm was chosen for all subsequent simulations, as decreasing both values further resulted in no significant change in the HVL_{A1} but had a major impact on computing time.

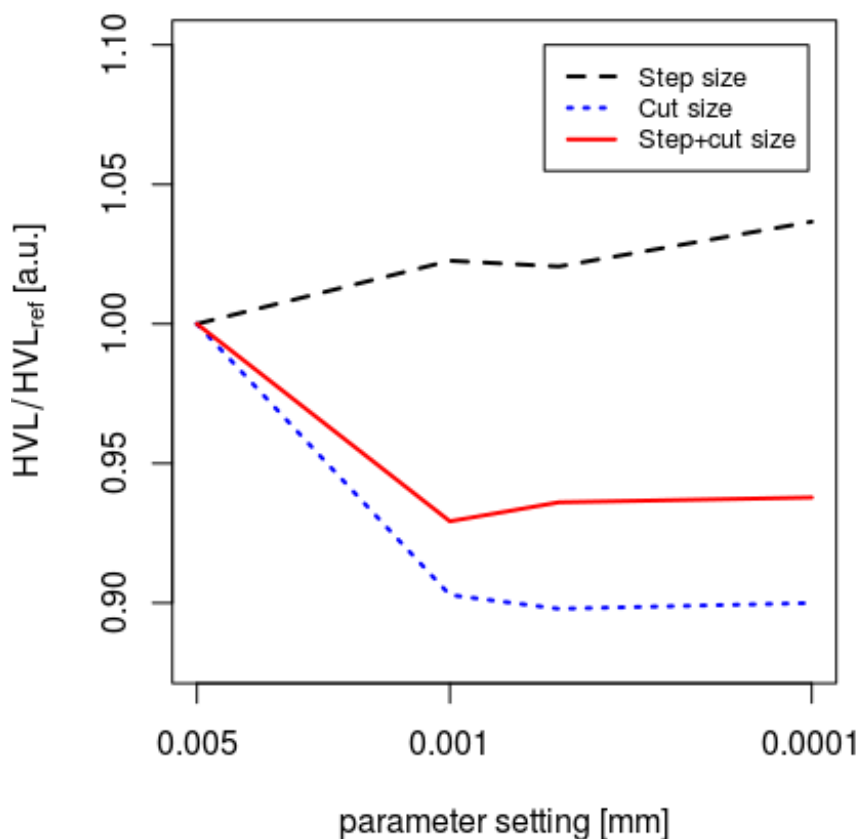


Figure 2.3: Results of different parameter settings in GATE. All HVL_{AI} are relative to a reference value at a step and cut size of 0.005 mm. The x axis is logarithmic. The dashed black line shows the influence of the step size at a fixed cut size of 0.005 mm. The dotted blue line shows the influence of the cut size at a fixed step size of 0.005 mm. The solid red line shows the effect of simultaneously changing step and cut size to the same value.

2.4 SpekCalc

SpekCalc is a software tool for Windows and Mac operating system for the creation of X-ray spectra emerging from a tungsten anode. It was created by G. Poludniowski et al. [47] and is based on calculations described in [48, 49]. The calculations were compared to MC simulations with discrepancies of less than a few percent [48].

The required input parameters to calculate a spectrum are tube voltage, which can

be chosen from the range of 40 keV to 300 kV and anode angle (6 to 30 degrees recommended). The output energy bin size with a minimum of 0.05 keV is also configurable. In addition, filters of various materials and adjustable thickness can be added [47].

The spectrum output is given as a histogram where the relative probability is plotted against the energy. In addition, SpekCalc calculates the first and the second half value layer (HVL) in aluminum and copper as well as the homogeneity factor, which is defined as the quotient of first and second half value layer.

2.5 R

R is a software and programming language for data manipulation, calculation and graphical display. It is freely available under the GNU general public license. R is based on the programming language S and was originally developed for academic purposes but is now also used by data analysts in the private sector as its popularity has increased substantially over the last years.

R comes with numerous packages for statistical computing and many more can be downloaded for free. All functions are stored in packages and have to be loaded before use for enhanced efficiency. The software is an efficient way of handling extensive amounts of data. [63].

While R only comes with a command line interface, several open source graphic user interfaces such as RStudio are available.

2.6 NOMEX

The NOMEX Multimeter (PTW, Freiburg, Germany), shown in figure 2.4, is a small multi-parameter measuring device for ionizing radiation. It uses semiconducting detectors to simultaneously measure dose, dose rate, dose per pulse, number of pulses, exposure time, tube voltage (maximum, mean and practical peak), half value layer in aluminum (HVL_{Al}) and total aluminum equivalent filtration. The device can be placed within the central beam, independently from tube-axis orientation [50].

The NOMEX Multimeter can be connected with a computer to display and store all measured data.

It is intended for quality assurance and control measurements in medical X-ray imaging. The uncertainty of the dose is within $\pm 1.5\%$ and the voltage within $\pm 0.5kV$ [9–11]. It is calibrated for the energy range used in radiography, mammography,

fluoroscopy and CT by the manufacturer. Calibration includes the calibration of air kerma, air kerma rate, tube voltage, time, total filtration and half value layers. A recalibration is recommended after two years [1].



Figure 2.4: The NOMEX Multimeter (PTW, Freiburg, Germany) (from [50])

2.7 Lynx

The Lynx PT (IBA Dosimetry, Bartlett, USA), shown in figure 2.5, is a high resolution 2D dosimetry system. It consists of a scintillating screen of 30 cm x 30 cm size coupled with a CCD camera with an effective resolution of 0.5 mm. The intensity of radiation can be measured for each of its pixel, resulting in a 2D intensity distribution. For high intensities, a shutter can be activated to protect the CCD camera. To measure absolute dose values the Lynx camera has to be calibrated [28].

The Lynx PT can be connected to a computer using a cat6 ethernet cable for real-time image acquisition and raw data correction.

It is used for quality assurance in proton and carbon ion therapy and was characterized in [54].



Figure 2.5: The Lynx PT (IBA Dosimetry, Bartlett, USA) (from [15])

3. X-ray head

In order to simulate the ImagingRing™ System, a viable model for the X-ray source itself had to be found.

In a first step, a precalculated spectrum was tested. Then, in a second step, a more direct approach to fully model an electron beam in GATE was tested. For this approach, the simulated X-ray spectrum was investigated and compared to literature values. Once the X-ray tube was established, the surrounding elements of the X-ray head were modeled. In a final step, the efficiency of the chosen approach was examined in GATE.

3.1 Precalculated spectrum approach

The first approach to model an X-ray source in GATE was to use a precalculated spectrum and import it into GATE.

SpekCalc was used to calculate an energy spectrum emerging from the tungsten anode. The anode angle was set to a value of 10° according to the tube documentation and the energy bin size was chosen to be 0.01 keV which is the minimum bin size in SpekCalc [27].

The calculated spectrum was then saved as a histogram and subsequently imported in GATE using the discrete input mode. Discrete input mode has been tested to be the most accurate among other input modes [51]. In GATE the energy of the particles emerging from the source volume were sampled from the imported histogram.

To validate the model, HVL_{Al} and $HVLCu$ values can be calculated in SpekCalc and compared to simulated values in GATE as described in a preceding work [51].

This approach provides a fast and accurate method for simulations of the central beam of the anode. However, energy spectrum and intensity of the emerging beam are homogeneous in all directions. As a result, any two dimensional effects such as

the heel effect of the anode are not reproduced. For this reason, this approach is not suitable for the investigation of head scatter.

Attempts were made to solve this problem by applying an external tungsten filter to the beam in order to artificially recreate the heel effect. To do so, the beam that exits the anode perpendicular to its surface is needed as its path through the anode material is the shortest. Thereby it is filtered the least. However, SpekCalc is only accurate for small offset angles and should not be used to calculate the beam perpendicular to the anode surface. For this reason the attempt to recreate the heel effect failed. Hence, a different method of simulating the source was chosen.

3.2 Electron beam approach

A more direct approach was to fully model the X-ray tube in GATE. For this, a tungsten anode and an electron beam were used, as can be seen in figure 3.1.

The rotating anode of the Monobloc was modeled as a truncated cone with an angle of 10° . Its material was set to pure tungsten. In reality the anode is in contact with a rhenium-molybdenum alloy for increased heat conduction (I.M. Messner, personal communication, June 9, 2017). However, as GATE does not consider heating and no particles reach the volume, it was omitted.

There are no electric fields in GATE to accelerate the electrons. Instead, the electron beam was created with a set energy, origin and direction. The electron energy was determined by the product of tube voltage and electron charge.

This model represents most important properties of an actual X-ray source. Therefore, it was chosen as a basis for further simulations.

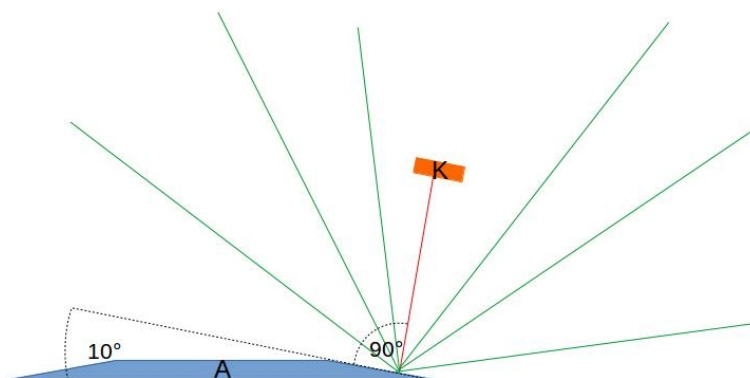


Figure 3.1: Electron beam approach: a cathode "K" (orange) emits electrons (red) which impact on the anode "A" (blue) resulting in X-ray photons (green). The electron beam is perpendicular to the anode surface.

3.3 Spectrum

To validate the approach, the X-ray spectrum emerging from the tungsten anode was evaluated in GATE. This was done by placing a planar energy spectrum actor in front of the source, perpendicular to the beam. The energy actor acted as a detector and registered the energy of incoming photons. For the actor a minimum energy of 3 keV, a maximum energy of 130 keV and the energy bin size of 85 eV was defined. The actor then registered all photons in the chosen energy range and created a histogram. The result of the simulation can be seen in figure 3.2. It is in excellent agreement with validated literature values [18].

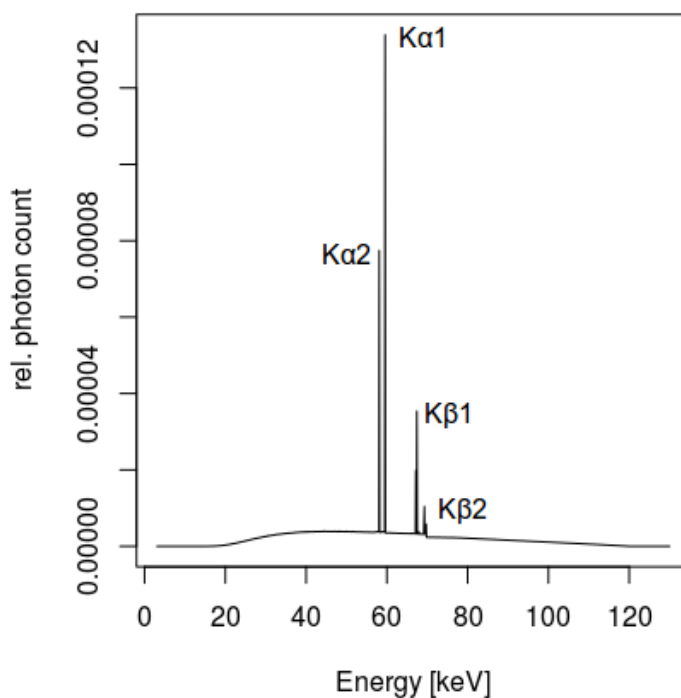


Figure 3.2: Example spectrum of a 120 keV tungsten anode registered by an energy spectrum actor. The literature values for the energy and relative intensity of the K-lines are:
 $K_{\alpha 1} : E = 57.98\text{keV}, I = 0.576$, $K_{\alpha 2} : E = 59.32\text{keV}, I = 1$, $K_{\beta 1} : E = 67.2\text{keV}, I = 0.338$,
 $K_{\beta 2} : E = 69.1\text{keV}, I = 0.086$ [18]

3.4 X-ray tube geometry

Surrounding the anode, a lead cone with a circular opening of 2.8 cm diameter collimates the X-ray beam. Inside the opening a cylindrical polycarbonate exit-window is placed. Emerging from the exit-window is the rest of the polycarbonate exit-cone at an angle of 64.58° around the central beam [29].

In addition to that, a glass cylinder was placed inside the lead cone and the space in between was filled with oil to reflect the self-filtration of the X-ray tube trough its glass tube and oil coolant. As no specific information about the oil was available, it was assumed to be a dielectric transformer oil. Figure 3.3 illustrates the geometry of the X-ray tube in GATE.

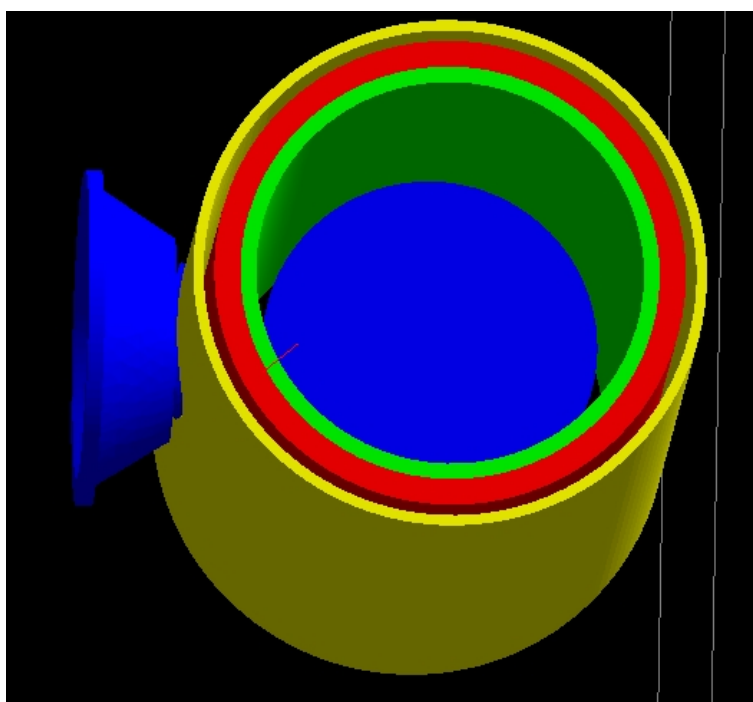


Figure 3.3: Geometry of the X-ray tube modeled in GATE: blue, center: anode, green: glass casing, red: oil (coolant), yellow: lead cylinder, blue: polycarbonate exit-cone

3.5 X-ray head geometry

To complete the X-ray head of the ImagingRing™ System, the flattening filter, the primary collimator and the collimator jaws were added. This was done by importing the premodeled files to GATE.

3.5.1 STL import

In GATE, geometrical objects can be imported from a CAD software using the tessellated volume (STL) format. All surfaces are approximated by numerous small triangles. The choice of geometrical shapes in GATE is very limited and there are no boolean operations possible such as intersecting or combining volumes. Thus, modeling a complex geometry in a CAD program is an attractive alternative.

To rule out possible artifacts from the STL approximation, a test was conducted. In this test, several different geometrical shapes were both modeled in GATE and in FreeCAD [52].

Each shape was irradiated by a photon beam of 120 keV and projected onto a detection plane. Between the objects a planar kill actor was placed to separate them. The projected image as registered by the dose actor inside the detection plane was then checked for possible artifacts.

The following shapes were investigated:

- Sphere
- Hollow zylinder
- Zylinder
- Cone, parallel to axis
- Cone, perpendicular to axis
- Wedge
- Ellipsoid

No difference between models in GATE and STL models were found, suggesting that this method provides a fast and accurate way of modeling complex geometries in GATE.

It is worth mentioning that the STL file does not contain any information about the unit of measure. Therefore, one has to be careful to use the same unit of measure for both GATE and the CAD software or else the object's scaling might be off by the conversion factor. The standard unit of measure in GATE is millimeter. The origin point of the geometry is saved in the STL file and matches the origin in GATE when importing a geometry.

3.5.2 Primary aperture and flattening filter

The primary aperture as well as the flattening filter were modeled by medPhoton and imported in GATE using the STL file format. Figure 3.4 shows their geometry in GATE. For the primary aperture lead was used and aluminum for the flattening filter.

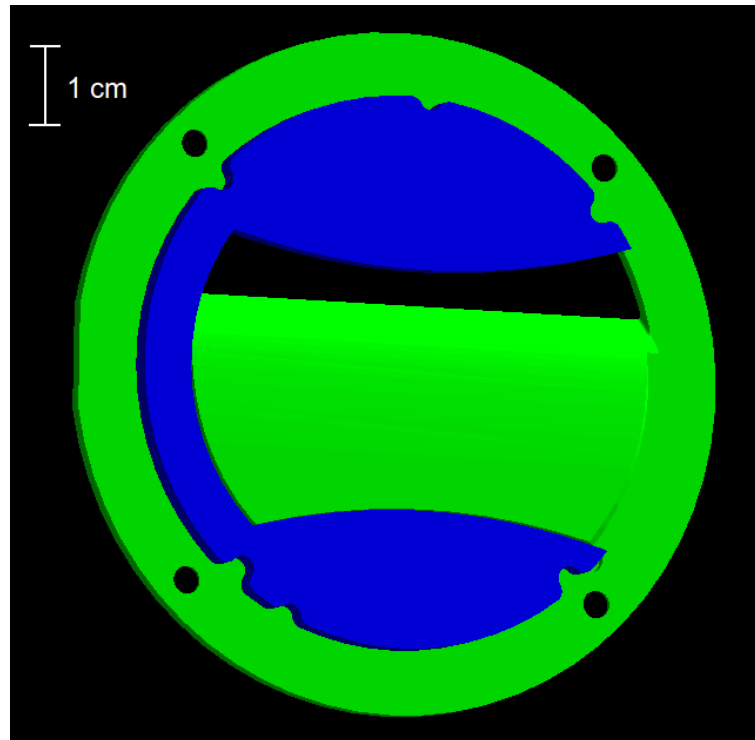


Figure 3.4: Primary aperture (blue) and flattening filter (green) in GATE.

3.5.3 Collimator jaws and exit window

The collimator jaws made of lead were modeled by medPhoton and imported in GATE using the STL file format. Their geometry is shown in figure 3.5.

To confine the X-ray head, an exit window consisting of a 0.5 mm thin disc of polycarbonate was used. This marked the outermost layer.

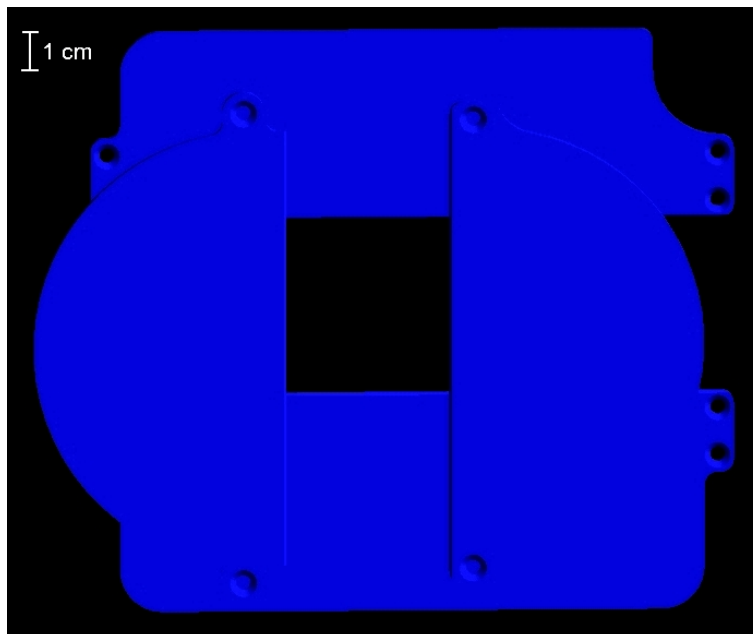


Figure 3.5: Collimator jaws in GATE.

3.6 Efficiency

While the upside of the chosen method of simulating an electron beam is enhanced accuracy, its major downside is efficiency. Simulating electrons requires a lot of processing power, thus when multiple simulations of high accuracy are needed, computing time becomes an issue. Hence, efficiency is of great importance. This section describes the method used to evaluate and improve the efficiency.

In the first step, the number of produced X-ray photons per incident electron was assessed. The X-ray anode was simulated for energies between 40 keV and 120 keV in steps of 10 keV. A thin spherical shell was placed around the anode and a fluence actor was activated inside the shell. This actor counts every particle that passes its volume and thus counts every X-ray photon leaving the anode. To eliminate unwanted electrons from the count, another spherical shell was placed between the first shell and the anode. A kill actor for electrons was activated in this volume, eliminating all electrons before they contribute to the particle count. Consequently only photons were registered. This process is illustrated in figure 3.7.

For each energy, the efficiency η of the anode was calculated from the data as the number of X-ray photons per primary electron.

In a second step, splitting was introduced. Splitting is a variance reduction technique. Every time a primary particle interacts with the anode volume, the interac-

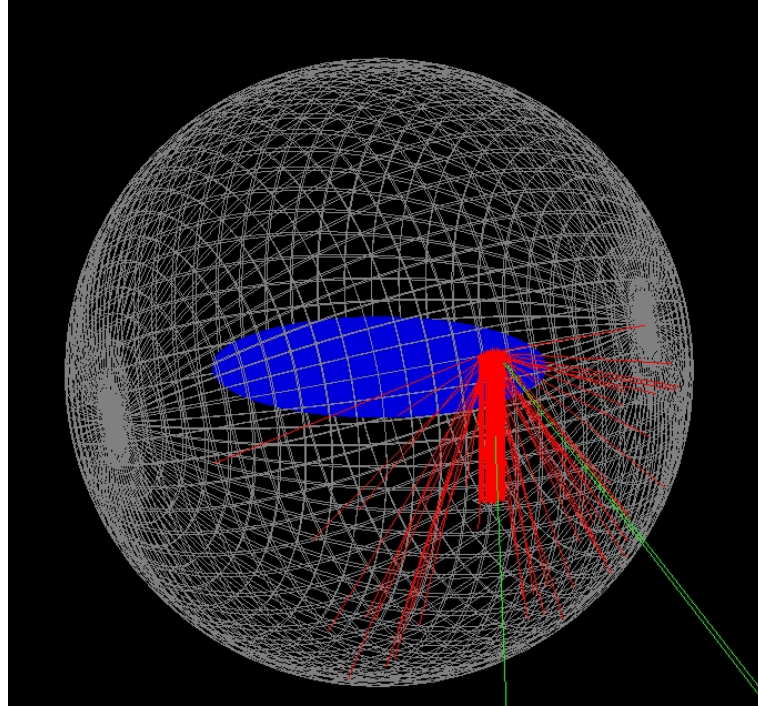


Figure 3.6: Evaluation of the efficiency of the simulated anode. The electron beam (red) hits the anode (blue). Many electrons are deflected but are eliminated before they leave the sphere. The photons (green) exit the sphere and contribute to the particle count.

tion is repeated n times, where n is the splitting factor. Therefore, every time an electron would create a photon, n photons are created instead. The new photons have the same point of origin but different energies and directions. All photons are weighted by a factor of $\frac{1}{n}$, so they contribute less to actors that take weight into account e.g. not to change the total dose.

As a dedicated splitting command was not implemented for GATE version 8.0, the GEANT4 command `"/process/em/setSecBiasing"` was used to activate splitting for both bremsstrahlung and electron ionization.

Splitting was tested for splitting factors n of 1 (no splitting), 10^2 , 10^3 , 10^4 and 10^5 . For each factor the computing time per primary electron t_e was evaluated. The effective X-ray photons per second $\frac{dN}{dt}$ can then be calculated from equation 3.1, where η is the previously calculated efficiency of the anode.

$$\frac{dN}{dt} = \frac{n * \eta}{t_e} \quad (3.1)$$

These values were then evaluated to find the splitting factor associated with maximum efficiency.

To rule out possible artefacts from high splitting factors, the spectrum was recorded with an energy spectrum actor, and the HVL_{AI} were evaluated with a dose actor as described in chapter 4 and compared to simulations of same variance and without splitting.

The number of photons per primary electron in GATE, depending on the electron energy, can be seen in figure 3.7. The theoretical result is given by equation 3.2 from [36], where η is the efficiency, $k = 1.1 \cdot 10^{-9}$ is a constant based on experimental data, $Z = 74$ for tungsten and U is the maximum voltage of the X-ray tube. Compared to the theoretical result, the simulation overestimated the efficiency of the anode by up to 20%.

$$\eta = k * Z * U \quad (3.2)$$

This effect may be caused by the monochromatic electron beam used in the simulation. Equation 3.2 is based on experimental data from X-ray tubes that most likely do not have a perfectly monochromatic electron beam. The average voltage for a monochromatic beam is equal to the maximum voltage and thus higher than for a polychromatic beam of the same maximum voltage. As equation 3.2 only considers the maximum voltage, the simulation will result in a higher efficiency. Further aspects associated with having a monochromatic beam are also addressed in chapter 4.

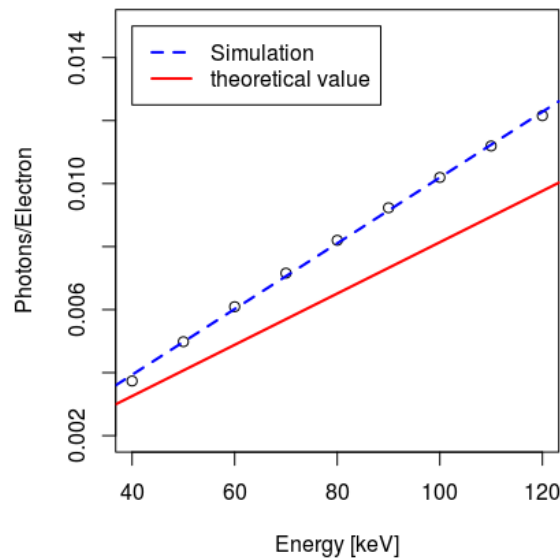


Figure 3.7: Efficiency of the anode for different energies as simulated in GATE.

The number of photons per primary electron for different splitting factors in GATE can be seen in figure 3.8. A data table can be found in appendix A.4. Efficiency greatly improved up to factors of 10^3 but only improved marginally for factors greater than 10^3 and declined for splitting factors greater than 10^4 . A splitting factor of 10^3 was chosen for all simulations. Simulations with this splitting factor showed no deviations in HVL_{A1} or energy spectrum compared to simulations without splitting.

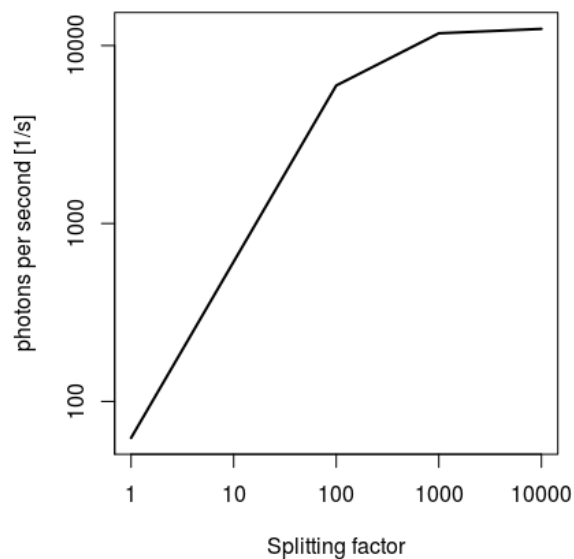


Figure 3.8: Efficiency of different splitting factors in GATE. Both axes are logarithmic.

4. Half value layer

The energy spectrum is a key factor in the applicability of the established model of the X-ray head. To investigate the head scatter of the ImagingRing™ System an accurate energy spectrum is needed .

While the spectrum can be easily obtained in the simulation, direct measurements of the X-ray spectrum are challenging. To compensate for this, several HVL_{Al} were measured experimentally as well as simulated in GATE. These values were then used to evaluate and improve the Monte Carlo model.

4.1 Experiments

HVLs in mm aluminum (HVL_{Al}) were measured with the NOMEX Multimeter. It was placed on the patient couch and its crosshair was positioned in the central beam. The experimental setup is shown in figure 4.1. Figure 4.2 shows an X-ray image of the NOMEX multimeter. Before irradiation, a warmup was performed for the X-ray source, to ensure stable operating conditions.

The HVL_{Al} were then measured for tube voltages of 60 kV, 80 kV, 100 kV and 120 kV. Each measurement was averaged over 50 pulses, with each pulse lasting for 10 ms.

As the ImagingRing™ System has two cathodes, the X-ray spectrum might differ depending on which cathode is in use. For this reason, all HVL_{Al} were evaluated for both the small focal spot (one cathode, 20 mA tube current) and the large focal spot (both cathodes, 40 mA tube current).

The set of measurements was performed for four different filters:

- Air
- 3 mm aluminum

- 0.5 mm copper
- 3 mm aluminum + 0.5 mm copper

Each filter specifies material and thickness of filtration placed in the X-ray beam. All filters used were of high purity and were placed on top of the NOMEX multimeter.

The entire process was performed twice on the ImagingRing™ System. One time with collimator jaws, primary aperture and flattening filter in place and one time after removing them from the system. By doing so, the spectrum could be characterized for both the raw source and the entire X-ray head.

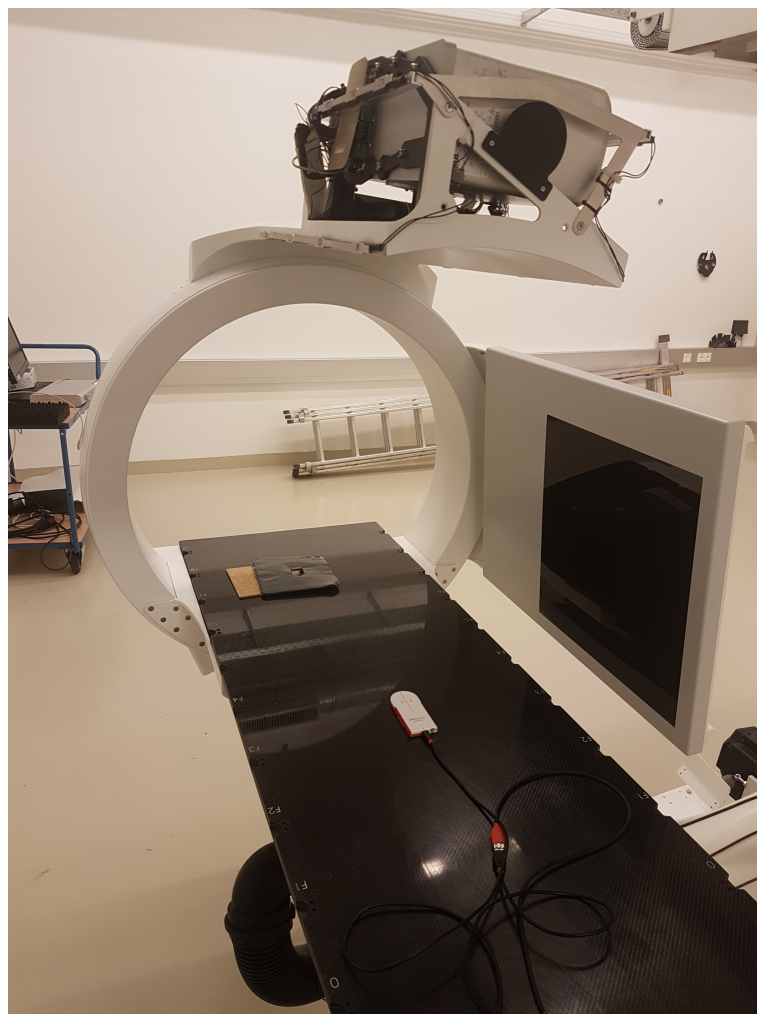


Figure 4.1: Experimental setup of HVL_{A1} measurements. The NOMEX Multimeter was placed on the patient couch, in the central beam of the X-ray source.

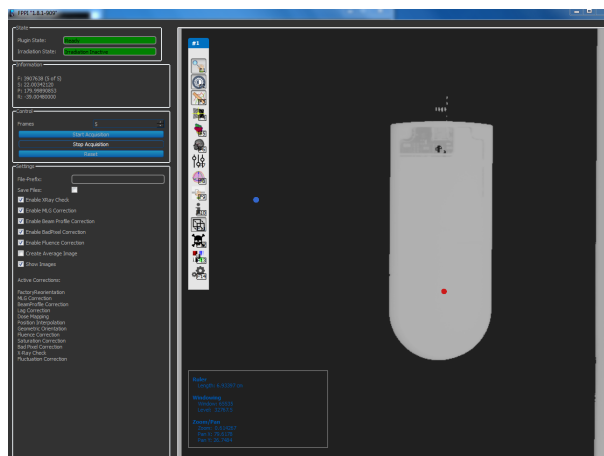


Figure 4.2: X-ray image of the NOMEX multimeter. The red dot marks the central beam.

4.2 Results of experiments

The measured HVL in aluminum for the ImagingRing™ System without primary collimator, flattening filter and collimator jaws for tube currents of 20 mA and 40 mA can be found in table 4.1 and 4.2.

Table 4.1: HVL_{Al} values measured on the ImagingRing™ System without primary collimator, flattening filter and collimator jaws for a tube current of 20 mA (small focal spot). All empirical standard deviations were below 0.1 mm

Energy [keV]	60	80	100	120
HVL_{Al} [mm] - unfiltered	3.5	5.1	5.9	6.8
HVL_{Al} [mm] - 3 mm Al	2.2	2.8	2.9	4.4
HVL_{Al} [mm] - 0.5 mm Cu	5.3	6.6	7.8	9.0
HVL_{Al} [mm] - 3 mm Al + 0.5 mm Cu	5.5	6.9	8.1	9.2

Table 4.2: HVL_{Al} values measured on the ImagingRing™ System without primary collimator, flattening filter and collimator jaws for a tube current of 40 mA (large focal spot). All empirical standard deviations were below 0.1 mm

Energy [keV]	60	80	100	120
HVL_{Al} [mm] - unfiltered	3.0	4.4	6.7	
HVL_{Al} [mm] - 3 mm Al	2.5	3.0	3.8	4.8
HVL_{Al} [mm] - 0.5 mm Cu	5.2	6.9	8.4	9.4
HVL_{Al} [mm] - 3 mm Al + 0.5 mm Cu	5.4	7.2	8.6	9.7

The measured HVL_{Al} for the unfiltered spectrum are significantly higher than for the

spectrum filtered by 3 mm of aluminum. For a tube current of 40 mA no value could be measured at all. As added filtration removes the low energy components of the spectrum and thus increases the HVL_{Al} , these results are counter-intuitive. This suggests that the NOMEX Multimeter requires a minimum filtration to produce accurate results. For this reason, the unfiltered values are disregarded in further examinations. As filtration is mandatory in medical imaging, this does not represent a limitation in most cases.

The deviation in HVL_{Al} for different tube currents suggests a difference in tube voltages. This might be the result of the two cathodes used as described in 2.1. On average the HVL_{Al} were 6 % higher for the large focal spot as can be seen in figure 4.3.

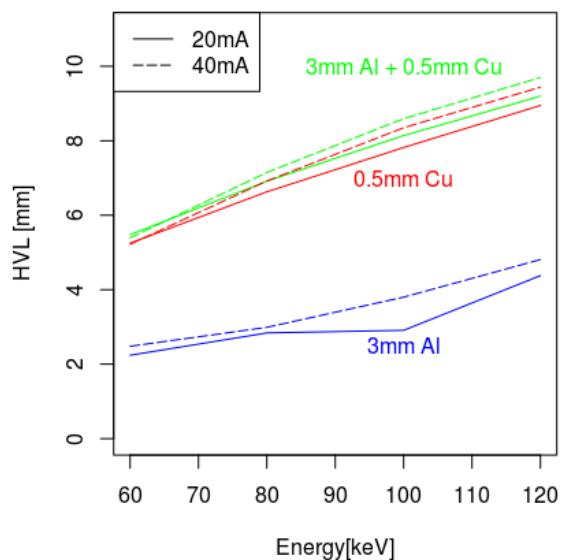


Figure 4.3: HVL_{Al} without flattening filter and primary collimator for different filtration and tube currents

The measured HVL in aluminum with primary collimator, flattening filter and collimator jaws included for tube currents of 20 mA and 40 mA can be found in tables 4.3 and 4.4.

With flattening filter and primary collimator in place, the NOMEX Multimeter was able to measure the HVL_{Al} accurately even without additional filtration.

However, the dependency on the tube current still persisted and amounted up to 3% as can be seen in figure 4.4.

Table 4.3: HVL_{Al} values measured on the ImagingRing™ System with primary collimator, flattening filter and collimator jaws for a tube current of 20 mA (small focal spot). All empirical standard deviations were below 0.1 mm

Energy [keV]	60	80	100	120
HVL_{Al} [mm] - unfiltered	3.0	4.0	4.7	5.6
HVL_{Al} [mm] - 3 mm Al	3.6	4.9	5.6	6.7
HVL_{Al} [mm] - 0.5 mm Cu	5.5	7.4	8.6	9.8
HVL_{Al} [mm] - 3 mm Al + 0.5 mm Cu	5.7	7.6	8.9	10.0

Table 4.4: HVL_{Al} values measured on the ImagingRing™ System with primary collimator, flattening filter and collimator jaws for a tube current of 40 mA (large focal spot). All empirical standard deviations were below 0.1 mm

Energy [keV]	60	80	100	120
HVL_{Al} [mm] - unfiltered	3.1	4.1	5.0	5.9
HVL_{Al} [mm] - 3 mm Al	3.7	5.0	5.9	6.9
HVL_{Al} [mm] - 0.5 mm Cu	5.5	7.5	8.8	10.0
HVL_{Al} [mm] - 3 mm Al + 0.5 mm Cu	5.6	7.7	9.1	10.2

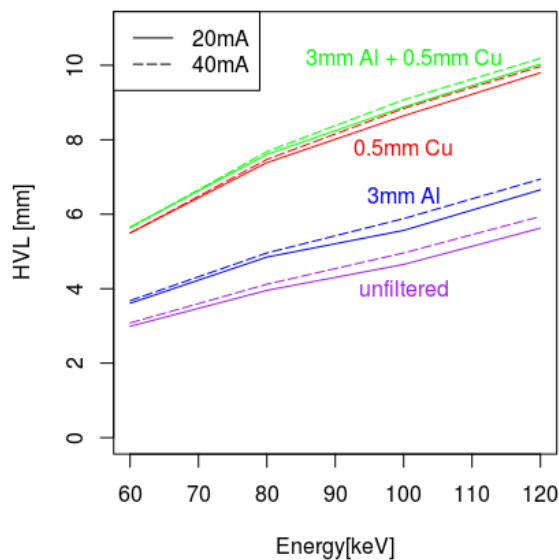


Figure 4.4: HVL_{Al} with flattening filter and primary collimator for different filtration and tube currents

4.3 Simulations

For HVL_{Al} simulations, two different approaches were tested. In the first approach, a monoenergetic electron beam was used. In the second approach, a superposition of weighted electron energies was determined through optimization. For both approaches HVL_{Al} were evaluated and compared to experimental data.

4.3.1 Monoenergetic approach

In this approach, the electron energy spectrum was simply approximated by an ideal monoenergetic peak corresponding to the tube voltage.

For HVL_{Al} simulations in GATE a block of aluminum was placed in the beam. A dose actor was then activated in this volume. The actor registered the deposited energy depending on the depth and stored the information. This setup is illustrated in figure 4.5.

For each layer GATE provides the sum of deposited energies, the sum of squares of the deposited energy and the number of particle hits. From this data an empirical standard deviation was calculated by linear error propagation through numerical derivation. This deviation only reflects the statistical deviation and allows no conclusion on systematic errors.

To evaluate the HVL_{Al} , the distance between the layer of maximum absorption and the layer closest to half the maximum was assessed. Linear interpolation was used in between points. This distance represents the HVL_{Al} .

Corresponding to the experimental setup, four different filters were used: no filter, 3 mm aluminum, 0.5 mm copper, 3 mm aluminum + 0.5 mm copper. As the dose actor in GATE stores the deposited energy in each layer, there is no difference between using a 3 mm Al filter and evaluating the dose curve in aluminum at a depth of 3 mm. Hence only two simulations were needed to measure all four settings - one with copper filter and one without.

The same number of particles has been used for all filters and energies. To achieve comparable statistical certainties in all simulations, the detector resolution was chosen relative to the penetration depth. In direction parallel to the beam a detector resolution of one percent of the expected HVL_{Al} was chosen for all simulations.

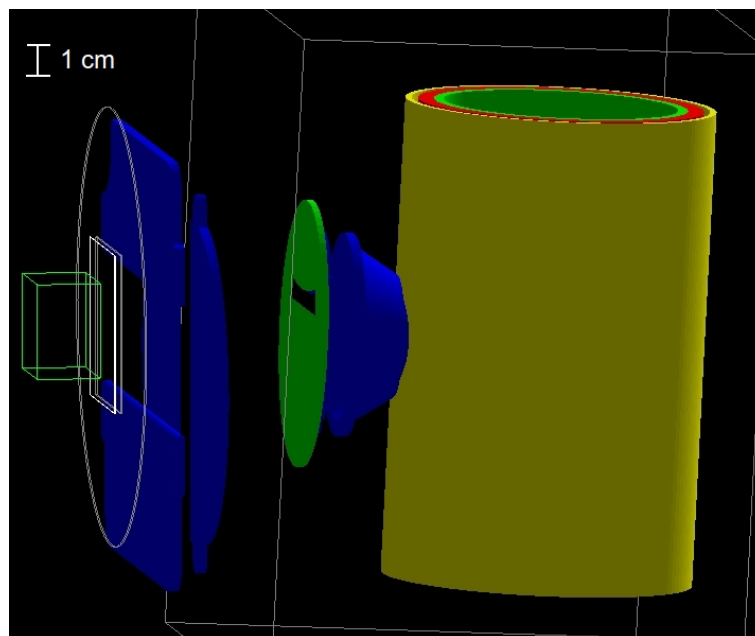


Figure 4.5: Simulation of HVL_{Al} measurements. From left to right: cuboid block of aluminum (green), copper filter (white square), polycarbonate exit window (white circle), collimator jaws (blue), primary collimator (green), flattening filter (blue), exit cone (blue), lead cylinder (yellow), oil (red), glass (green).

4.3.2 Energy weighting approach

In the second approach, the electron energy spectrum was approximated by a linear combination of discrete energies E_i between 40 keV and 120 keV in steps of 10 keV. The linear coefficients were called weighting factors $\omega(E_i)$ with $\sum_i \omega(E_i) = 1$. Example spectra are shown in figure 4.6. Energies below 40 keV were disregarded, as the resulting X-ray photons were filtered out by the inherent filtration of the tube and the flattening filter, respectively.

For an electron energy spectrum of a single discrete energy, the probability for a newly created electron in GATE to have the discrete energy E_i equals 1. For a linear combination of discrete energies, the probability $P(E_i)$ equals the weighting factor $\omega(E_i)$.

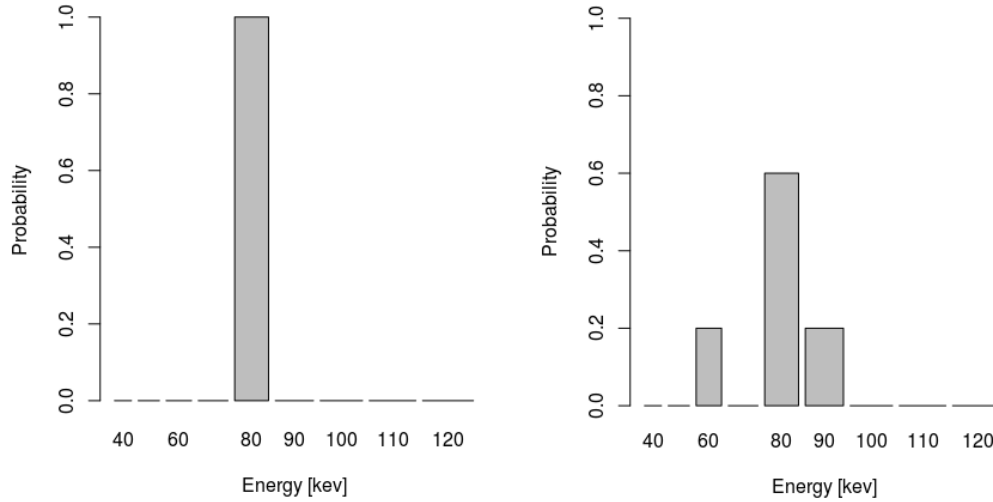


Figure 4.6: Left: a monoenergetic energy spectrum with $\omega(80keV) = 1$, Right: linearcombination of three energies with $\omega(60keV) = 0.2$, $\omega(80keV) = 0.6$ and $\omega(90keV) = 0.2$

Simulating all energies E_i between 40 keV and 120 keV in steps of 10 keV and weighting factors $\omega(E_i)$ between 0 and 1 in steps of 0.1 directly in GATE requires extensive computing power. The number of possible combinations is given by $\binom{18}{10}$, amounting to a computing time of over 2500 years on a standard CPU.

This issue was solved by simulating each discrete energy separately and afterwards combining it in R. This was possible, as the dose actor in GATE saves the deposited energy for each layer of the detector. Hence, if the dimensions of the layers remain the same and the deposited energy is scaled by the number of primary particles, the deposited energy depth curves for two discrete energies E_1 and E_2 in the detector can be weighted with the corresponding weighting factors ω_1 and ω_2 and added up as illustrated in figure 4.7. The new curve then represents the depth dose of a mixed spectrum $E = \omega_1 E_1 + \omega_2 E_2$. From this curve the HVL_{A1} can be calculated.

To compare the simulated HVL_{A1} to the experimental data, a cost function was defined in equation 4.1, where $HVL_{exp,i}$ is the experimentally measured HVL_{A1} for filter setting i and $HVL_{sim,i}$ is the simulated one.

$$C = \sum_i \left(\frac{HVL_{exp,i} - HVL_{sim,i}}{HVL_{exp,i}} \right)^2 \quad (4.1)$$

The cost function was then minimized using a combination of a modified quasi-Newton BFGS method [6] and simulated annealing. The resulting weighting factors

then represent the closest approximation to the experimental data.

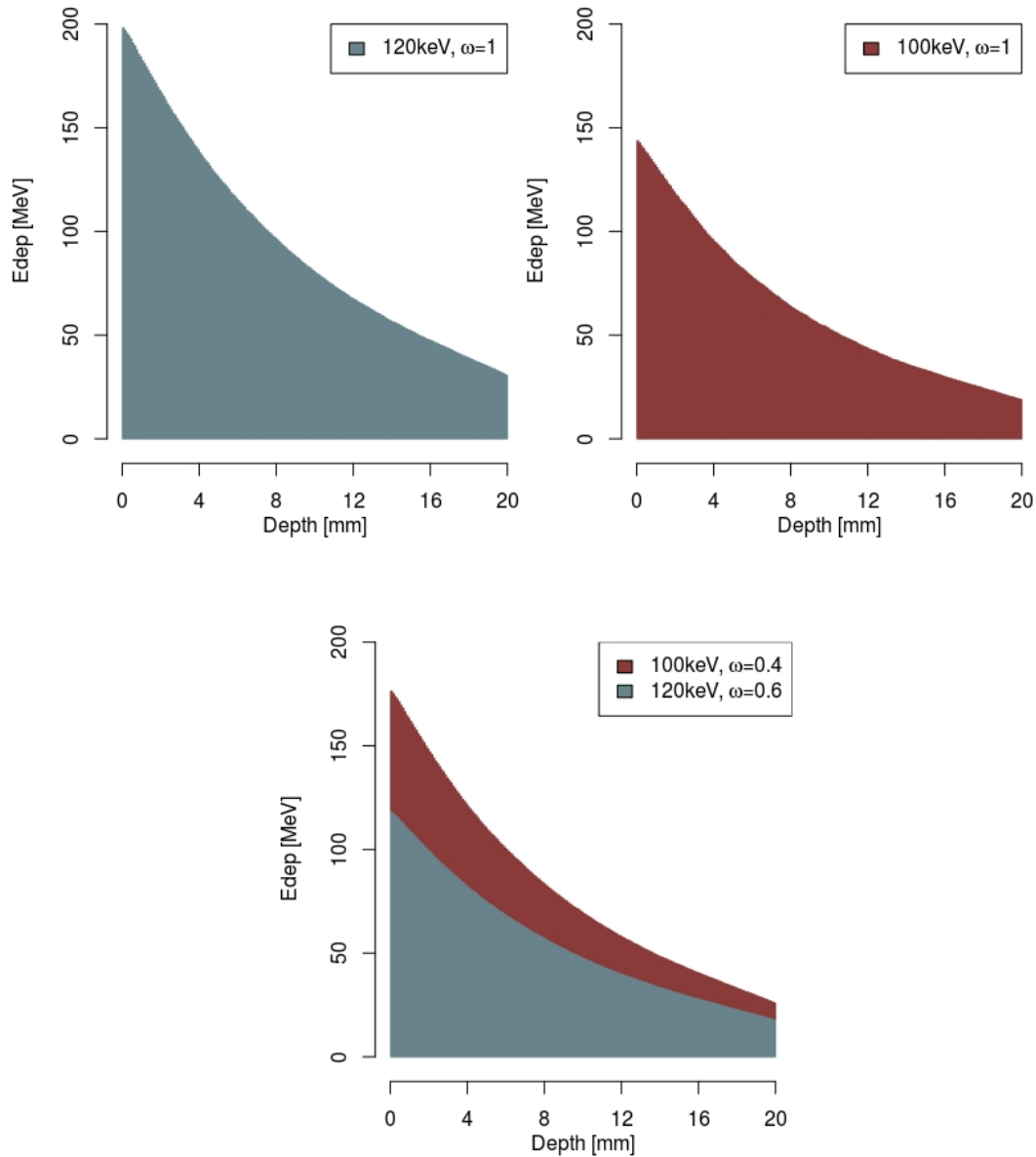


Figure 4.7: Deposited energy in aluminum. Left: monoenergetic electron beam of $E_1 = 120\text{keV}$ and $\omega_1 = 1$, Right: monoenergetic electron beam of $E_2 = 100\text{keV}$ and $\omega_2 = 1$, Bottom: Example of a linear combination of electron energies. $E_1 = 120\text{keV}$, $\omega_1 = 0.6$ and $E_2 = 100\text{keV}$, $\omega_2 = 0.4$

4.4 Results of simulations and discussion

4.4.1 Results of the monoenergetic approach

The results of the HVL_{Al} simulation can be found in tables 4.5 and 4.6. The relative deviation of simulated HVL_{Al} and experimentally measured HVL_{Al} averaged over all filter settings, was between 14% to 28%, with the simulated values being strictly larger than the measured values.

Table 4.5: Simulated HVL_{Al} values without primary collimator and flattening filter and mean relative deviation between simulation and experiment. All empirical standard deviations were below 0.1 mm

Energy [keV]	60	80	100	120
HVL_{Al} [mm] - 3 mm Al	3.6	4.6	5.4	6.1
HVL_{Al} [mm] - 0.5 mm Cu	5.3	7.4	8.7	9.7
HVL_{Al} [mm] - 3 mm Al + 0.5 mm Cu	6.3	8.2	9.3	10.0
mean relative deviation to experiment	24%	28%	26%	15%

Table 4.6: Simulated HVL_{Al} values with primary collimator and flattening filter and mean relative deviation between simulation and experiment. All empirical standard deviations were below 0.1 mm

Energy [keV]	60	80	100	120
HVL_{Al} [mm] - unfiltered	4.3	5.7	6.8	7.7
HVL_{Al} [mm] - 3 mm Al	4.6	5.8	7.0	7.7
HVL_{Al} [mm] - 0.5 mm Cu	5.6	7.8	9.2	10.1
HVL_{Al} [mm] - 3 mm Al + 0.5 mm Cu	6.5	8.6	9.6	10.3
mean relative deviation to experiment	26%	27%	20%	14%

4.4.2 Results of energy weighting approach

The results of the HVL_{Al} simulation for the energy weighting approach can be found in tables 4.7 and 4.8. It resulted in a close approximation with average deviations from the experimentally measured HVL_{Al} of under 4%. This was a major improvement to the previously simulated HVL_{Al} values from chapter 4.4 with average deviations of 23%.

Table 4.7: Simulated HVL_{Al} values without primary collimator and flattening filter and mean relative deviation between simulation and experiment. All empirical standard deviations were below 0.1mm

Energy [keV]	60	80	100	120
HVL_{Al} [mm] - 3 mm Al	2.5	3.0	3.4	4.6
HVL_{Al} [mm] - 0.5 mm Cu	4.6	6.2	7.8	9.0
HVL_{Al} [mm] - 3 mm Al + 0.5 mm Cu	6.1	7.6	8.8	9.6
mean relative deviation	9%	5%	2%	1%

Table 4.8: Simulated HVL_{Al} values with primary collimator and flattening filter and mean relative deviation between simulation and experiment. All empirical standard deviations were below 0.1 mm

Energy [keV]	60	80	100	120
HVL_{Al} [mm] - unfiltered	3.2	4.1	4.9	5.9
HVL_{Al} [mm] - 3 mm Al	3.6	4.7	5.5	6.5
HVL_{Al} [mm] - 0.5 mm Cu	4.9	7.2	8.6	9.9
HVL_{Al} [mm] - 3 mm Al + 0.5 mm Cu	6.1	8.0	9.2	10.2
mean relative deviation	7%	3%	2%	2%

4.4.3 Discussion

A possible explanation for the deviation in HVL_{Al} in the monoenergetic approach might be the backscatter of electrons.

In X-ray tubes, a significant amount of electrons is backscattered upon impact on the anode, losing some of their energy in the process [12]. If they remain inside the electric field between cathode and anode, they are accelerated back towards the anode, where they impact again. Such electrons have lower energies and thus shift the X-ray spectrum towards lower energies, resulting in lower HVL_{Al} values.

However, the simulation of electric fields and accurate backscatter models are not fully implemented in GATE [34]. Because of this, backscattered electrons cannot reach the anode and do not contribute to the X-ray spectrum, potentially causing a deviation between simulation and experiment.

These deviations from the experimental data suggest that the effect on the HVL_{Al} caused by the backscattered electrons, which was neglected in the first approach, might be significant. Thus, accounting for it was an integral part of the modeling process.

In the second approach, possible low energy electrons that result from backscatter are accounted for. Thus the resulting HVL_{Al} are in better agreement with experimental

data.

However, the approach resulted in an unexpected strong representation of low electron energies. Figure 4.8 displays the weighted electron energy spectrum for an X-ray beam with the maximum energy of 120 keV.

A possible explanation is the overestimation of the filtration by the GEANT4 physics models, resulting in overall higher HVL_{Al} values. To compensate, the weighting approach would increase the weighting of low energies by increasing the corresponding weighting factors. Low energies however contribute less to the overall deposited energies as less photons reach the detection volume. As a result, their share is increased out of proportion in order to have the desired impact on lowering the HVL_{Al} values.

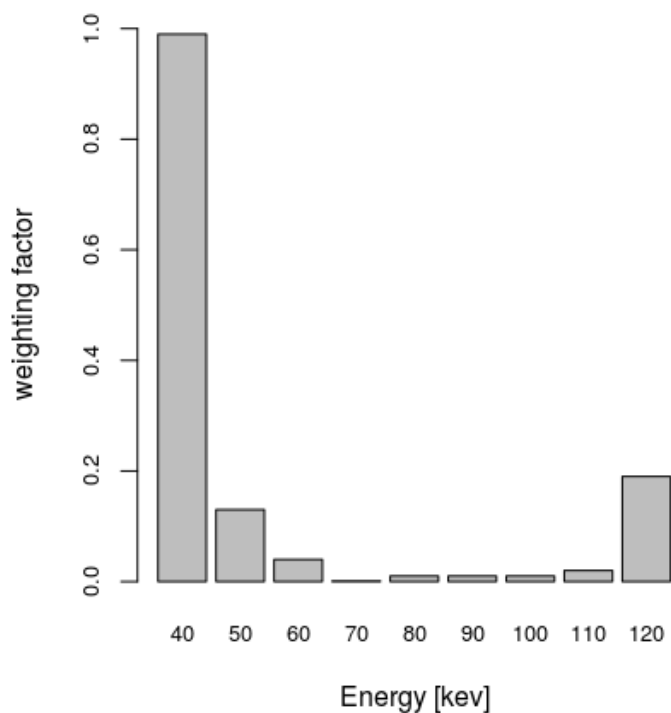


Figure 4.8: Weighting factors of an optimized electron energy spectrum for a tube voltage of 120kV.

5. Focal spot

The filament of an X-ray cathode has a fixed length and width. As a result, the cross section of the electron beam penetrating the tungsten anode deviates from the cross section of an infinitely thin pencil beam. Thus, the projection onto the anode called focal spot is spread out over a small area. The X-rays emerging from the anode originate not from a single point but from an area instead.

Image reconstruction requires precise knowledge of the origin of the X-rays. Thus, the shape of the focal spot as well as the out-of-focus radiation have a strong impact on image quality and are key factors in image processing. For this reason, the focal spot was evaluated and included in the simulation by the methods described in this chapter.

5.1 Experiments

The size and shape of the focal spot was measured in an experiment so it could subsequently be modeled in GATE. The experiments were performed in research room "IR1" at MedAustron.

The source of the ImagingRing™ System was positioned at an angle of 5.8° (corresponding to 95.84° in ImagingRing™ System coordinates) below the horizontal line to compensate for the 5.84° tilt of the source described in 2.1, resulting in a horizontal central beam. The detector was positioned on the other side of the patient couch, parallel to the exit window of the source (corresponding to 275.84° in ImagingRing™ System coordinates). The longitudinal position of the ImagingRing™ System was 25.82 cm.

Two indexing bars were put in positions H1 and F1 [41]. Then, a slit-camera (PTW, Freiburg, Germany), consisting of a disc of lead with a 0.7 cm long slit mounted on a stand, was placed on the patient couch between the indexing bars.

The center of the slit was positioned in the central beam of the source and moved towards the exit window as closely as possible, resulting in the distance of exit

window to slit camera of 1.0 cm. The distance between holder surface and grid board surface was adjusted to 17.2 cm [39]. The experimental setup can be seen in figure 5.1.

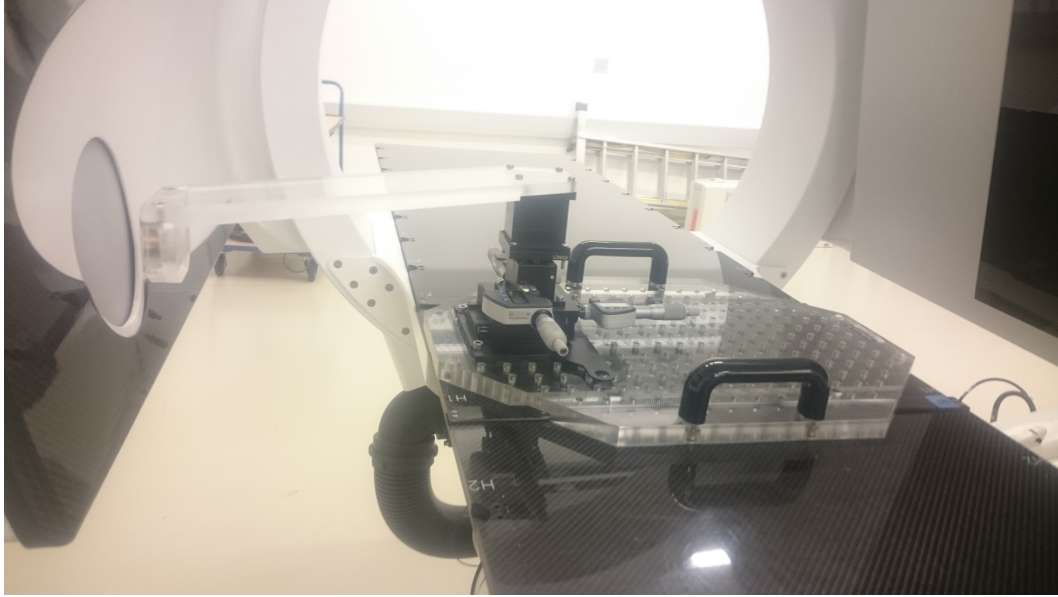


Figure 5.1: Experimental setup of the focal spot measurements: the X-ray head on the left side was placed in a horizontal position, with the slit camera directly next to the exit window. The detector was positioned parallel.

Data was collected for energies between 60 keV and 120 keV in steps of 10 keV and averaged over 5 pulses of 10 ms duration each. The slit was positioned vertically to measure the vertical dimension of the focal spot as well as horizontally to measure its horizontal dimension. Each experiment was performed for the small focal spot at a tube current of 20 mA and the large focal spot at 40 mA.

Furthermore, the focal spot size was measured for a tube voltage of 100 kV and tube currents of 10 mA, 15 mA, 20 mA, 25 mA, 40 mA, 60 mA and 80 mA. Finally, the irradiation time was varied between 10 ms and 25 ms in steps of 5 ms with a fixed tube voltage of 100 kV and for both focal spots.

The size of the projection of the slit onto the detector was defined to be the distance between the two points at which the intensity was equal to 15% of its maximum. This distance was then converted to the actual focal spot size by application of the enlargement factor $f_{enlargement}$ described in equation 5.1.

$$f_{enlargement} = (D_{SD} - D_{SE} - L_{slit}/2 - D_{ES}) / (D_{SE} + L_{slit}/2 + D_{ES}) \quad (5.1)$$

where D_{SD} is the source to detector distance of 103.86 cm, D_{SE} is the source to exit window distance of 11.41 cm, L_{slit} is the length of the slit of 0.7 cm and D_{ES} is the exit window to slit distance of 1.0 cm. All distances result from the geometry of the ImagingRing™ System and were supplied by the vendor, with the exception of D_{ES} , which was measured using a ruler.

5.2 Results of experiments

The mean vertical and horizontal length of the small and large electron focal spot can be found in table 5.1.

The standard deviation was about ± 0.01 mm for all measurements. However, the uncertainty in the distance between slit camera and exit window contributed to an additional uncertainty, resulting in an overall uncertainty of ± 0.02 mm.

The profile of both small and large focal spot in horizontal as well as vertical direction are shown in figures 5.2 and 5.3. The small focal spot in horizontal direction exhibits two bumps, one on each side. The width at 15% of the maximum was therefore approximated as the width of the normal distribution which was fitted to the high intensity part of the profile.

Detailed results on the effects of tube voltage, tube current and irradiation time are displayed in radar charts figs. 5.4 to 5.9. Radar charts are a useful method of displaying multivariate data and enable easy identification of outliers through asymmetry [7].

Table 5.1: Focal spot size of the small and large focal spot measured with a slit camera and the detector of the ImagingRing™ System. All empirical standard deviations were below 0.1 mm.

	vertical length [mm]	horizontal length [mm]
small focal spot	0.6	0.7
large focal spot	1.1	0.9

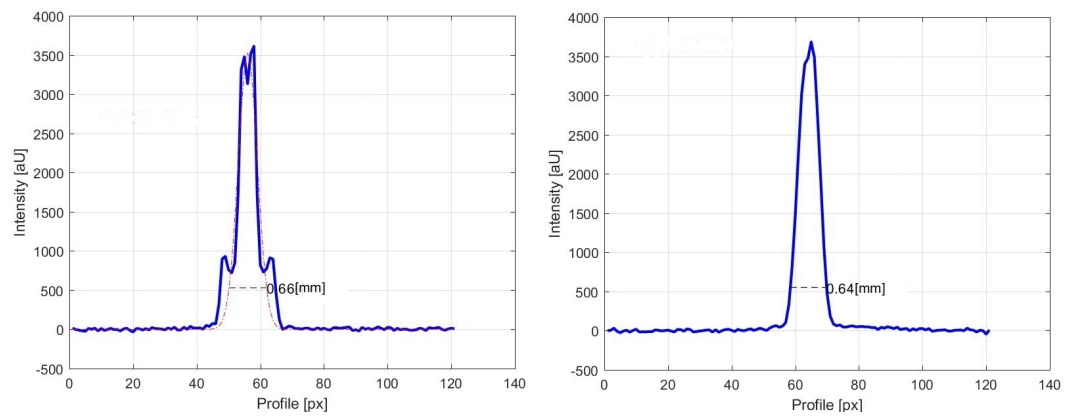


Figure 5.2: Profile of the small focal spot. Left: in horizontal direction. Right: in vertical direction.

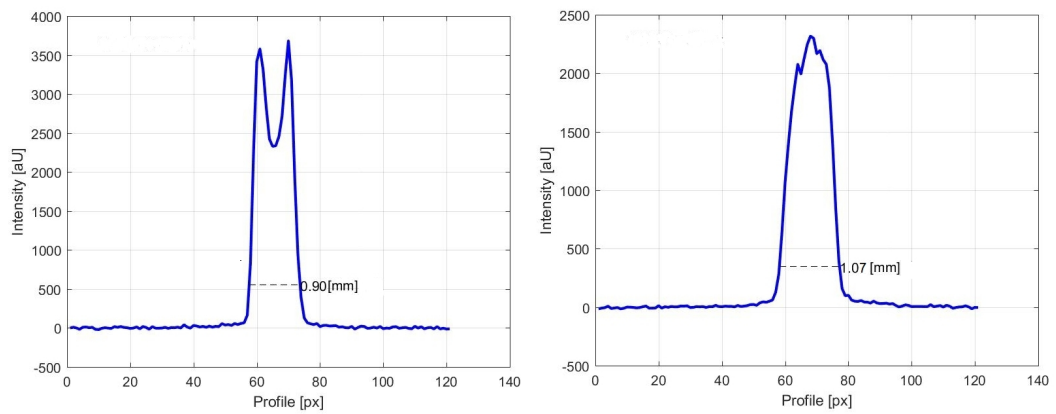


Figure 5.3: Profile of the large focal spot. Left: in horizontal direction. Right: in vertical direction.

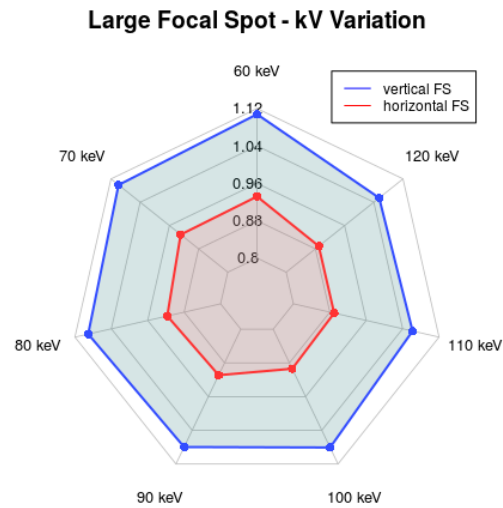


Figure 5.4: Vertical (blue line) and horizontal (red line) length in [mm] of the large focal spot (FS) for varying tube voltages.

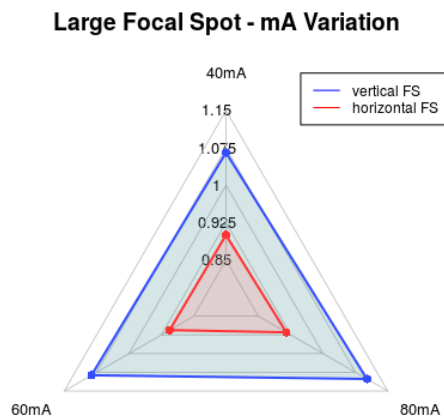


Figure 5.5: Vertical (blue line) and horizontal (red line) length in [mm] of the large focal spot (FS) for varying tube currents.

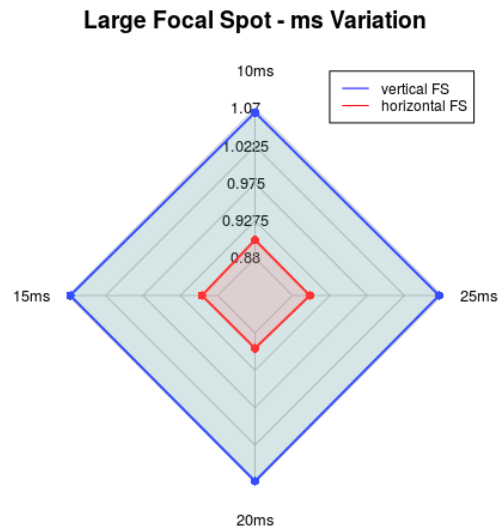


Figure 5.6: Vertical (blue line) and horizontal (red line) length in [mm] of the large focal spot (FS) for varying irradiation times.

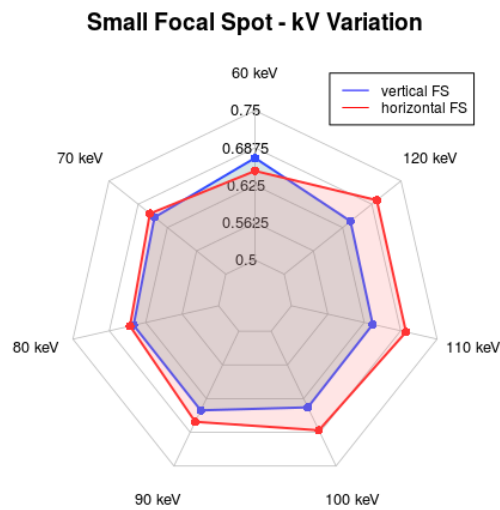


Figure 5.7: Vertical (blue line) and horizontal (red line) length in [mm] of the small focal spot (FS) for varying tube voltages.

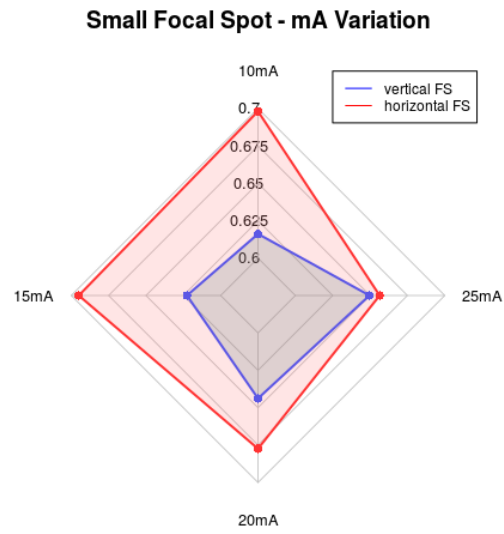


Figure 5.8: Vertical (blue line) and horizontal (red line) length in [mm] of the small focal spot (FS) for varying tube currents.

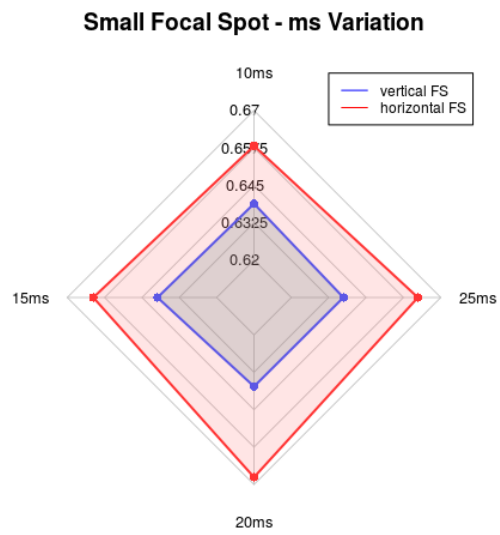


Figure 5.9: Vertical (blue line) and horizontal (red line) length in [mm] of the small focal spot (FS) for varying irradiation times.

5.3 Simulations

The nonzero dimension of cathode and anode results in a spread out electron focal spot. To account for this effect, the focal spot was modeled in the simulation by fitting the shape of the electron beam to the data obtained in the slit-camera experiment. This was done by executing the following method:

From the slit-camera experiment, the profile of the focal spot in both horizontal and vertical direction was obtained. In the first step, this profile was approximated in the software tool R by a superposition of normal distributions as shown in equation 5.2. The number n of normal distributions used was chosen greater or equal to the number of peaks in the profile. Each distribution was characterized by three parameters: mean value μ_i , standard deviation σ_i and height a_i . The parameter values were then determined by a least squares fit and BFGS optimization [6]. Results of the fitting process are illustrated in figure 5.10.

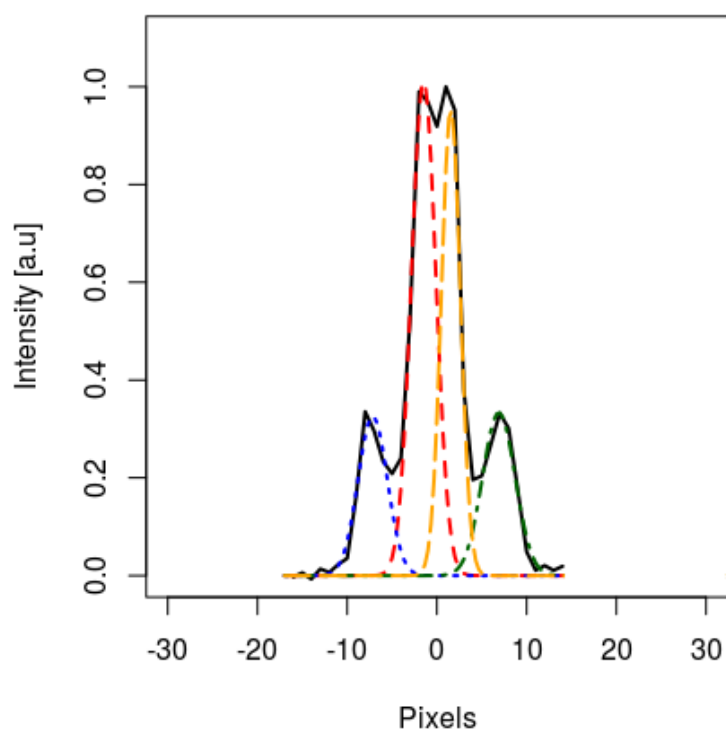


Figure 5.10: Approximation of the experimentally measured profile of the small focal spot (black, solid line) by four normal distributions (red, blue, green and yellow dashed or dotted lines).

$$FocalSpot_{approx} = \sum_{i=1}^n a_i * \exp\left(-\frac{(x - \mu_i)^2}{2 * \sigma_i^2}\right) \quad (5.2)$$

In horizontal direction, the experimentally found width of the focal spot is the result of a projection of the electron beam onto the 10° tilted anode. This projection is illustrated in figure 5.11. In order to get the actual width of the electron beam, a factor $s = \frac{1}{\tan(10^\circ)}$ was applied.

Then, the electron beam was modeled in GATE by adding n electron sources of type "beam" and shape "circle". The position of source i was equal to $x_i = s * \mu_i$ and the intensity $int_i = a_i * \sigma_i$. The standard deviation for both directions was set to be $std_{hor,i} = s * \sigma_{hor,i}$ in horizontal direction and $std_{ver,i} = \sigma_{ver,i}$ in vertical direction.

In the final step, the simulation was evaluated against experimental data. In order to do so, a production- and stop-actor was activated in the entire anode volume. The actor registered the origin of every secondary particle whenever one was created. It was combined with a filter for photons, to limit the detection to X-ray photons. As a result, all photons created inside the anode were detected by the actor.

The volume of origin for all photons is equal to the experimentally measured focal spot only if the created photons actually exit the anode volume and contribute to the X-ray beam. If the penetration depth of the electron beam is of the same order of magnitude as the size of the focal spot, the chosen method might not be accurate for the size of the focal spot in horizontal direction, as photons created deep inside the anode material might not be able to exit it. For this reason, the penetration depth of electrons had to be examined to rule out this possible source of error. This was done in a separate simulation, by irradiating a tungsten cube with an electron beam while examining the depth in which X-ray photons were created.

The profile of the focal spot was examined in R by evaluating the number of produced particles along vertical and horizontal lines close to the point of maximum production. Results were averaged over multiple lines to reduce variance. The resulting graphs allowed the evaluation of the size of the focal spot by assessing the distance between the two points where the production had decreased to 15% of its maximum, as it was done in the experiment from chapter 5.1.

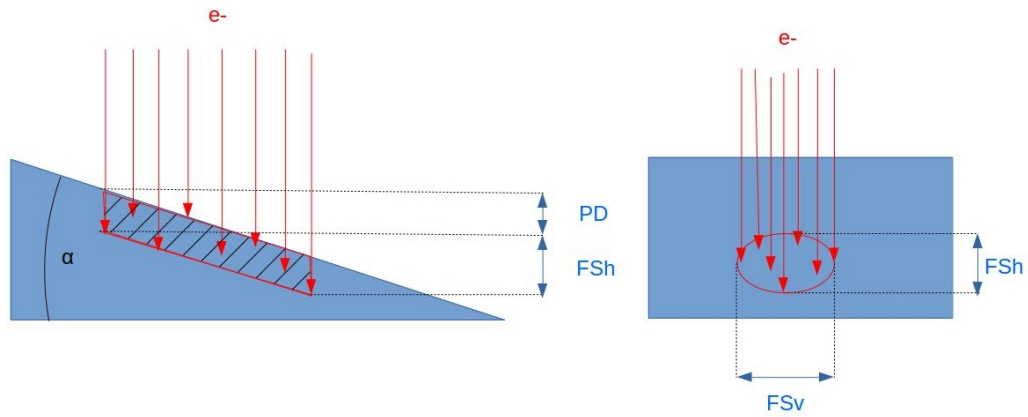


Figure 5.11: Sketch of an elliptical focal spot. Left: anode as seen from the side, FSh is the horizontal size of the focal spot, PD is the penetration depth of the electrons, alpha is the anode angle. Right: anode as seen from front for negligible penetration depths, FSv is the vertical size of the focal spot.

5.4 Results of simulations and discussion

Approximating the experimentally measured profile of the electron focal spot by a set of normal distributions in the R software tool resulted in an excellent fit, suggesting that this set could be used to simulate the focal spot. The fit parameters can be found in tables 5.2 and 5.3. The superposition of normal distributions is plotted against the experimental data in figure 5.12.

Table 5.2: Fit parameters for the simulation of the small focal spot in GATE. Each normal distribution is implemented in GATE as a separate electron beam. Each electron source in GATE, called "Beam i" corresponds to a two dimensional normal distribution of mean value μ_i , standard deviations $\sigma_{ver,i}$ and $\sigma_{hor,i}$ and intensity a_i .

	x [mm]	y [mm]	σ_x [mm]	σ_y [mm]	Intensity
Beam 1	0	-0.250	0.167	0.225	0.392
Beam 2	0	-1.187	0.167	0.268	0.150
Beam 3	0	1.132	0.167	0.300	0.172
Beam 4	0	0.250	0.167	0.174	0.286

Table 5.3: Fit parameters for the simulation of the large focal spot in GATE. Each normal distribution is implemented in GATE as a separate electron beam. Each electron source in GATE, called "Beam i " corresponds to a two dimensional normal distribution of mean value μ_i , standard deviations $\sigma_{ver,i}$ and $\sigma_{hor,i}$ and intensity a_i .

	x [mm]	y [mm]	σ_x [mm]	σ_y [mm]	Intensity
Beam 1	0	-0.778	0.273	0.250	0.271
Beam 2	0	0.778	0.273	0.281	0.329
Beam 3	0	-0.078	0.273	0.465	0.401

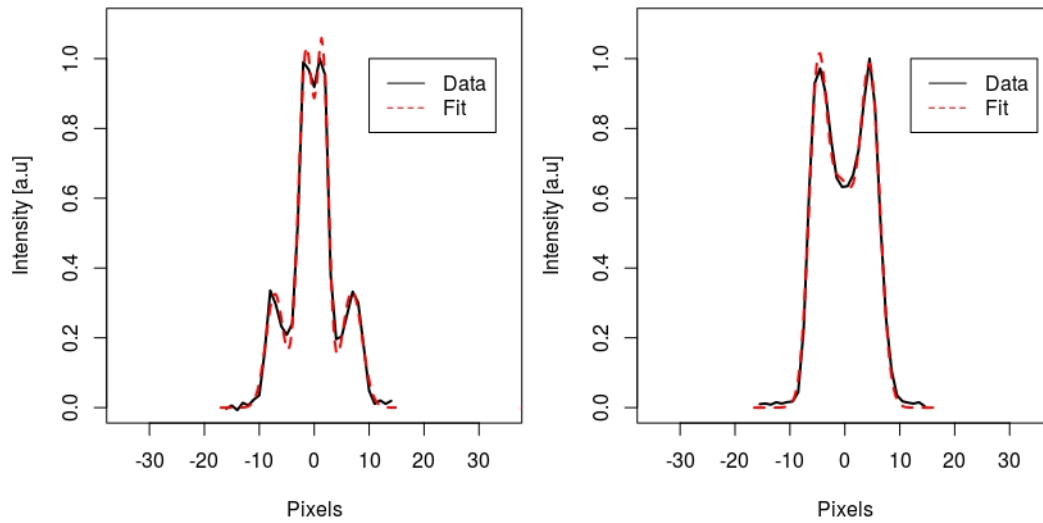


Figure 5.12: Comparison of the experimental data of the focal spot profile in horizontal direction and the superposition of normal distributions in R. Left: small focal spot, Right: large focal spot. This approximation served as a basis for the model of the focal spot in GATE.

Comparisons of simulation and experiment are shown in figures 5.13 and 5.14. For the small focal spot, the absolute value of the relative deviation between simulation and experiment in each data point was on average 6%, for the large focal spot it was 3%. Thus, the simulated focal spot is in good agreement with the experimental data. Furthermore it is not distorted by the penetration depth of the electrons. The penetration depth of electrons in tungsten at the highest energy of 120 keV was evaluated to be $3\mu\text{m}$. The possible distortion caused by this effect is less than 0.3% and thus insignificant compared to the accuracy of the slit-camera experiment.

The quality of the approach could be further improved by increased CPU time to reduce random noise and outliers or by adding additional normal distributions to enhance the goodness of fit.

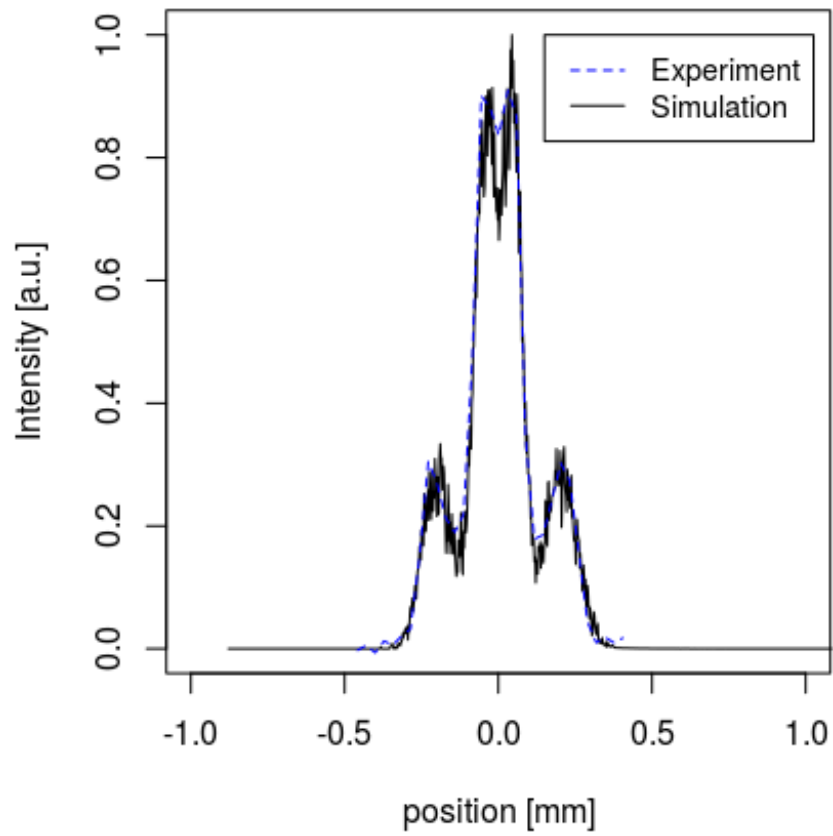


Figure 5.13: Comparison of the profile of the small focal spot in horizontal direction for simulation and experiment.

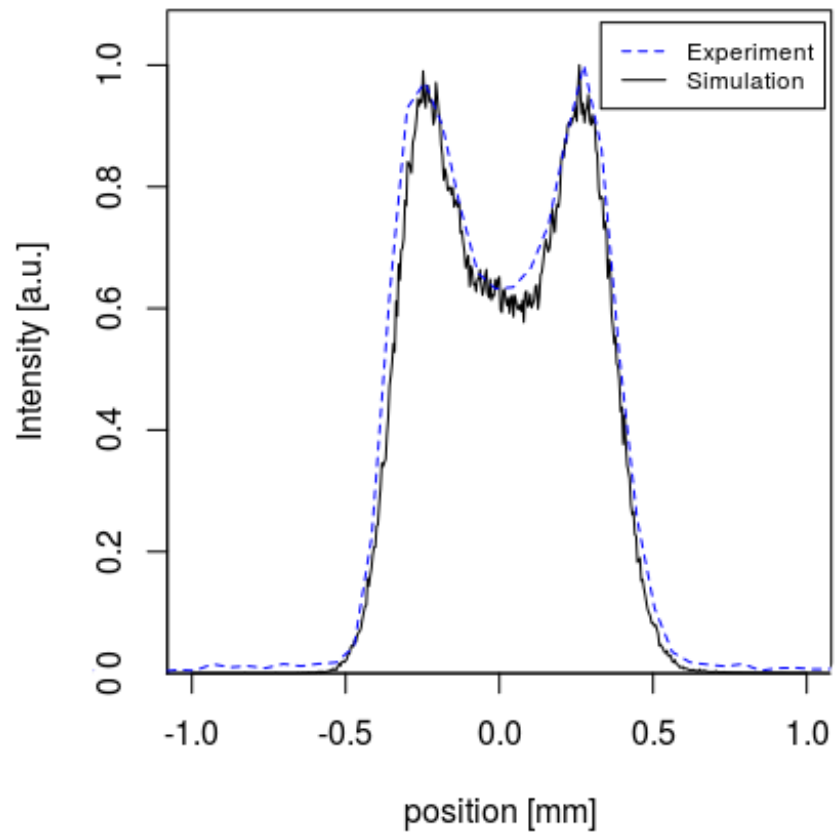


Figure 5.14: Comparison of the profile of the large focal spot in horizontal direction for simulation and experiment.

6. Heel effect

In planar imaging, the heel effect of the anode has a strong and often unwanted impact on image quality. Thus a flattening filter is added to reduce this effect. If scatter effects on the flattening filter are to be simulated, it is essential that the heel effect is accurately represented in the model.

For this reason, the two dimensional dose distribution as well as the dose profile were investigated in both experiment and simulation. In addition to providing information about the heel effect, this also served the purpose of validating the geometry of the X-ray head.

6.1 Experiments

The heel effect of the anode was measured with the Lynx camera. Because the flattening filter of the X-ray head was designed to compensate the heel effect, all filters were removed prior to the measurements.

In the first step, the X-ray head was positioned horizontally and rotated by 5.8° to cancel out the tilt of the source as described in section 2.1. The Lynx camera was then placed on top of the patient couch at a distance of 22.2 cm between the center of the exit window and the Lynx detection plane. The experimental setup is shown in figure 6.1.

The two dimensional dose distribution was measured for tube voltages of 60 keV, 80 keV, 100 keV and 120 kV and tube currents of 20 mA and 40 mA. Each measurement was averaged over several pulses of 10 ms duration.

The entire process was performed for a parallel position of exit window and Lynx detection plane. Because the source is rotated by 3° relative to the exit window to counteract the heel effect, the measurements were repeated with the detection plane perpendicular to the central beam. The first setup better reflects the source-detector setup of the ImagingRing™ System, whereas the second setup shows the heel effect more clearly.

The two dimensional dose distribution was processed in R by evaluating the dose along vertical and horizontal lines. Results were averaged over multiple lines to reduce variance. The resulting graphs allow the evaluation of the heel effect and can be used to validate simulation data.

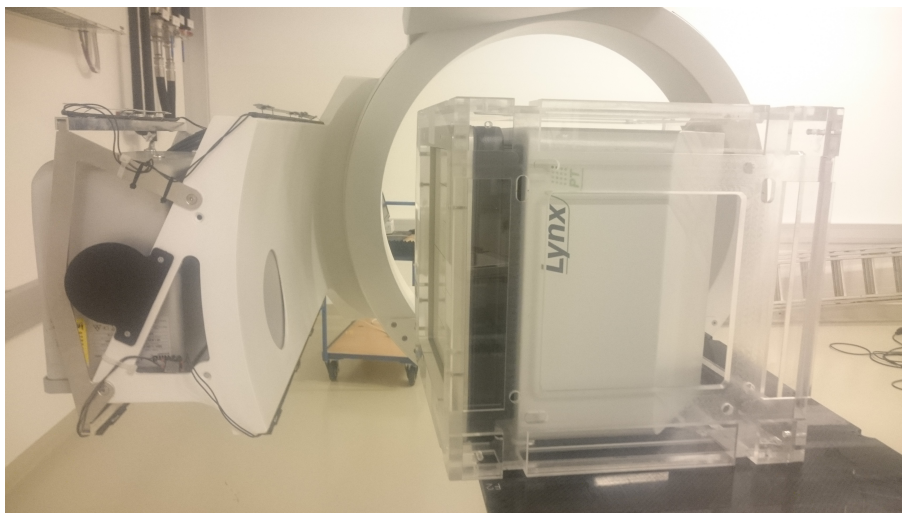


Figure 6.1: Experimental setup of heel measurements. Left: the X-ray head of the ImagingRing™ System, Right: The Lynx camera. The detector (not in the picture) of the ImagingRing™ System was moved to the top in order to protect the electronics from unfiltered radiation.

6.2 Results of experiments

The intensity profile measured by the Lynx camera can be seen in figure 6.2. The heel effect of the anode is shown by the steep decline on the left side. While the absolute intensity depends heavily on the tube voltage, the shape of the curve is mostly identical for all tube voltages with exception of a slight tilt to the right that can be observed for higher tube voltages. This tilt results from the increased electron penetration depth for higher tube voltages. The deeper the electrons interact in the anode, the longer the way the photons have to travel through the anode [8].

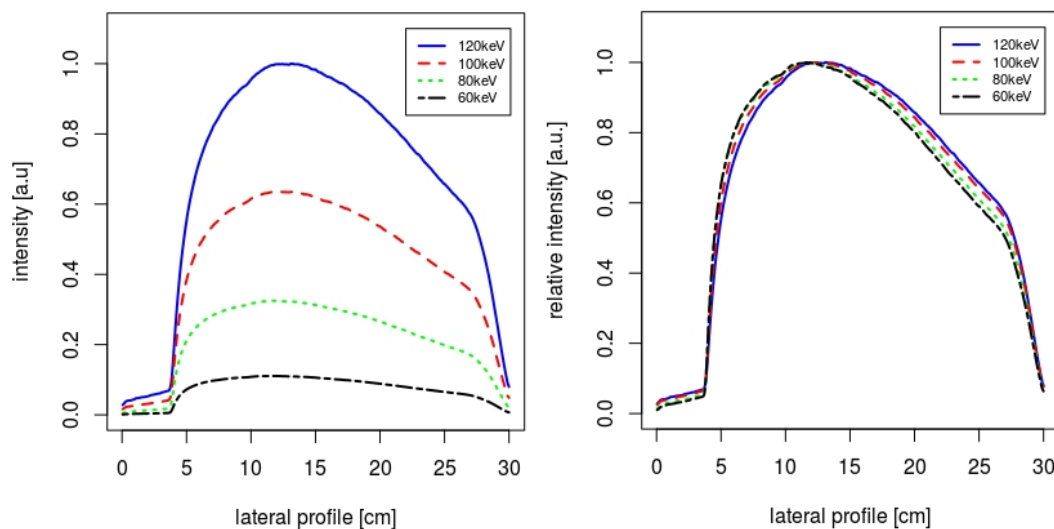


Figure 6.2: Intensity profile of the X-ray source of the ImagingRing™ System without primary collimator, flattening filter and collimator jaws as detected by the Lynx camera. Left: absolute intensity, right: intensity relative to maximum

6.3 Simulations

The heel effect of the anode was evaluated by recreating the Lynx experiment in GATE.

A detection plane was placed perpendicular to the central photon beam at a distance of 23.1 cm from the exit window as illustrated in figure 6.3. The deposited energy was then registered by a dose actor.

The size of the detector was increased to 60 cm x 60 cm which was 4 times the size of the Lynx to provide additional information. However, for direct comparison between experiment and simulation a smaller excerpt the size of the physical Lynx camera could be extracted from the data.

The two dimensional dose distribution was processed in R evaluating the dose along vertical and horizontal lines. Results were averaged over multiple line profiles to reduce variance. The resulting graphs allow the evaluation of the heel effect and can be compared to the experimental data for validation.

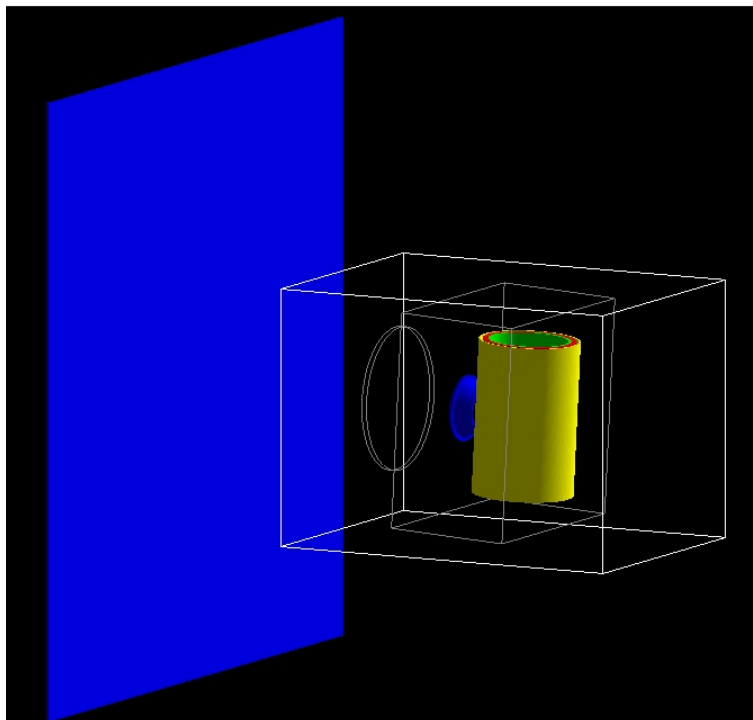


Figure 6.3: Simulation of Heel measurements. Left: The detection plane of the Lynx camera (blue), Right: the X-ray head of the ImagingRing™ System.

6.4 Results of simulations and discussion

A comparison of the 2D intensity distribution of experiment and simulation can be seen in figure 6.4. The excellent agreement suggests that the X-ray head was modeled correctly. The difference in lightness results from the lower statistical certainty in the simulation and can be reduced by increasing the number of simulated particles.

The intensity profile in horizontal direction for a monoenergetic beam of 120 keV can be seen in figure 6.5. The heel effect is clearly visible on the left side and there is an excellent match of simulation and experiment. The maximum relative deviation between simulation and experiment was 5.7%.

The intensity profile for an electron energy spectrum that resulted from the optimization in chapter 4.3.2 can be seen in figure 6.6. The maximum relative deviation between simulation and experiment was 10%. While there is still a reasonable fit, the simulated profile is slightly tilted to the left. When compared to the results from figure 6.2 this suggests that the X-ray energy in the simulation was lower than in the experiment. This results from an overrepresentation of lower electron energies caused by the energy weighting approach.

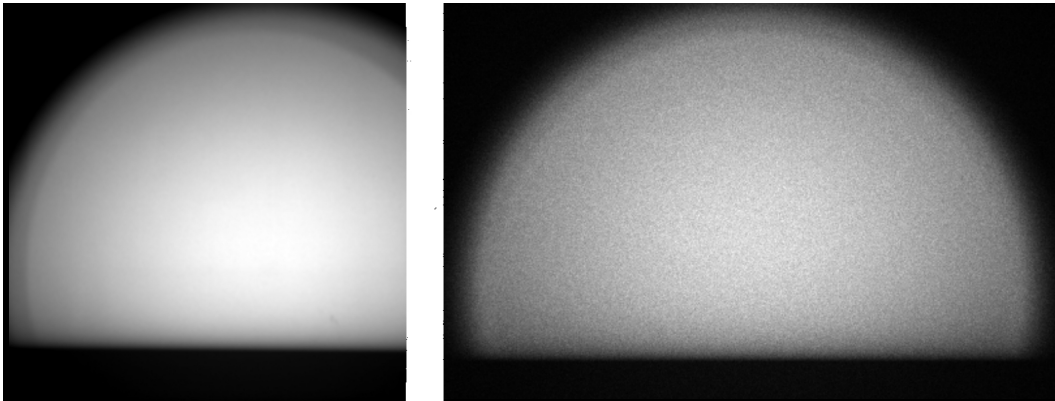


Figure 6.4: Greyscale plot of the 2D intensity distribution of the X-ray source of the ImagingRing™ System without primary collimator, flattening filter and collimator jaws. Left: 2D intensity measured with Lynx. The image is cut off due to the limited size of the Lynx scan field. Right: simulated 2D intensity

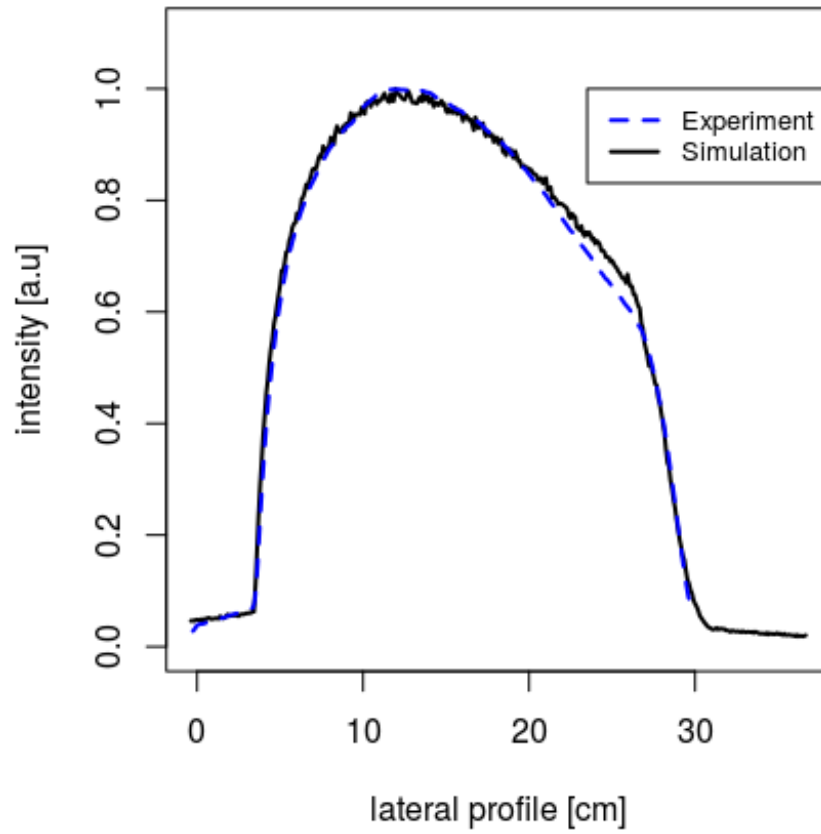


Figure 6.5: Comparison of the heel effect in vertical direction for simulation and experiment for a monochromatic electron beam of 120 keV. Due to the limited size of the Lynx scan field, the experimental data is cut off to the right.

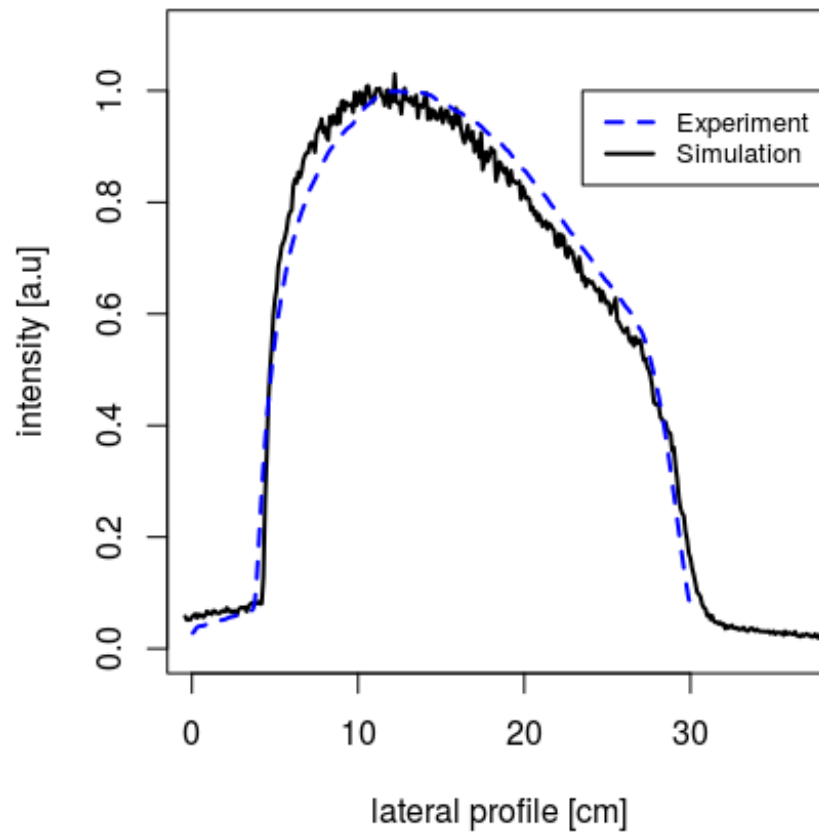


Figure 6.6: Comparison of the heel effect in vertical direction for simulation and experiment for an electron energy spectrum that resulted from the optimization in chapter 4.3.2. Due to the limited size of the Lynx scan field, the experimental data is cut off to the right.

7. Summary

In this thesis, a Monte Carlo based model of the ImagingRing™ System was established and validated.

In a first step, the Monobloc X-ray tube of the ImagingRing™ System was modeled. A simple approach of using a precalculated spectrum from SpekCalc proved to be unsuitable as it resulted in an unrealistic homogeneous 2D intensity distribution. It did not show important effects such as the heel effect of the anode.

The second approach was to model the X-ray tube directly in GATE, by modeling a monoenergetic electron beam and a tungsten anode. Combined with the surrounding geometry, this approach showed the expected 2D intensity distribution. Simulating large numbers of electrons requires extensive amounts of computing power. Consequently efficiency was investigated and improved by applying the splitting method.

The X-ray head, consisting of flattening filter, primary collimator, collimator jaws and exit window, modeled in a CAD software, was imported in GATE.

In a second step, the Monte Carlo model was evaluated against experimental data. Half value layer (HVL) in aluminum were measured with different added filters using the NOMEX multimeter. This was done for several tube voltage and tube current settings as well as with and without flattening filter, primary collimator and collimator jaws.

The experimental setup was then recreated in the simulation. The resulting HVL in aluminum showed deviations of up to 28% between experiment and simulation. To improve the model, the effect of electron backscatter at the anode was modeled indirectly by choosing an energy weighting approach. In this approach, the electron energy was approximated by an energy spectrum instead of a single energy. The spectrum was then optimized to fit the experimentally measured HVL in aluminum by the use of a quasi-Newton BFGS method and simulated annealing. The resulting HVL in aluminum agreed on average within 4% of the experimental data.

Next, the electron focal spot was investigated. The focal spot of the ImagingRing™ System was measured using a dedicated slit camera. Its profile in vertical and

horizontal direction was then approximated in the simulation by the superposition of several normal distributions. The resulting focal spot was in good agreement with experimental data, with average deviations of 3 to 6%.

In a final step, the two-dimensional intensity distribution of the X-ray source was investigated. It was experimentally measured using the Lynx camera. Because flattening filter and collimators were designed to homogenize and limit the X-ray field, they were removed prior to the measurements.

The intensity distribution was then evaluated in the simulation. The setup, including relevant parts of the Lynx camera, was modeled in GATE, effectively recreating the experiment in the simulation. The intensity profiles resulting from the simulation matched the experimentally measured profiles. In both experiment and simulation the heel effect of the anode was clearly visible.

In conclusion, the energy spectrum, focal spot size and shape and 2D intensity distribution of the established model were in good agreement with the experiment.

The established model can be compared to publications from other authors.

A very similar approach to modeling a CT device was described by Emiliano Spezi et al. [58]. In their work, the EGSNRC/BEAMNRC Monte Carlo code was used to directly model an X-ray tube. Anode geometry, anode material, density and filtration were taken into account. A parallel rectangular electron source was simulated and the vendor supplied geometry of the electron focal spot was included in the model. Subsequent filters were modeled according to vendor supplied data. The results from the X-ray tube simulation were stored in a phase space. The resulting phase space could then be used for CT simulations without the need to repeat the tube simulation, making the simulation more time efficient. The results were benchmarked against measurements in water and half value layer measurements and showed excellent agreement. The chosen method of storing the X-ray distribution in a phase actor could be applied to the model of the ImagingRing™ System as well. This would result in shorter simulation times at the cost of flexibility in tuning the tube voltage.

Watson et al. described the Monte Carlo modeling of an X-ray source (INTRA-BEAM, Carl Zeiss) using the EGSnrc Monte Carlo code [65]. In their work, the photon fluence spectra emitted by the source were detected in a circular region around the source. From the spectra, half value layer were calculated and compared to experimental data, resulting in good agreement.

Källman et al. used the RayStation (RayStation™, RaySearch Laboratories, Stockholm, Sweden) treatment planning system to calculate the dose from a CT device (GE Healthcare, Wauwatosa, WI, USA), using a precalculated spectrum approach [32]. The X-ray beam was characterized by measurements of half value layers in aluminum and KERMA distributions. The X-ray spectrum was then calculated us-

ing SpekCalc. It was modified using four different beam-shaping variations such as adding angle dependent aluminum filtration. The resulting X-ray beam was verified by comparison with measurements in water and in an anthropomorphic phantom.

Turner et al. describe a systematic approach on reconstructing an X-ray energy spectrum from half value layer measurements [61]. The energy spectrum was first numerically constructed from the measured half value layers. It was then modified by a filtration scheme of equivalent filters to attenuate the beam in a similar fashion as the actual filtration of the actual device as measured by bowtie profile measurements.

In the works published by Jarry et al. a CT device was simulated using the MCNP4B Monte Carlo code [13, 31]. The X-ray energy spectrum was in the first case calculated and in the second case supplied by the CT manufacturer. Filtration was accounted for by application of weighting factors to the source. The path length of X-ray photons was calculated for all directions and implemented as a look up table. The resulting angle dependent filter attenuation was then assigned to each X-ray photon as a weight factor.

In comparison, the direct way of modeling the X-ray tube by simulating an electron beam was only chosen by Emiliano Spezi et al., while most other models started by calculating a spectrum and afterwards adapting it to fit the two dimensional dose distribution. Both models resulted in excellent agreement with experimental data. The precalculated spectrum approach chosen by Turner, Watson, Källman and Jarry is especially advantageous if little information about the X-ray tube geometry is available. Furthermore, it requires much less CPU time. However, this comes at the cost of flexibility. Directly modeled X-ray tubes allow modifications in focal spot shape and size. Thus they can be used to investigate effects such as the extra focal radiation.

8. Conclusion and outlook

The established model reflects all key attributes of the physical ImagingRing™ System and provides information that would not be accessible otherwise.

Furthermore, the systematic approach to modeling an X-ray source described in this thesis can be applied to other X-ray devices. This work can be used as a step-by-step guide in order to establish a detailed model that accurately reflects the physical device.

To further improve the model, electron backscatter could be modeled directly by adding an electric field. As electric fields are not available in GATE, they would have to be added to the source code manually. However, extensive testing would be required to ensure the electric fields work as intended. In the current model, this effect is compensated by the energy weighting approach.

The model can also be extended to allow full CT scan simulations. This would require a rotating source as well as a rotating detector. It can be done by simulating a sequence of X-ray images with different source and detector positions.

Further research will include the application of the established model to investigate the head scatter of the ImagingRing™ System. CT scans of phantoms will be compared to simulations in order to assess scatter effects. The findings can then be used to improve image processing [46]. As a result, the X-ray dose to patients could possibly be reduced, supporting the ALARA (As Low As Reasonably Achievable) principle [3, 14].

Bibliography

- [1] Nomex multimeter commercial note, March 2018. URL file:///home/nik/Desktop/NOMEX_Multimeter_Note_en_90919901_00.pdf.
- [2] A. Ableitinger, A. Utz, A. Zechner, S. Vatnitsky, and M. Stock. EP-1741: Commissioning of a robotic patient positioning system equipped with an integrated tracking system. *Radiotherapy and Oncology*, 123:S958, may 2017. doi: 10.1016/s0167-8140(17)32104-7.
- [3] P. Alaei and E. Spezi. Imaging dose from cone beam computed tomography in radiation therapy. *Physica Medica*, 31(7):647–658, nov 2015. doi: 10.1016/j.ejmp.2015.06.003.
- [4] A. F. Bielajew. *Fundamentals of the Monte Carlo method for neutral and charged particle transport*. Ann Arbor, Michigan, U.S.A.: University of Michigan, 2001.
- [5] H. Braun, Y. Kyriakou, M. Kachelrieß, and W. A. Kalender. The influence of the heel effect in cone-beam computed tomography: artifacts in standard and novel geometries and their correction. *Physics in Medicine & Biology*, 55(19): 6005, 2010. URL <http://stacks.iop.org/0031-9155/55/i=19/a=024>.
- [6] R. H. Byrd, P. Lu, J. Nocedal, and C. Zhu. A Limited Memory Algorithm for Bound Constrained Optimization. *SIAM Journal on Scientific Computing*, 16(5):1190–1208, 1995. doi: 10.1137/0916069.
- [7] J. M. Chambers, W. S. Cleveland, B. Kleiner, and P. A. Tukey. *Graphical Methods for Data Analysis*. Wadsworth, 1983.
- [8] P. Cherry. *[(Practical Radiotherapy: Physics and Equipment)]*. Wiley-Blackwell (an imprint of John Wiley & Sons Ltd), 2009. ISBN 1405184264.
- [9] I. E. Commission. Medical electrical equipment - dosimetric instruments used for the non-invasive measurement of x-ray tube voltage in diagnostic radiology, 2002.

-
- [10] I. E. Commission. Medical diagnostic x-ray equipment - radiation conditions for use in the determination of characteristics, 2005.
- [11] I. E. Commission. Medical electrical equipment - dosimeters with ionization chambers and/or semiconductor detectors as used in x-ray diagnostic imaging, 2012.
- [12] E. H. Darlington. Backscattering of 10-100 keV electrons from thick targets. *Journal of Physics D: Applied Physics*, 8(1):85, 1975. URL <http://stacks.iop.org/0022-3727/8/i=1/a=016>.
- [13] J. J. DeMarco, C. H. Cagnon, D. D. Cody, D. M. Stevens, C. H. McCollough, J. O'Daniel, and M. F. McNitt-Gray. A monte carlo based method to estimate radiation dose from multidetector CT (MDCT): cylindrical and anthropomorphic phantoms. *Physics in Medicine and Biology*, 50(17):3989–4004, aug 2005. doi: 10.1088/0031-9155/50/17/005.
- [14] G. X. Ding, P. Munro, J. Pawlowski, A. Malcolm, and C. W. Coffey. Reducing radiation exposure to patients from kV-CBCT imaging. *Radiotherapy and Oncology*, 97(3):585–592, dec 2010. doi: 10.1016/j.radonc.2010.08.005.
- [15] I. Dosimetry. Lynx PT, February 2018. URL <http://www.iba-dosimetry.com/solutions/radiation-therapy/particle-therapy-qa/lynx-pt/>.
- [16] S. A. et al. Geant4—a simulation toolkit. *Nuclear Instruments and Methods in Physics Research Section A: Accelerators, Spectrometers, Detectors and Associated Equipment*, 506(3):250–303, jul 2003. doi: 10.1016/s0168-9002(03)01368-8.
- [17] S. J. et al. GATE: a simulation toolkit for PET and SPECT. *Physics in Medicine and Biology*, 49(19):4543–4561, sep 2004. doi: 10.1088/0031-9155/49/19/007.
- [18] T. R. Fewell. Handbook of computed tomography x-ray spectra, 1981.
- [19] H. Fuchs, J. Ströbele, T. Schreiner, A. Hirtl, and D. Georg. A pencil beam algorithm for helium ion beam therapy. *Medical Physics*, 39(11):6726–6737, oct 2012. doi: 10.1118/1.4757578.
- [20] H. Fuchs, P. Moser, M. Gröschl, and D. Georg. Magnetic field effects on particle beams and their implications for dose calculation in MR-guided particle therapy. *Medical Physics*, 44(3):1149–1156, feb 2017. doi: 10.1002/mp.12105.
- [21] H. Furtado, E. Steiner, M. Stock, D. Georg, and W. Birkfellner. Real-time 2d/3d registration using kV-MV image pairs for tumor motion tracking in image guided radiotherapy. *Acta Oncologica*, 52(7):1464–1471, jul 2013. doi: 10.3109/0284186x.2013.814152.
- [22] *Geant4 User's Guide for Application Developers*. Geant4 Collaboration, 2016.

- [23] D. Georg. Bildgeführte Radiotherapie, Lecture, 2016.
- [24] P. Georg, P. Andrzejewski, K. Pinker, and D. Georg. Strahlentherapieplanung mit der funktionellen MRT. *Der Radiologe*, 55(12):1097–1103, oct 2015. doi: 10.1007/s00117-015-0036-z.
- [25] R. L. Harrison, C. Granja, and C. Leroy. Introduction to monte carlo simulation. AIP, 2010. doi: 10.1063/1.3295638.
- [26] L. Hoffmann, M. Alber, M. F. Jensen, M. I. Holt, and D. S. Møller. Adaptation is mandatory for intensity modulated proton therapy of advanced lung cancer to ensure target coverage. *Radiotherapy and Oncology*, 122(3):400–405, mar 2017. doi: 10.1016/j.radonc.2016.12.018.
- [27] *Tube Documentation X20P 0.3/0.6*. iae, Milano, Italy, 1998.
- [28] *LYNX PT User Manual*. IBA Dosimetry, Bartlett, USA, June 2014.
- [29] *Technical Drawing X20P Monobloc*. imd, Grassobbio, Italy, 2014.
- [30] P. Jaeckel. *Monte Carlo Methods in Finance*. Wiley, 2002. ISBN 047149741X.
- [31] G. Jarry, J. J. DeMarco, U. Beifuss, C. H. Cagnon, and M. F. McNitt-Gray. A monte carlo-based method to estimate radiation dose from spiral ct: from phantom testing to patient-specific models. *Physics in Medicine & Biology*, 48(16):2645, 2003. URL <http://stacks.iop.org/0031-9155/48/i=16/a=306>.
- [32] H.-E. Källman, R. Holmberg, J. Andersson, L. Kull, E. Tranéus, and A. Ahnesjö. Source modeling for monte carlo dose calculation of CT examinations with a radiotherapy treatment planning system. *Medical Physics*, 43(11):6118–6128, oct 2016. doi: 10.1118/1.4965043.
- [33] P. Keuschnigg, D. Kellner, K. Fritscher, A. Zechner, U. Mayer, P. Huber, F. Sedlmayer, H. Deutschmann, and P. Steininger. Nine-degrees-of-freedom flexmap for a cone-beam computed tomography imaging device with independently movable source and detector. *Medical Physics*, 44(1):132–142, jan 2017. doi: 10.1002/mp.12033.
- [34] S. H. Kim, M. G. Pia, T. Basaglia, M. C. Han, G. Hoff, C. H. Kim, and P. Saracco. Validation test of geant4 simulation of electron backscattering. *IEEE Transactions on Nuclear Science*, 62(2):451–479, apr 2015. doi: 10.1109/tns.2015.2401055.
- [35] H. Krieger. *Grundlagen der Strahlungsphysik und des Strahlenschutzes*. Vieweg Teubner Verlag, 2012. doi: 10.1007/978-3-8348-2238-3.
- [36] H. Krieger. *Strahlungsquellen für Technik und Medizin*. Springer Fachmedien Wiesbaden, 2013. doi: 10.1007/978-3-658-00590-0.

- [37] H. Krieger. *Strahlungsmessung und Dosimetrie*. Springer Fachmedien Wiesbaden, 2013. doi: 10.1007/978-3-658-00386-9.
- [38] B. F. Manly. *Randomization, Bootstrap and Monte Carlo Methods in Biology, Third Edition (Texts in Statistical Science Series)*. Chapman and Hall/CRC, 2006. ISBN 1584885416.
- [39] *Quarterly Quality Assurance Guideline*. MedAustron, Wiener Neustadt, Austria, 2017.
- [40] MedAustron. Particle Accelerator, January 2018. URL <https://www.medaustron.at/en/particle-accelerator>.
- [41] *ImagingRing Benutzerhandbuch IR Version 1.1*. medPhoton, Salzburg, Austria, 2015.
- [42] *ImagingRing Geometry Specifications Interface Control Document*. medPhoton, Salzburg, Austria, 2015.
- [43] medPhoton. ImagingRing System, December 2017. URL <https://www.medphoton.at/products/imaging-ring/>.
- [44] V. I. Mikla and V. V. Mikla. *Medical Imaging Technology*. Elsevier, 2013.
- [45] M. Moteabbed, J. Schuemann, and H. Paganetti. Dosimetric feasibility of real-time MRI-guided proton therapy. *Medical Physics*, 41(11):111713, oct 2014. doi: 10.1118/1.4897570.
- [46] G. Poludniowski, P. M. Evans, V. N. Hansen, and S. Webb. An efficient Monte Carlo-based algorithm for scatter correction in keV cone-beam CT. *Physics in Medicine & Biology*, 54(12):3847, 2009.
- [47] G. Poludniowski, G. Landry, F. DeBlois, P. M. Evans, and F. Verhaegen. SpekCalc: a program to calculate photon spectra from tungsten anode X-ray tubes. *Physics in Medicine and Biology*, 54(19):N433–N438, sep 2009. doi: 10.1088/0031-9155/54/19/n01.
- [48] G. G. Poludniowski. Calculation of X-ray spectra emerging from an X-ray tube. Part II. X-ray production and filtration in X-ray targets. *Medical Physics*, 34(6Part1):2175–2186, may 2007. doi: 10.1118/1.2734726.
- [49] G. G. Poludniowski and P. M. Evans. Calculation of X-ray spectra emerging from an X-ray tube. Part I. Electron penetration characteristics in X-ray targets. *Medical Physics*, 34(6Part1):2164–2174, may 2007. doi: 10.1118/1.2734725.
- [50] *NOMEX Multimeter T11049 Gebrauchsanweisung*. PTW, Freiburg, Germany, 2014.

- [51] N. Reisz. Monte Carlo modelling of the X-ray spectrum and distribution of a commercial X-ray source, 2017. Project thesis.
- [52] J. Riegel, W. Mayer, and Y. van Havre. Freecad, 2002. URL <https://freecadweb.org/>.
- [53] S. Rit, R. Clackdoyle, P. Keuschnigg, and P. Steininger. Filtered-backprojection reconstruction for a cone-beam computed tomography scanner with independent source and detector rotations. *Medical Physics*, 43(5):2344–2352, apr 2016. doi: 10.1118/1.4945418.
- [54] S. Russo, D. Boi, A. Mirandola, S. Molinelli, A. Mairani, E. Mastella, G. Magro, S. Giordanengo, and M. Ciocca. Dosimetric characterization of a commercial 2-d scintillation detector for quality assurance tests in scanned proton and carbon ion beams. *Physica Medica*, 32:199, sep 2016. doi: 10.1016/j.ejmp.2016.07.675.
- [55] Y. Seppenwoolde, M. Stock, M. Buschmann, D. Georg, K.-Y. Bauer-Novotny, R. Pötter, and P. Georg. Impact of organ shape variations on margin concepts for cervix cancer ART. *Radiotherapy and Oncology*, 120(3):526–531, sep 2016. doi: 10.1016/j.radonc.2016.08.004.
- [56] H. Shirato, S. Shimizu, T. Kunieda, K. Kitamura, M. van Herk, K. Kagei, T. Nishioka, S. Hashimoto, K. Fujita, H. Aoyama, K. Tsuchiya, K. Kudo, and K. Miyasaka. Physical aspects of a real-time tumor-tracking system for gated radiotherapy. *International Journal of Radiation Oncology Biology Physics*, 48(4):1187–1195, nov 2000. doi: 10.1016/s0360-3016(00)00748-3.
- [57] C. Siversson, F. Nordström, T. Nilsson, T. Nyholm, J. Jonsson, A. Gunnlaugsson, and L. E. Olsson. Technical note: MRI only prostate radiotherapy planning using the statistical decomposition algorithm. *Medical Physics*, 42(10):6090–6097, sep 2015. doi: 10.1118/1.4931417.
- [58] E. Spezi, P. Downes, E. Radu, and R. Jarvis. Monte carlo simulation of an x-ray volume imaging cone beam CT unit. *Medical Physics*, 36(1):127–136, dec 2008. doi: 10.1118/1.3031113.
- [59] E. Steiner, M. Stock, B. Kostresevic, A. Ableitinger, U. Jelen, H. Prokesch, A. Santiago, P. Trnková, A. Wolf, A. Wittig, A. Lomax, O. Jäkel, G. Baroni, and D. Georg. Imaging dose assessment for IGRT in particle beam therapy. *Radiotherapy and Oncology*, 109(3):409–413, dec 2013. doi: 10.1016/j.radonc.2013.09.007.
- [60] M. Stock, D. Georg, A. Ableitinger, A. Zechner, A. Utz, M. Mumot, G. Kragl, J. Hopfgartner, J. Gora, T. Böhlen, L. Grevillot, P. Kuess, P. Steininger, H. Deutschmann, and S. Vatnitsky. The technological basis for adaptive ion beam therapy at MedAustron: Status and outlook. *Zeitschrift für Medizinische Physik*, oct 2017. doi: 10.1016/j.zemedi.2017.09.007.

- [61] A. C. Turner, D. Zhang, H. J. Kim, J. J. DeMarco, C. H. Cagnon, E. Angel, D. D. Cody, D. M. Stevens, A. N. Primak, C. H. McCollough, and M. F. McNitt-Gray. A method to generate equivalent energy spectra and filtration models based on measurement for multidetector CT monte carlo dosimetry simulations. *Medical Physics*, 36(6Part1):2154–2164, may 2009. doi: 10.1118/1.3117683.
- [62] A. Utz, A. Ableitinger, A. Zechner, M. Mumot, M. Teichmeister, P. Steininger, H. Deutschmann, and M. Stock. OC-0491: Quality assurance of a novel table mounted imaging device integrated in a patient positioning system. *Radiotherapy and Oncology*, 123:S261–S262, may 2017. doi: 10.1016/s0167-8140(17)30931-3.
- [63] D. M. S. W. N. Venables and the R Core Team. *An Introduction to R*, 2017. Notes on R: A Programming Environment for Data Analysis and Graphics.
- [64] P. Wang, L. Yin, Y. Zhang, M. Kirk, G. Song, P. H. Ahn, A. Lin, J. Gee, D. Dolney, T. D. Solberg, R. Maughan, J. McDonough, and B.-K. K. Teo. Quantitative assessment of anatomical change using a virtual proton depth radiograph for adaptive head and neck proton therapy. *Journal of Applied Clinical Medical Physics*, 17(2):427–440, mar 2016. doi: 10.1120/jacmp.v17i2.5819.
- [65] P. Watson, M. Popovic, and J. Seuntjens. An in-air monte carlo investigation of a miniature low energy x-ray tube. *Radiotherapy and Oncology*, 2015.
- [66] J. F. Williamson. Monte carlo evaluation of kerma at a point for photon transport problems. *Medical Physics*, 14(4):567–576, jul 1987. doi: 10.1118/1.596069.
- [67] Y. Yuan, O. C. Andronesi, T. R. Bortfeld, C. Richter, R. Wolf, A. R. Guimaraes, T. S. Hong, and J. Seco. Feasibility study of in vivo MRI based dosimetric verification of proton end-of-range for liver cancer patients. *Radiotherapy and Oncology*, 106(3):378–382, mar 2013. doi: 10.1016/j.radonc.2013.01.016.
- [68] A. Zechner, M. Stock, D. Kellner, I. Ziegler, P. Keuschnigg, P. Huber, U. Mayer, F. Sedlmayer, H. Deutschmann, and P. Steininger. Development and first use of a novel cylindrical ball bearing phantom for 9-DOF geometric calibrations of flat panel imaging devices used in image-guided ion beam therapy. *Physics in Medicine and Biology*, 61(22):N592–N605, oct 2016. doi: 10.1088/0031-9155/61/22/n592.

A. Appendix

Table A.1: HVL_{Al} and computing time for varying step sizes inside the anode volume. All HVL_{Al} and computing times are relative to a reference value at a step size of 0.005 mm.

Step size [mm]	$HVL_{Al}/HVL_{Al,ref}$ [a.u.]	computing time [a.u.]
0.005	1	1
0.001	1.02	1
0.0005	1.02	2
0.0001	1.03	4

Table A.2: HVL_{Al} and computing time for varying cut sizes inside the anode volume. All HVL_{Al} and computing times are relative to a reference value at a cut size of 0.005 mm.

Cut size [mm]	$HVL_{Al}/HVL_{Al,ref}$ [a.u.]	computing time [a.u.]
0.005	1	1
0.001	0.90	10
0.0005	0.90	30
0.0001	0.90	500

Table A.3: HVL_{Al} and computing time for varying cut sizes inside the anode volume. All HVL_{Al} and computing times are relative to a reference value at a cut size of 0.005 mm.

Cut and step size [mm]	$HVL_{Al}/HVL_{Al,ref}$ [a.u.]	computing time [a.u.]
0.005	1	1
0.001	0.93	10
0.0005	0.94	30
0.0001	0.94	500

Table A.4: Efficiency of different splitting factors

Splitting factor	photons per second	efficiency
1	62.4	1
100	5962	96
1000	11714	188
10000	12401	199

B. Code Listing

```
#####  
# main.mac  
#####  
  
# ===== CONTROL =====  
  
# contains settings for particle number, splitting,  
# physics list, etc.  
  
/control/execute mac/control.mac  
  
# ===== MATERIALS =====  
  
/gate/geometry/setMaterialDatabase data/GateMaterials.db  
  
# ===== GEOMETRY =====  
  
/control/execute mac/geometry.mac  
  
# ===== PHYSICS =====  
  
/gate/physics/addPhysicsList {physlist}  
  
# ===== PARAMETERS =====
```

```
/control/execute mac/parameters.mac

# ===== OUTPUTS =====

# use allowNoOutput if you dont have
# any actors (for checking the geometry)
# /gate/output/allowNoOutput

/control/execute mac/actors.mac

# ===== SOURCE =====

/gate/run/initialize
/control/execute mac/source.mac

# ===== INITIALIZATION =====

/gate/run/initialize

# ===== SPLITTING =====

# activates splitting in the anode volume
/process/em/setSecBiasing eBrem anode {nsplitting} 100 MeV
/process/em/setSecBiasing eIoni anode {nsplitting} 100 MeV

# ===== SEED =====

/gate/random/setEngineName MersenneTwister
/gate/random/setEngineSeed auto

# ===== START BEAMS =====

/gate/application/setTotalNumberOfPrimaries {pnum}
/gate/application/start
```

```
=====  
# control.mac  
=====
```

Variables used in other files are defined here

```
=====  
#=====  
# set the number of primary particles here  
  
/control/alias pnum "10"
```

```
=====  
#=====  
# turn on/off visualization  
  
/control/execute mac/visu.mac  
/vis/scene/add/axes  
#~ /vis/disable
```

```
=====  
#=====  
# set the splitting factor here  
  
/control/alias nsplitting "1000"
```

```
=====  
#=====  
# set the physics list here  
# Some other possible options: "QBBC_EMZ", "emlivermore",  
# "QGSP_BERT_EMZ", "emlowenergy"  
  
/control/alias physlist "empenelope"
```

```
=====  
#=====  
  
/control/alias CubeSize "30"    #[mm]
```

```
/control/alias DetectorMaterial "Aluminium"      #Aluminium Copper
/control/alias zlength "20"      #[mm] detector length
/control/alias halfzlength "10"  #[mm]
/control/alias Resol "0.1"      #[mm] detector resolution
```

```
##### LYNX DETECTOR #####
```

```
/control/alias LynxMaterial "Aluminium"
/control/alias LynxSize "600"    #[mm]
/control/alias LynxLength "3"   #[mm] set detector length
```

```
##### CUT & STEP #####
```

```
#Cut and step size settings for detector, anode and filter
```

```
/control/alias detector_step "0.01"
/control/alias detector_cut "0.01"
```

```
/control/alias anode_step "0.001"      #step size
/control/alias anode_cut "0.001"      #production cut
/control/alias anode_trackcut "0.001"  #track cut
```

```
/control/alias filter_step "0.001"
/control/alias filter_cut "0.001"
/control/alias filter_trackcut "0.001"
```

```
/control/alias world_step "1"
/control/alias world_cut "1"
```

```
##### ANODE MATERIAL #####
```

```
#set anode material here
```

```
/control/alias anodemat "Tungsten"      Tungsten
```

```
#####
# geometry.mac
#####
```

```
# WORLD
```

```
/gate/world/geometry/setXLength 140. cm
/gate/world/geometry/setYLength 140. cm
/gate/world/geometry/setZLength 200. cm
/gate/world/setMaterial Air

#===== X-Ray Head =====

# X-Ray head

/gate/world/daughters/name xrhead
/gate/world/daughters/insert box
/gate/xrhead/geometry/setXLength 25 cm
/gate/xrhead/geometry/setYLength 25 cm
/gate/xrhead/geometry/setZLength 35 cm
/gate/xrhead/setMaterial Air

# Polycarbonate Exit window

/gate/xrhead/daughters/name exitwindow
/gate/xrhead/daughters/insert cylinder
# translate in y1 so carprim is in the center
/gate/exitwindow/placement/setTranslation 0.0 5.97 -114.1 mm
/gate/exitwindow/setMaterial PC
/gate/exitwindow/geometry/setRmin 0 mm
/gate/exitwindow/geometry/setRmax 69.16 mm
/gate/exitwindow/geometry/setHeight 0.5 mm

# Jaws
# use comments to change between jaw position 1 and 2

/gate/xrhead/daughters/name Jaws
/gate/xrhead/daughters/insert tessellated
/gate/Jaws/placement/setTranslation 459.13 34.49 11.32 mm
#~ /gate/Jaws/geometry/setPathToSTLFile data/jaws1.stl
/gate/Jaws/geometry/setPathToSTLFile data/jaws2.stl
/gate/Jaws/setMaterial Lead
/gate/Jaws/vis/forceSolid
```

=====*MONOBLOC*=====

Monobloc

```
/gate/xrhead/daughters/name monobloc
/gate/xrhead/daughters/insert box
/gate/monobloc/geometry/setXLength 21 cm
/gate/monobloc/geometry/setYLength 21 cm
/gate/monobloc/geometry/setZLength 15 cm
/gate/monobloc/placement/setRotationAxis 1 0 0
/gate/monobloc/placement/setRotationAngle 3 deg
/gate/monobloc/setMaterial Vacuum
```

ANODE

```
/gate/monobloc/daughters/name anode
/gate/monobloc/daughters/insert cone
/gate/anode/setMaterial {anodemat}
/gate/anode/geometry/setRmin1 0 mm
/gate/anode/geometry/setRmax1 19.93 mm
/gate/anode/geometry/setRmin2 0 mm
/gate/anode/geometry/setRmax2 32.0 mm
# 32 mm from Tube.pdf diameter=64 mm
/gate/anode/geometry/setHeight 2.128 mm
/gate/anode/geometry/setPhiStart 0 deg
/gate/anode/geometry/setDeltaPhi 360 deg
/gate/anode/placement/setRotationAxis 1 0 0
/gate/anode/placement/setRotationAngle 270 deg
/gate/anode/placement/setTranslation 0.0 0.0 25 mm
#25 mm from Tube.pdf p.4
/gate/anode/vis/setColor blue
/gate/anode/vis/forceSolid
```

#Cathode

```
/gate/monobloc/daughters/name cathode
/gate/monobloc/daughters/insert box
/gate/cathode/geometry/setXLength 5 mm
/gate/cathode/geometry/setYLength 0.1 mm
/gate/cathode/geometry/setZLength 5 mm
/gate/cathode/placement/setTranslation 0.0 -29.54423 -5.209445 mm
/gate/cathode/placement/setRotationAxis 1 0 0
```

```
#beam is perpendicular to anode surface
/gate/cathode/placement/setRotationAngle 10 deg
/gate/cathode/setMaterial Vacuum

# Polycarbonate Window

/gate/monobloc/daughters/name pcwindow
/gate/monobloc/daughters/insert tessellated
#eliminate overlap
/gate/pcwindow/placement/setTranslation 0 75 99.9 mm
/gate/pcwindow/placement/setRotationAxis 0 0 1
/gate/pcwindow/placement/setRotationAngle 90 deg
/gate/pcwindow/geometry/setPathToSTLFile data/exit.stl
/gate/pcwindow/setMaterial PC
/gate/pcwindow/vis/forceSolid
/gate/pcwindow/vis/setColor blue

# Lead cone

/gate/monobloc/daughters/name xraycasing
/gate/monobloc/daughters/insert tessellated
#eliminate overlap
/gate/xraycasing/placement/setTranslation 0 75 100 mm
/gate/xraycasing/placement/setRotationAxis 0 0 1
/gate/xraycasing/placement/setRotationAngle 90 deg
/gate/xraycasing/geometry/setPathToSTLFile data/xraycasing.stl
/gate/xraycasing/setMaterial Lead
/gate/xraycasing/vis/forceSolid
/gate/xraycasing/vis/setColor yellow

# Glass

/gate/monobloc/daughters/name glassfilter
/gate/monobloc/daughters/insert cylinder
/gate/glassfilter/geometry/setRmin 37 mm
/gate/glassfilter/geometry/setRmax 40 mm
/gate/glassfilter/geometry/setHeight 150 mm
/gate/glassfilter/geometry/setPhiStart 0 deg
/gate/glassfilter/geometry/setDeltaPhi 360 deg
/gate/glassfilter/placement/setTranslation 0.0 0.0 25 mm
/gate/glassfilter/placement/setRotationAxis 1 0 0
/gate/glassfilter/placement/setRotationAngle 90 deg
/gate/glassfilter/setMaterial Glass
```

```
/gate/glassfilter/vis/forceSolid  
/gate/glassfilter/vis/setColor green
```

```
# Oil
```

```
/gate/monobloc/daughters/name oilfilter  
/gate/monobloc/daughters/insert cylinder  
/gate/oilfilter/geometry/setRmin 40 mm  
/gate/oilfilter/geometry/setRmax 45 mm  
/gate/oilfilter/geometry/setHeight 150 mm  
/gate/oilfilter/geometry/setPhiStart 0 deg  
/gate/oilfilter/geometry/setDeltaPhi 360 deg  
/gate/oilfilter/placement/setTranslation 0.0 0.0 25 mm  
/gate/oilfilter/placement/setRotationAxis 1 0 0  
/gate/oilfilter/placement/setRotationAngle 90 deg  
/gate/oilfilter/setMaterial Oil  
/gate/oilfilter/vis/forceSolid  
/gate/oilfilter/vis/setColor red
```

```
# Flattening Filter
```

```
/gate/monobloc/daughters/name FlatteningFilter  
/gate/monobloc/daughters/insert tessellated  
/gate/FlatteningFilter/placement/setTranslation 0.0 0.0 -54.0 mm  
/gate/FlatteningFilter/placement/setRotationAxis 0 0 1  
/gate/FlatteningFilter/placement/setRotationAngle -90 deg  
/gate/FlatteningFilter/geometry/setPathToSTLFile data/flatteningfilter.stl  
/gate/FlatteningFilter/setMaterial Aluminium  
/gate/FlatteningFilter/vis/forceSolid
```

```
# Primary Collimator
```

```
/gate/monobloc/daughters/name Primaerkollimator  
/gate/monobloc/daughters/insert tessellated  
#eliminate overlap  
/gate/Primaerkollimator/placement/setTranslation -0.05 -0.05 -52 mm  
/gate/Primaerkollimator/placement/setRotationAxis 0 0 1  
/gate/Primaerkollimator/placement/setRotationAngle 180 deg  
/gate/Primaerkollimator/geometry/setPathToSTLFile data/kollimator.stl  
/gate/Primaerkollimator/setMaterial Lead  
/gate/Primaerkollimator/vis/forceSolid
```

===== *HVL Detector* =====

Copper Filter

```
/gate/xrhead/daughters/name cufilter
/gate/xrhead/daughters/insert box
/gate/cufilter/geometry/setXLength 5 cm
/gate/cufilter/geometry/setYLength 5 cm
/gate/cufilter/geometry/setZLength 0.5 mm
/gate/cufilter/setMaterial Copper
/gate/cufilter/placement/setTranslation 0.0 6.54 -115 mm
```

Energy Spectrum Actor

```
/gate/xrhead/daughters/name spectrum
/gate/xrhead/daughters/insert box
/gate/spectrum/geometry/setXLength 5 cm
/gate/spectrum/geometry/setYLength 5 cm
/gate/spectrum/geometry/setZLength 0.1 mm
/gate/spectrum/setMaterial Air
/gate/spectrum/placement/setTranslation 0.0 6.54 -117 mm
```

HVL Detector

```
/gate/xrhead/daughters/name detector
/gate/xrhead/daughters/insert box
/gate/detector/geometry/setXLength {CubeSize} mm
/gate/detector/geometry/setYLength {CubeSize} mm
/gate/detector/geometry/setZLength {zlength} mm
/gate/detector/setMaterial {DetectorMaterial}
/gate/detector/placement/setTranslation 0.0 6.54 -130 mm
```

===== *Lynx Detector* =====

```
/gate/world/daughters/name lynx
/gate/world/daughters/insert box
/gate/lynx/geometry/setXLength {LynxSize} mm
/gate/lynx/geometry/setYLength {LynxSize} mm
/gate/lynx/geometry/setZLength {LynxLength} mm
```

```
/gate/lynx/setMaterial {LynxMaterial}
/gate/lynx/placement/setTranslation 0.0 17.57 -311.3 mm

#===== Backscatter Detector =====

/gate/monobloc/daughters/name bsdetector
/gate/monobloc/daughters/insert box
/gate/bsdetector/geometry/setXLength 5 cm
/gate/bsdetector/geometry/setYLength 0.1 cm
/gate/bsdetector/geometry/setZLength 5 cm
/gate/bsdetector/setMaterial Vacuum
/gate/bsdetector/placement/setTranslation 0.0 -1 0 mm
/gate/bsdetector/placement/setRotationAxis 1 0 0
/gate/bsdetector/placement/setRotationAngle 10 deg

#=====
# parameters.mac
#=====

# this section executes the settings for cut and
# step size for each volume found in control.mac

#===== world volume =====

#Cut
/gate/physics/Gamma/SetCutInRegion world {world_cut} mm
/gate/physics/Electron/SetCutInRegion world {world_cut} mm
/gate/physics/Positron/SetCutInRegion world {world_cut} mm

#Tracking cut
/gate/physics/SetMinRemainingRangeInRegion world {world_cut} mm
/gate/physics/ActivateSpecialCuts e-

#stepLimiter
/gate/physics/SetMaxStepSizeInRegion world {world_step} mm
/gate/physics/ActivateStepLimiter proton
/gate/physics/ActivateStepLimiter deuteron
/gate/physics/ActivateStepLimiter triton
/gate/physics/ActivateStepLimiter alpha
```

```
/gate/physics/ActivateStepLimiter GenericIon

#===== detector volume =====

#Cut
/gate/physics/Gamma/SetCutInRegion detector {detector_cut} mm
/gate/physics/Electron/SetCutInRegion detector {detector_cut} mm
/gate/physics/Positron/SetCutInRegion detector {detector_cut} mm

#Tracking cut
/gate/physics/SetMinRemainingRangeInRegion detector {detector_cut} mm
/gate/physics/ActivateSpecialCuts e-

#stepLimiter
/gate/physics/SetMaxStepSizeInRegion detector {detector_step} mm
/gate/physics/ActivateStepLimiter proton
/gate/physics/ActivateStepLimiter deuteron
/gate/physics/ActivateStepLimiter triton
/gate/physics/ActivateStepLimiter alpha
/gate/physics/ActivateStepLimiter GenericIon

#===== anode volume =====

#Cut
/gate/physics/Gamma/SetCutInRegion anode {anode_cut} mm
/gate/physics/Electron/SetCutInRegion anode {anode_cut} mm
/gate/physics/Positron/SetCutInRegion anode {anode_cut} mm

#Tracking cut
/gate/physics/SetMinRemainingRangeInRegion anode {anode_trackcut} mm
/gate/physics/ActivateSpecialCuts e-
/gate/physics/ActivateSpecialCuts gamma

#stepLimiter
/gate/physics/SetMaxStepSizeInRegion anode {anode_step} mm
/gate/physics/ActivateStepLimiter gamma
/gate/physics/ActivateStepLimiter proton
/gate/physics/ActivateStepLimiter electron
/gate/physics/ActivateStepLimiter deuteron
/gate/physics/ActivateStepLimiter triton
/gate/physics/ActivateStepLimiter alpha
/gate/physics/ActivateStepLimiter GenericIon
```

```
# ===== Filter Volume =====

#Cut
/gate/physics/Gamma/SetCutInRegion cufilter {filter_cut} mm
/gate/physics/Electron/SetCutInRegion cufilter {filter_cut} mm
/gate/physics/Positron/SetCutInRegion cufilter {filter_cut} mm

#Tracking cut
/gate/physics/SetMinRemainingRangeInRegion cufilter {filter_trackcut} mm
/gate/physics/ActivateSpecialCuts e-
/gate/physics/ActivateSpecialCuts gamma

#stepLimiter
/gate/physics/SetMaxStepSizeInRegion cufilter {filter_step} mm
/gate/physics/ActivateStepLimiter gamma
/gate/physics/ActivateStepLimiter proton
/gate/physics/ActivateStepLimiter electron
/gate/physics/ActivateStepLimiter deuteron
/gate/physics/ActivateStepLimiter triton
/gate/physics/ActivateStepLimiter alpha
/gate/physics/ActivateStepLimiter GenericIon

# =====

# actors.mac
# =====

# ===== Statistics actor =====

/gate/actor/addActor SimulationStatisticActor stat
/gate/actor/stat/saveEveryNSeconds 5
/gate/actor/stat/save output/STAT.txt
/gate/actor/stat/saveEveryNSeconds 10

# ===== HVL Dose actor =====

# this actor is the detector for all HVL simulations

/gate/actor/addActor TLEDoseActor dose-PDD
/gate/actor/dose-PDD/attachTo detector
/gate/actor/dose-PDD/stepHitType random
```

```
/gate/actor/dose-PDD/enableEdep true
/gate/actor/dose-PDD/enableUncertaintyEdep true
/gate/actor/dose-PDD/enableDose true
/gate/actor/dose-PDD/enableSquaredEdep true
/gate/actor/dose-PDD/enableSquaredDose true
/gate/actor/dose-PDD/save output/dose.txt
/gate/actor/dose-PDD/setVoxelSize {CubeSize} {CubeSize} {Resol} mm
```

```
/gate/actor/addActor DoseActor dose-noh
/gate/actor/dose-noh/attachTo detector
/gate/actor/dose-noh/stepHitType random
/gate/actor/dose-noh/enableNumberOfHits true
/gate/actor/dose-noh/save output/dose.txt
/gate/actor/dose-noh/setVoxelSize {CubeSize} {CubeSize} {Resol} mm
```

```
#===== Energy spectrum actor =====
```

```
# this actor registers the energy spectrum
```

```
/gate/actor/addActor EnergySpectrumActor PhaseActor
/gate/actor/PhaseActor/save output/PhaseActor.txt
/gate/actor/PhaseActor/energySpectrum/setEmin 3 keV
/gate/actor/PhaseActor/energySpectrum/setEmax 130 keV
/gate/actor/PhaseActor/energySpectrum/setNumberOfBins 1500
/gate/actor/PhaseActor/energyLossHisto/setEmin 3 keV
/gate/actor/PhaseActor/energyLossHisto/setEmax 130 keV
/gate/actor/PhaseActor/energyLossHisto/setNumberOfBins 1500
/gate/actor/PhaseActor/attachTo spectrum
```

```
#===== Lynx 2D Dose Actor =====
```

```
# this is the simulated Lynx camera
```

```
/gate/actor/addActor TLEDoseActor lynxact
/gate/actor/lynxact/attachTo lynx
/gate/actor/lynxact/stepHitType random
/gate/actor/lynxact/enableEdep true
/gate/actor/lynxact/enableUncertaintyEdep true
/gate/actor/lynxact/enableDose true
/gate/actor/lynxact/save output/lynx.txt
/gate/actor/lynxact/setVoxelSize 1 1 3 mm
```

```
#===== Focal Spot =====  
  
# this actor registers the origin of secondary particles  
# and thus the shape of the electron focal spot  
  
/gate/actor/addActor ProductionAndStoppingActor pasta  
/gate/actor/pasta/save output/pasta.txt  
/gate/actor/pasta/attachTo anode  
/gate/actor/pasta/setResolution 30000 1 1000  
/gate/actor/pasta/stepHitType post  
/gate/actor/pasta/addFilter particleFilter  
/gate/actor/pasta/particleFilter/addParticle gamma  
/gate/actor/pasta/saveEveryNSeconds 30  
  
#===== Electron Backscatter =====  
  
# this actor registers ALL particles that enter or exit  
# the anode surface.  
# Direction and type of particle must be filtered to  
# isolate backscattered electrons from the data  
  
/gate/actor/addActor PhaseSpaceActor bsactor  
/gate/actor/bsactor/save output/phasespace.root  
/gate/actor/bsactor/attachTo bsdetector  
/gate/actor/bsactor/enableParticleName true  
/gate/actor/bsactor/enableProductionVolume true  
/gate/actor/bsactor/enableProductionProcess true  
  
#=====   
# source.mac  
#=====   
  
# Electron beam  
# superposition of multiple normal distributions  
# set energy in ./data/electronenergy.txt  
# deactivate either small or large focal spot by  
# commenting the block
```

#===== *Small Focal Spot* =====

```
/gate/source/addSource beam1 gps
/gate/source/beam1/gps/particle e-
/gate/source/beam1/gps/type Beam
/gate/source/beam1/gps/shape Circle
/gate/source/beam1/attachTo cathode
/gate/source/beam1/gps/pos/centre 0 -0.2504737 0 mm
/gate/source/beam1/gps/pos/sigma_x 0.166848 mm
/gate/source/beam1/gps/pos/sigma_y 0.2247027 mm
/gate/source/beam1/gps/direction 0 1 0
/gate/source/beam1/gps/energytype UserSpectrum
/gate/source/beam1/gps/setSpectrumFile ./data/electronenergy.txt
/gate/source/beam1/setIntensity 0.3918212
```

```
/gate/source/addSource beam2 gps
/gate/source/beam2/gps/particle e-
/gate/source/beam2/gps/type Beam
/gate/source/beam2/gps/shape Circle
/gate/source/beam2/attachTo cathode
/gate/source/beam2/gps/pos/centre 0 -1.187225 0 mm
/gate/source/beam2/gps/pos/sigma_x 0.166848 mm
/gate/source/beam2/gps/pos/sigma_y 0.2678737 mm
/gate/source/beam2/gps/direction 0 1 0
/gate/source/beam2/gps/energytype UserSpectrum
/gate/source/beam2/gps/setSpectrumFile ./data/electronenergy.txt
/gate/source/beam2/setIntensity 0.1500595
```

```
/gate/source/addSource beam3 gps
/gate/source/beam3/gps/particle e-
/gate/source/beam3/gps/type Beam
/gate/source/beam3/gps/shape Circle
/gate/source/beam3/attachTo cathode
/gate/source/beam3/gps/pos/centre 0 1.131808 0 mm
/gate/source/beam3/gps/pos/sigma_x 0.166848 mm
/gate/source/beam3/gps/pos/sigma_y 0.3000225 mm
/gate/source/beam3/gps/direction 0 1 0
/gate/source/beam3/gps/energytype UserSpectrum
/gate/source/beam3/gps/setSpectrumFile ./data/electronenergy.txt
/gate/source/beam3/setIntensity 0.1717472
```

```
/gate/source/addSource beam4 gps
/gate/source/beam4/gps/particle e-
```

```
/gate/source/beam4/gps/type Beam
/gate/source/beam4/gps/shape Circle
/gate/source/beam4/attachTo cathode
/gate/source/beam4/gps/pos/centre 0 0.2504737 0 mm
/gate/source/beam4/gps/pos/sigma_x 0.166848 mm
/gate/source/beam4/gps/pos/sigma_y 0.1743633 mm
/gate/source/beam4/gps/direction 0 1 0
/gate/source/beam4/gps/energytype UserSpectrum
/gate/source/beam4/gps/setSpectrumFile ./data/electronenergy.txt
/gate/source/beam4/setIntensity 0.2863722
```

```
#===== Large Focal Spot =====
```

```
#~ /gate/source/addSource beam1 gps
#~ /gate/source/beam1/gps/particle e-
#~ /gate/source/beam1/gps/type Beam
#~ /gate/source/beam1/gps/shape Circle
#~ /gate/source/beam1/attachTo cathode
#~ /gate/source/beam1/gps/pos/centre 0 -0.778 0 mm
#~ /gate/source/beam1/gps/pos/sigma_x 0.273 mm
#~ /gate/source/beam1/gps/pos/sigma_y 0.250 mm
#~ /gate/source/beam1/gps/direction 0 0 1
#~ /gate/source/beam1/gps/ene/mono 120.0 keV
#~ /gate/source/beam1/gps/ene/type Mono
#~ /gate/source/beam1/setIntensity 0.271

#~ /gate/source/addSource beam2 gps
#~ /gate/source/beam2/gps/particle e-
#~ /gate/source/beam2/gps/type Beam
#~ /gate/source/beam2/gps/shape Circle
#~ /gate/source/beam2/attachTo cathode
#~ /gate/source/beam2/gps/pos/centre 0 0.778 0 mm
#~ /gate/source/beam2/gps/pos/sigma_x 0.273 mm
#~ /gate/source/beam2/gps/pos/sigma_y 0.281 mm
#~ /gate/source/beam2/gps/direction 0 0 1
#~ /gate/source/beam2/gps/ene/mono 120.0 keV
#~ /gate/source/beam2/gps/ene/type Mono
#~ /gate/source/beam2/setIntensity 0.329

#~ /gate/source/addSource beam3 gps
#~ /gate/source/beam3/gps/particle e-
#~ /gate/source/beam3/gps/type Beam
#~ /gate/source/beam3/gps/shape Circle
```

```
#~ /gate/source/beam3/attachTo cathode
#~ /gate/source/beam3/gps/pos/centre 0 -0.078 0 mm
#~ /gate/source/beam3/gps/pos/sigma_x 0.273 mm
#~ /gate/source/beam3/gps/pos/sigma_y 0.465 mm
#~ /gate/source/beam3/gps/direction 0 0 1
#~ /gate/source/beam3/gps/ene/mono 120.0 keV
#~ /gate/source/beam3/gps/ene/type Mono
#~ /gate/source/beam3/setIntensity 0.401
```

```
=====
# visu.mac
=====
```

```
/vis/open OGLIQ
/vis/drawVolume
/vis/viewer/flush
/tracking/storeTrajectory 1
/vis/scene/add/trajectories
/vis/scene/endOfEventAction accumulate
```